Justyna Anna Niestrawska, M.Sc. RWTH Aachen

Experimental and Computational Analyses of Pathological Soft Tissues - Towards a Better Understanding of the Pathogenesis of Abdominal Aortic Aneurysms

DISSERTATION

zur Erlangung des akademischen Grades

Doktorin der technischen Wissenschaften

eingereicht an der

Technischen Universität Graz

Betreuer

Univ.-Prof. Dipl.-Ing. Dr. techn. Gerhard A. Holzapfel

Institut für Biomechanik, Technische Universität Graz

Fakultät für Informatik und Biomedizinische Technik

Graz, März 2018

EIDESSTATTLICHE ERKLÄRUNG

Ich erkläre an Eides statt, dass ich die vorliegende Arbeit selbstständig verfasst, andere als die angegebenen Quellen/Hilfsmittel nicht benutzt, und die den benutzten Quellen wörtlich und inhaltlich entnommenen Stellen als solche kenntlich gemacht habe. Das in TUGRAZonline hochgeladene Textdokument ist mit der vorliegenden Dissertation identisch.

Datum

Unterschrift

Preface

In November 2013 I was in the final phase of my Master thesis at the Auckland Bioengineering Institute in New Zealand, when I noticed the announcement for an open PhD position at the Institute of Biomechanics in Graz. I was lucky that Prof. Holzapfel agreed to an interview via Skype despite the 12 hours of time difference, as it gave me the opportunity to move to Graz, a place I have never been before and did not know anything about. Coming back from the hot NZ summer to the dark and cold winter in Germany I only stayed two weeks at home to move to Austria and to start a new chapter in my life. As many spontaneous and unplanned decisions it turned out to be perfect – I was able to work in a multicultural and diverse group with many possibilities to learn and grow and to meet numerous people from around the world and of course Austria itself (one of them becoming my partner). There are many reasons to be thankful and I would like to express my gratitude in the following paragraphs to all the people who accompanied me on this part of my path.

First of all, I would like to thank my supervisor Prof. Gerhard A. Holzapfel for his tremendous amount of support and motivation throughout my PhD. Thank you for giving me the opportunity to work with you only after two Skype-interviews from the other side of the world. It is due to your outstanding reputation that I was welcomed on international conferences and that my work received recognition.

I owe special thanks to Prof. Tina Cohnert for her support (without her I would not have been awarded the 'Aortenpreis') and many fruitful discussions. Thank you for sharing your enthusiasm and knowledge about aneurysms with me, supporting me, and of course for providing us with the valuable AAA samples throughout my research.

This work would not have been possible without my collaborators at the Institute of Pathology, Medical University of Graz. I would like to thank especially Prof. Peter Regitnig and Dr. Christian Viertler: thank you for sharing your medical expertise as well as the enthusiasm and excitement about our findings with me throughout the last few years. I am grateful for all your time and knowledge you shared, no paper or book could have provided me with it. Additionally, many thanks to Augustin Donnerer, who provided me with all required human tissues for my research.

I would like to thank all colleagues at the Institute of Biomechanics, namely Selda Sherifova, Markus Geith, Emmanouil Agrafiotis, Daniel Haspinger, Kewei Li, Gerhard Sommer, Anna Pukaluk, Andreas Schriefl, Anju Babu, Sae-Il Murtada and Jakob Eckmann for interesting Friday meetings, coffee-breaks, discussions and for providing a great working atmosphere. Especially the first three not only provided me with an incredible amount of mutual support, fruitful discussions and enjoyable after-work activities, but also became close friends. For all the time spent on supporting me with Austrian bureaucracy and listening to my complains about it, I would like to thank Bettina Strametz – you were always

there to help me with any questions I had. Thank you for your patience! Many thanks go to all students who wrote their Bachelor or Master thesis on a topic which was related to my work, providing me with valuable contributions. Also I am very grateful for the support of the former Ph.D. and Master students of our institute, namely Michael Unterberger, Hannah Weisbecker, Thomas Eriksson and Thomas Fastl, who all supported me with my questions about FEAP, despite having left the institute a while ago.

Additionally, my gratitude goes to all my colleagues abroad who I was able to work with and learn from during my PhD, namely Igor Karšaj, Lana Virag (thank you for being the best Zagreb guide one could wish for!), Gal deBotton, Mor Frank and José Luis Calvo Gallego. I am thankful especially for the last two who became close friends in Israel and Spain and made my stays there special.

I owe many thanks to my colleagues and Master thesis supervisors from the Auckland Bioengineering Institute, Martyn Nash and Vicky Wang, who I was able to publish two papers with during my PhD and who paved the road which led me to soft tissue mechanics. Thank you Vicky for keeping in touch and for all your valuable input and advice via e-mail throughout the years.

Last but not least, my deep gratitude goes to my parents, who always gave me strength to proceed showing me unconditional love and support, to all my friends outside the institute, providing the important counter-balance to the academic bubble, and to my partner and best friend, Andreas Reinisch, who supported me throughout my PhD. He showed his incredible ability to stay calm and encourage me again and again when I was having doubts, day and night. I was lucky to build up my work on his Master Thesis and was therefore provided with the most valuable foundation from the beginning of my PhD and a genuine and fruitful interest in my work throughout the four years.

Abstract

The arterial wall such as many soft biological tissues can be seen as a fiber-reinforced composite material, consisting of collagen fibers embedded in an elastic matrix. Especially during the pathogenesis of diseases such as the development of abdominal aortic aneurysms (AAA), changes in the structural components have been shown to play a significant role. Hence, there is a pressing need to develop a more profound understanding of the re-modeling processes.

Towards a better understanding of the pathogenesis of AAA preliminary studies of our group have first targeted the collagen architecture of healthy abdominal aortas (AA). These studies suggested a higher distribution of collagen fibers in-plane (the circumferential-axial plane) than out-of-plane (the radial-axial plane) in AA. Based on these findings, a novel, non-symmetric collagen fiber dispersion model was introduced, considering both in- and out-of-plane distributions separately using a bivariate von Mises distribution and utilizing two independent dispersion parameters κ_{ip} and κ_{op}.

In a subsequent study AA walls and AAA samples were systematically compared regarding their mechanics and structure. To this end, biaxial tensile tests and second-harmonic generation (SHG) imaging were used, respectively. Significant differences in both mechanics and structure were found between AA and AAA samples. AA walls showed three distinct layers, whereas this typical layered structure was mostly lost in AAA samples. The out-of-plane dispersion in healthy AAs was significantly lower compared to their diseased counterparts, which showed a significant out-of-plane dispersion. Additionally, adipocytes were found in the outer side of AAA walls. The mechanical data were fitted utilizing the proposed non-symmetric dispersion model. The structural parameters were obtained from SHG images and subsequently the mechanical data were obtained by fitting to the data from the biaxial tension tests. Mechanical parameters of AAAs were very heterogeneous and significantly different compared to AA.

The third study utilized the novel data set of three structural and three mechanical parameters for the three AA layers and AAA walls and studied their influence on the mechanical behavior. Thee different fiber dispersions were studied using the finite element analysis program FEAP, revealing significant differences of stress distributions and magnitudes, and hence highlighting the need to include these differences to gain meaningful stress predictions.

The last study in this thesis drew on the findings of the experimental study, this time applying not only mechanical tests and SHG imaging but also histology. It was possible to define three stages of disease progression based on mechanical data and find significant differences in structural and histological data between these stages. The study resulted in a novel AAA pathogenesis hypothesis derived directly from the systematic comparison of the gained data.

Zusammenfassung

Die Arterienwand kann, so wie viele biologische Weichgewebe, als ein faserverstärktes Kompositmaterial gesehen werden. Besonders während der Pathogenese von Krankheiten, wie zum Beispiel der Entwicklung eines Aortenaneurysmas (AAA), spielen Änderungen in den Strukturkomponenten eine zentrale Rolle. Aus diesen Gründen besteht die dringende Notwendigkeit ein tieferes Verständnis der Remodellierungsprozesse von AAAs zu entwickeln.

Um ein besseres Verständnis der Pathogenese von AAAs zu entwickeln, haben vorausgehende Untersuchungen die Kollagenstruktur von gesunden abdominalen Aorten (AA) analysiert. Diese Studien erkannten eine höhere Verteilung der Kollagenfasern in der Ebene (zirkumferentiell – axial) als aus der Ebene heraus (radial – axial). Basierend auf diesen Ergebnissen wurde ein neues Modell entwickelt, welches die nicht-symmetrische Kollagenfaserverteilung darstellt und auf einer bivariaten *von Mises* Verteilung basiert.

In einer darauffolgenden Studie wurden AA und AAA systematisch auf Unterschiede in ihrer Mechanik (durch biaxiale Zugversuche) und Struktur (durch second-harmonic generation (SHG) Mikroskopie) verglichen. Signifikante Unterschiede wurden gefunden. AA zeigten drei unterscheidbare Schichten, während in AAA keine solche Differenzierung sichtbar war. Auch die Verteilung der Kollagenfasern aus der Ebene heraus war in AAA deutlich höher als in AA. Zusätzlich wurden Adipozyten im äußeren Teil von AAA gefunden. Die mechanischen Daten wurden zu dem nicht-symmetrischen Modell gefittet, nachdem die strukturellen Daten aus den SHG Bildern ermittelt wurden. Die mechanischen Daten von AAA waren sehr heterogen und unterschieden sich stark von AA.

In der dritten Studie wurde der neue Satz von Materialparametern aus drei strukturellen und drei mechanischen Parametern genutzt, um deren Einfluss auf das mechanische Verhalten zu untersuchen. Drei verschiedene Faserverteilungen wurden im Finite Elemente Programm FEAP untersucht und zeigten signifikante Unterschiede sowohl in der Spannungsverteilung als auch in der -höhe, was die Relevanz dieser Unterschiede hervorhob.

Die letzte Studie baute auf den Ergebnissen der experimentellen Studie auf und erweiterte diese um histologische Daten. Es war möglich, drei Kankheitsstadien anhand der mechanischen Daten zu differenzieren und signifikante Unterschiede sowohl in Struktur als auch in Mechanik zwischen diesen zu finden. Die Studie war in der Lage eine neue Hypothese der Pathogenese von AAA vorzustellen, die direkt aus dem systematischen Vergleich der Daten resultierte.

CONTENTS

1 INTRODUCTION

1.1 Motivation

Every year cardiovascular diseases (CVD) cause almost 4 million deaths in Europe. This makes CVD the leading cause of death in Europe, accounting for 45 % of all deaths. The overall cost for the EU economy is estimated to 230 billion € a year [1]. Statistics for the United States and China show similar trends, with 30.8 % and 32 % of all deaths being caused by CVD, respectively [2, 3].

One of these CVD are abdominal aortic aneurysms (AAA), which represent a significant disease in the western population, especially for men over 65 years [4, 5]. AAA are localized bulges of the abdominal aorta which exceed the normal diameter by more than 50 % and are often clinically silent. If not treated, many AAA tend to grow and eventually rupture, which is associated with a mortality rate up to 85 % [6]. However, treatment of AAAs with elective surgical repair or with endovascular grafts bears a high risk especially for elderly patients and does not necessarily improve survival [7, 8]. As current criteria for surgery such as the 'maximum diameter criterion' are more a rule of thumb than a scientific criterion, there is a pressing need for a reliable basis of decision-making. The acquisition of patient-specific *in vivo* data has improved over the past decades, and hence patient-specific finite-element (FE) analysis has become a promising tool to predict stress states and serve as a more reliable aid for decision making [9]. However, many studies utilize strongly simplified models (see Chapter 4.1). These simplifications, along with other influences such as AAA shape or diameter, have been shown to have a significant impact on wall stress magnitudes and locations, and hence the outcome of FE studies should be treated with caution [10–14].

Understanding the characteristics of both healthy and diseased arteries is the key for adequate computational modeling. Only with a detailed knowledge of the structure and mechanics, starting with healthy and extending to diseased tissues, pathogenesis and disease progression can be understood. Hence, this thesis focuses on both experimental methods – collecting data on healthy aortas and on changes in both mechanics and structure during disease progression – and the simultaneous inclusion of these data into computational models. This synergy allows for promising and exciting insights into the disease progression of AAA.

1.2 The Healthy Abdominal Aorta

Arteries can be classified into three types: elastic arteries, muscular arteries and arterioles. Elastic arteries convey oxygenated blood from the heart to the systemic circulation and include all larger vessels close to the heart. This group consists of the pulmonary artery, the ascending, thoracic and abdominal aortas, and the branches which originate from the aortic arch. Muscular arteries cannot be sharply distinguished from elastic arteries as there is no distinct boundary between these types. However, they are located mostly towards the periphery of the cardiovascular system and include vessels such as carotid or the coronary arteries. The group of the arterioles are the smallest type of arteries and part of the microcirculation. [15]

The abdominal aorta (AA) is an elastic artery and provides all the oxygenated blood to the organs and tissues in the abdomen as well as the pelvis and the lower limbs. It serves as a conduction tube and assists a continuous blood flow along the tube [15].

1.2.1 Structure

The healthy AA consists of three layers, namely the *tunica intima*, *tunica media* and *tunica adventitia* as shown in Figure 1.1, which are subsequently described.

Intima

The innermost layer is the *tunica intima*. It forms the barrier towards the blood flow with an endothelial lining with flat and elongated cells, oriented towards the blood flow. The subendothelial layer connects the endothelial lining with the artery, consisting of both elastin and collagen. Smooth muscle cells (SMC) may be present in this layer, which secrete collagen, elastin and extracellular ground substance [15]. The border towards the media is formed by the internal elastic membrane, which is the innermost of up to 90 elastic layers of the aortic wall. In young arteries the intima is very thin, its main purpose being to provide a non-clotting interface towards the blood flow and serving as a gateway for nutrient transport to and from the blood stream [17]. In this stage it does not play any biomechanical role. However, it thickens and becomes mechanically significant with age [18].

Media

The middle and thickest layer is the *tunica media*. It consists of 40 to 70 lamellae or fenestrated sheets of elastin which facilitate the diffusion of substances in the aortic wall and provide the elasticity [15]. SMC are present in the media and arranged in layers. They

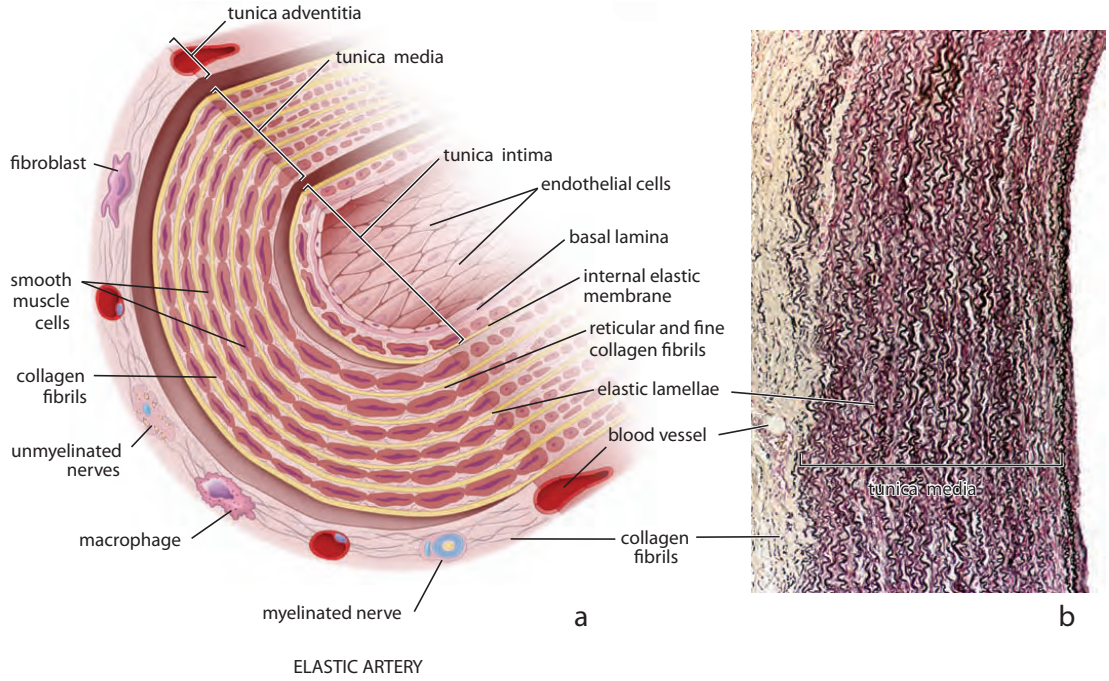

Figure 1.1: Idealization (a) and micrograph (b) of a healthy elastic artery, consisting of the three layers intima, media and adventitia. Note the blood vessels, macrophages and nerves in the adventitia and the organization of elastic lamellae and SMC in the media. With permission from [16].

synthesize collagen, elastin and extracellular ground substance and may proliferate and migrate to the intima in response to certain growth factors. Under physiological conditions the media is mechanically the most important layer with circumferentially oriented collagen fibers which provide stability under physiological blood pressures [19].

Adventitia

The outermost layer consists of a loose network of elastin and collagen, and is less organized than the media. The network is interspersed with fibroblasts and macrophages. The collagen fibers are mostly oriented towards the axial direction, preventing the overextension of the artery under super-physiological blood pressures [19]. Vasa vasorum (blood vessels) and nerves infiltrate the adventitia from outside, providing nutrients and removing waste products from the outer aortic wall [15]. The adventitia anchors in the surrounding tissue and is contiguous to perivascular adipose tissue [20, 21].

Collagen

Collagen is the most important structural biological polymer in vertebrates, making up to 30 % of their mass [22]. To date 28 types of collagen have been detected in the human body, which are categorized according to their structural properties [23]. Collagen molecules mainly consist of three helically wound peptide chains. The most common types of collagen in the aortic walls are type I and III [24]. Both type I and III belong to the fibrillar collagens. In the intima and media, most collagen is synthesized by SMC, whereas most collagen in the adventitia is synthesized by fibroblasts [25].

Collagen fibers exhibit a highly hierarchical structure as they are built of parallel fibrils which themselves consist of parallel collagen molecules. This leads to several advantages, such as the Cook-Gordon effect which describes the arresting of an initial crack at the surface of a fibril, making crack propagation more unlikely [26]. These characteristics lead to an ultimate tensile strength of $50 - 100\,\mathrm{MPa}$ which makes collagen fibers suited to withstand high tensile stresses without rupture [27].

The hierarchical structure of collagen leads to special optical properties of collagen fibers, namely birefringence, autofluorescence and second-harmonic generation (SHG). Birefringence is responsible for double refraction where a ray of light is split by polarization into two rays which take different paths. This phenomenon makes imaging of collagen via polarized light microscopy possible [28]. The positive birefringence of collagen can be intensified with certain stains, the most commonly used being Picrosirius red stain [29, 30]. Autofluorescence [31] and SHG [32] are both types on non-linear light-matter interactions and utilized in multiphoton microscopy (MPM) [33]. They both yield high contrast and optical sectioning capabilities without destroying the examined tissue or the addition of contrast agents.

Elastin

Elastin provides the elasticity and resilience to many tissues in the human body, including large arteries and constitutes around 30 % of the dry weight of arteries. It is a very durable and insoluble biopolymer. Elastin is a crosslinked array of tropoelastin and forms concentric rings around the lumen in large arteries without a specific orientation [34]. Elastin fibers consist of elastin molecules organized in densely cross-linked filaments. Elastin is produced by SMC only until maturity and exhibits a half-life of 40-70 years [35]. As collagen fiber bundles are embedded in a dense network of elastin in a wavy configuration, the mechanical response of the aortic wall is governed by the isotropic elastin under small loads, which can be stretched up to 70 % of its length [36] and provides recoil, and hence integrity of the arterial wall under the oscillating blood pressure.

Other Relevant Constituents

Proteoglycans have been shown to have a significant impact on the stress distribution in aortic walls, being able to regulate residual stresses in aortas [37]. Additionally to all passive components mentioned previously, SMCs have an impact on the stresses inside aortic tissues as they are able to actively contract, and hence influence the diameter and flow resistance in the vessels [15]. Besides exhibiting a contractile phenotype, SMCs can transit to a synthetic phenotype, where the cell morphology changes. In this phenotype SMCs can produce substances such as growth factors, proteases and components of the ECM [38].

1.2.2 Biomechanical Behavior

From the biomechanical point of view the arterial wall is a composite material with collagen fibers embedded in an isotropic ground matrix. It exhibits a characteristic exponential stiffening behavior under loading which is highly anisotropic [39]. The nonlinear stiffening is due to the gradual reorientation and recruitment of wavy collagen fibers which are the main load bearing element in arterial walls [40]. At low pressures the stress-strain behavior is linear and mostly governed by the elastic tissue components. With increasing loads the stresses are progressively carried by collagen fibers which continuously align in the direction of load and hence lead to the characteristic progressive stiffening and the high anisotropy [39].

Stresses are still present in unloaded vessels due to the existence of *residual stresses*. This was first observed in 1960 by Bergel et al. [41] who described the opening of an arterial ring after a radial cut and was further investigated by Fung and Vaishnav independently [42, 43]. Residual stresses imply that the luminal part of vessels is under compression, whereas the external part is under tension. This leads to an equilibration of stresses throughout the wall *in vivo* due to the internal blood pressure [27, 44, 45]. It is widely accepted that residual stresses are the result of growth and remodeling [46]. The constituent mainly responsible for residual stresses is elastin which has been proven by selective digestion of components in the arterial wall [47].

Arterial walls can be assumed to be incompressible due to their high water content ($70-80\,\%$). Although there may be small movements of fluids within the tissue, experimental observations have proven this assumption to hold under a large variety of loads [48–50].

A certain degree of viscoelasticity is present in aortic walls, revealed by a certain stress relaxation after deformations and a small hysteresis under cyclic loads. This is most likely due to fluid transport within the extracellular matrix and the friction between the constituents. However, after preconditioning, aortic tissues display a highly repetitive behavior and hence can be considered to behave in a pseudoelastic manner [51].

1.3 Abdominal Aortic Aneurysms

The world aneurysm is derived from the greek word $\alpha\nu\varepsilon\upsilon\rho\upsilon\sigma\mu\alpha$ (aneurusma) which means 'widening'. Abdominal aortic aneurysms are, together with intracranial saccular aneurysms, the most common types of aneurysms. AAA mostly occur in the human infrarenal aorta, which is around 12 cm long and exhibits an diameter of 2 cm and a wall thickness of around 0.22 cm in the healthy case [6]. They are permanent balloon-like dilatations of the aortic wall which can be saccular, hour glass or fusiform shaped. The latter shape is the most common one, where the aneurysm bulges out evenly to all sides, whereas saccular aneurysms bulge out only to one side. The shape of a AAA has been showsn to influence the stress distribution inside the AAA wall significantly [52]. The thickness of the aortic wall varies significantly in aneurysms. Depending on the location of the measurement the wall thickness was measured to vary from 0.23 mm on rupture sides up to 4.26 mm at highly calcified locations, leading to an average thickness of 1.50 mm [53]. 75 % of all AAAs are accompanied by an intraluminal thrombus (ILT), which is a fibrin structure consisting of blood proteins and cells, platelets and cellular debris [54]. The impact of an ILT on AAA development has not been clarified yet, but it was suggested by clinical studies that it might contribute to a higher expansion rate [55].

1.3.1 Pathogenesis and Changes in Structural Proteins

As discussed in Chapter 1.2.1, elastin and collagen are important structural proteins in the AA. The content of both constituents has been shown to be significantly altered in AAA walls. Early studies revealed a thinning and disruption of the media and a significant loss of elastin [56]. In 1994 He and Roach [57] quantified the decrease in volume fraction of elastin from $22.7\,\% \pm 5.7\,\%$ to $2.4\,\% \pm 2.2\,\%$. The same trend was observed for the volume fraction of SMCs. As Baxter et al. [58] came to a similar conclusion it is widely accepted that loss in elastin and SMC content contribute to the initiation and dilatation of AAAs.

The mechanism leading to the loss in elastin and SMCs has not been clarified yet. It is most likely a complex interaction among various risk factors such as cigarette smoking, hypertension, sex, aging and hemodynamic factors [59, 60]. The pathogenic mechanisms leading to AAAs have been summarized in 2001 by the Vascular Biology Research Program of the National Heart, Lung and Blood institute into four areas: inflammation and immune response, biomechanical wall stress, proteolytic degradation of connective tissue within the aortic wall and molecular genetics [61]. Nordon et al. [62] suggested that AAAs are a systemic disease of the vasculature, and hence a degenerative disease. The main histological features that can be observed in AAAs are severe atherosclerosis, chronic inflammation, destructive remodeling of the media and neovascularization [63]. Although atherosclerosis has been pointed out as one of the key factors of AAA initiation, several authors have argued that both diseases might underly different pathological mechanisms.

One key difference is the localization of macrophages: in AAA they are located in the media, whereas in atherosclerosis they are observed in the subintima [60]. Figure 1.2 shows an overview from [64] on mechanisms which are involved in AAA formation, which is partly discussed in this sub-chapter.

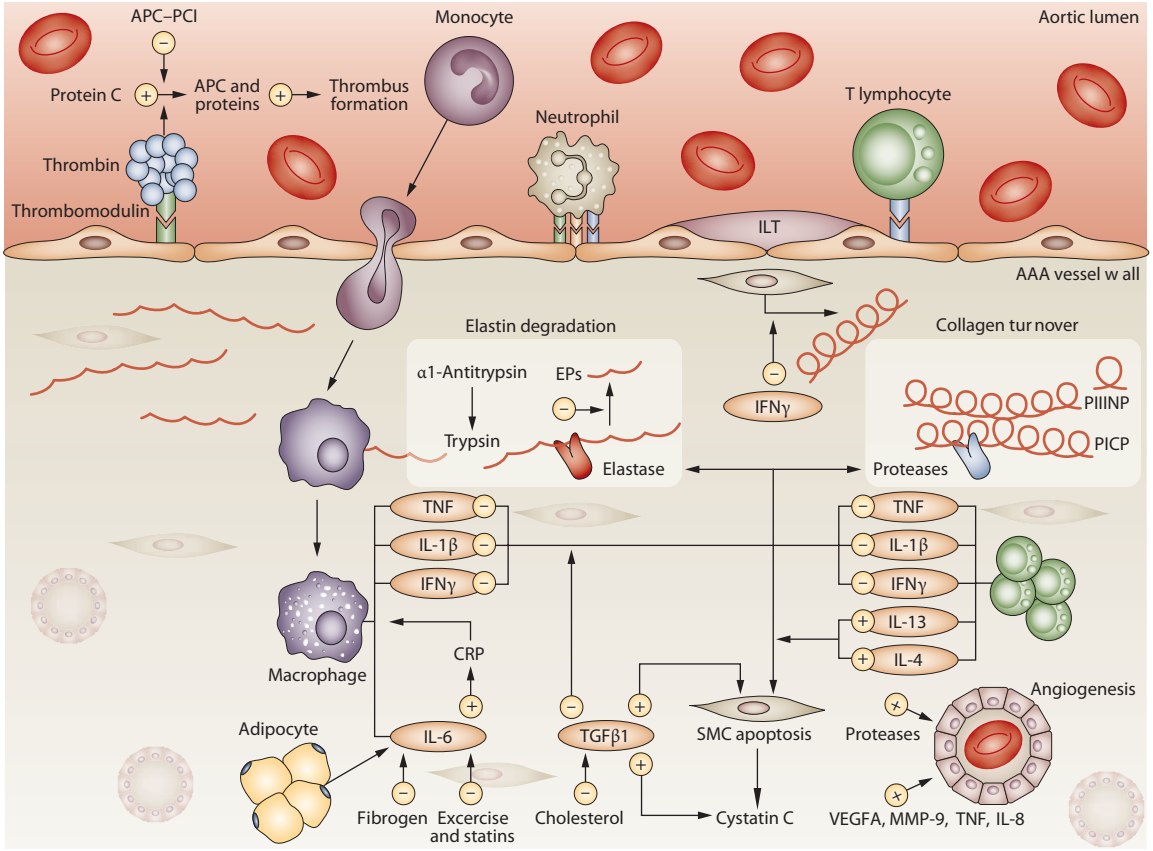

Figure 1.2: Schematic representation of mechanisms involved in AAA formation with two processes: inflammation and ECM turnover. The initiation of AAAs is connected to the recruitment of inflammatory cells to the media and macrophage infiltration. ILT is formed on the luminal side, where the adhesion of inflammatory cells can be seen. This promotes SMC apoptosis, elastin degradation and collagen turnover. +: promotes, -: inhibits, APC-PCI: activated protein C-protein C inhibitor complex, CRP: C-reactive protein, EP: elastin peptide, IFN: interferon, IL: interleukin, PICP: carboxy-terminal propeptide of type I procollagen, PIIINP: amino-terminal propeptide of type iii procollagen, TGF: transforming growth factor, TNF: tumor necrosis factor, VEGFA: vascular endothelial growth factor A. With permission from [64].

Proteolysis

Persistent stresses, e.g., hemodynamic or oxidative stresses, might induce dysfunctional remodeling through a production of atypical elastin and collagen by SMCs [65] and favor proteolytic degradation such as elastase and collagenase [60, 66]. Cohen et al. [66] showed that the treatment of aortas with elastase leads to dilatation and early stiffening, and treatment with collagenase only does not lead to dilatation but to rupture. Hence, it is widely accepted that elastin degradation leads to dilatation and collagen degradation ultimately leads to AAA rupture. Elastolysis is mostly induced by inflammation, medial stress and aging and has been reported primarily in the adventitia. Proteolysis in the aortic wall is mainly governed by infiltration of matrix metalloproteinases (MMPs), and countless studies have reported an increased MMP expression in AAA walls [67]. MMPs are enzymes which are produced by fibroblasts or by inflammatory cells such as macrophages, among others. Usually MMP expression is only needed for tissue remodeling in processes like embryonic development and wound healing. Nevertheless, abnormal MMP expression has been reported for pathological conditions such as tumor cell invation or rheumatoid arthritis [68]. The most common MMPs in aneurysmatic walls are MMP-2 and MMP-9 which are both able to degrade both elastin and collagen and are usually found in the media. MMP-2, predominantly secreted by adventitial SMCs and fibroblasts, mainly degrades collagen type IV and elastin and was shown to correlate with AAA diameter, hence it especially influences the early expansion of AAAs [69]. MMP-9, mainly originating from macrophages, monocytes infiltrating the adventitia and SMC, on the contrary is correlated to expansion and rupture of AAAs and is rarely found in smaller AAA [70].

Inflammatory Changes

Chronic inflammation is closely associated to formation and progression of AAAs, as the most striking pathological feature is the infiltration of inflammatory cells such as macrophages, lymphocytes and plasma cells. Shah et al. [71] suggested that these inflammatory cells lead to a release of reactive oxygen species which cause further degradation of the ECM by activating, e.g., MMPs. Macrophages are found from the onset of AAA development and are probably recruited by elastin degradation products. They are known to stimulate cytokine and protease production, B-cells and neovascularization and also to produce TIMP cells, confirming the important role of macrophages in the immune system [72]. However, the specific inflammatory cascades which cause aneurysmal growth are complicated and remain unknown [63].

Cytokines

TNF (tumor necrosis factor) is a monocyte derived cytotoxin which is believed to play a central role in AAA dilatation. It can cause SMC apoptosis and induces the release of proteases, contributing to the weakening of the aortic wall. Additionally, when released by macrophages it inhibits collagen synthesis [64]. TNF levels have been shown to be increased in AAA patients and correlate with aneurysm size [73].

Low levels of TGF (transforming growth factor)-$\beta 1$ have been observed in AAA patients. It controls proliferation and differentiation and induces apoptosis. This might contribute to the pathological wall remodeling [64]. However, Lindholt et al. [72] did not find any correlation between TGF-$\beta 1$ levels and AAA progression.

IFN-γ (interferon-gamma) inhibits collagen production by SMCs and has been studied as a potential biomarker for AAA progression and shown to be positively correlated to an increased AAA expansion rate [74]. The elevation of circulating IFN-γ for AAA patients has been shown by several studies and stressed the potential involvement in AAA development [74]. However, other studies have reported the opposite, i.e. low levels of IFN-γ [75]. Hence, there is a need for further studies examining the role of IFN-γ in AAAs.

Unfortunately, cytokines are not good biomarkers for AAA progression as they might also originate from other inflammatory sites, are quickly released and have a short half-life [64].

Hemodynamic Factors

The arterial wall is subjected to three kinds of forces induced by blood flow, namely pressure, shear stress and circumferential stress leading to axial and radial forces. Turbulent blood flow has been shown to favor aneurysm growth as it causes injury to the endothelium and accelerates the degeneration of the vessel wall [63].

Under physiological conditions, mechanical loads on arterial walls are considered to maintain a healthy microstructure. However, the mechanical loads are altered when a AAA is developing. A simple approximation of the stresses acting on the aortic wall is the Law of Laplace which states that the wall stress is proportional to the diameter of the vessel. Hence, sites of the AAA with so called ‘blebs’, which are focal saccular outpouchings, are considered to have a higher risk of rupture, as they represent areas of stress concentration [76]. These outpouchings are characterized by locally decreased elastin contents. Additionally, MMPs, as described above, are known to be enhanced by the stress in the aortic wall [77]. Macrophages, SMCs and fibroblasts are known to be able to react to mechanical stimuli with increased production of proteolytic proteins [76]. Hence, local changes in wall stresses seem to play an important role in the reported spatial variability of mechanical properties and wall integrity in AAA [78].

Influence of the ILT

As mentioned above, the basic pathological mechanism of AAA development seems to be the degradation of the media by proteolytic processes. Medial SMC have been reported to be able to initiate cell death or holding signs of apoptosis [79]. SMC death may have an impact on the reparative maintenance capacity of the ECM. The ILT contains neutrophils which can regulate MMP-9 activity, thus having a direct influence on their proteolytic effect [80]. Walls covered with a thrombus have been reported to be thinner and to contain significantly less elastin, broken elastin bands and disorganized elastic lamellae. Additionally, no change in collagen content was found, however, SMC α-actin was shown to be significantly decreased. In total it was suggested that the thrombus free wall shows lower structural integrity and higher tissue destruction than a thrombus free wall [81].

1.3.2 Risk Factors

Risk factors associated with AAA development and enlargement have been found by several large scale studies. The most striking, self-inflicted risk factor is undoubtedly tobacco smoking [82, 83]. Other risk factors are male gender, aging, hypertension, inflammation and atherosclerosis [84]. Men are six times more likely to develop an aneurysm compared to women [85], however an aneurysm is more likely to grow in females [86]. The overall differences in disease progression between the sexes remain unclear. Age is, as for all cardiovascular diseases, a striking risk factor [82]. Hypertension is another factor, which leads to stiffening of the aortic wall, leading ultimately to a change in local hemodynamics, which is regarded as one of the causes for AAA initiation [87]. Lipid levels are discussed as risk factors, as studies yielded controversial results [88–90]. However, statin intake has been discussed as a possible therapy for established AAA as it has been observed to inhibit AAA growth [91], nevertheless, this finding remains to be shown by further studies. Finally, genetic factors seem to play a key role in aneurysm development, with at least 15 % of patients having a first-degree family member with a AAA [92].

Interestingly, *diabetes mellitus* was found to have a protective effect against AAA expansion [93, 94]. Collagen glycation and the resistance to MMP digestion which are associated with *diabetes mellitus* are most likely the protecting factors here [60, 95].

1.3.3 Biomechanical Behavior

As the previous sub-chapters pointed out, the precise pathogenesis of AAA initiation and development is still poorly understood. However, as AAA involve a growth up to 800 % of the initial aortic wall, it is reasonable to seek deeper understanding of AAA wall mechanics to gain insight into the causes and progression of this disease [96].

The experimental determination of mechanical properties of soft biological tissues is aimed at capturing the relationship between acting forces and resulting deformations. The usual approach in materials science is to subject specimen to controlled loads while capturing the resulting deformation (load-controlled) or *vice versa* (motion-controlled). However, biological tissues are not engineering materials existing for themselves. They are rather part of a complex and poorly understood living entity. Isolation from the natural surroundings may affect the results of experiments severely, thus, the possible effects should always be considered when experimentally analyzing biological tissues. There are two possible approaches for experiments: *in vivo* and *ex vivo*. Both approaches offer advantages and disadvantages and there is no *per se* better approach. Experiments performed *in vivo* offer the advantage that physiological boundary effects and physiological loads act on the tissue. However, measuring the exact force remains difficult. Experiments *ex vivo* have the advantage of precisely measurable forces and motions, but, as discussed before, the influence of the extraction from its natural environment has to be considered and is not always known. A third possibility is the utilization of animal models, where many uncertain factors usually present in *in vivo* studies can be circumvented. Nevertheless, the reliability of animal models is questionable, especially when targeting diseases such as AAA development [96].

The measurement of *in vivo* distensibility under pulsatile blood pressure provides a first idea about the mechanical behavior of the aortic wall. Lanne et al. [97] defined distensibility with a pressure-strain elastic modulus dependent on the diameter, the inner pressure and a stiffness parameter. They reported a higher elastic modulus of AAA walls compared to healthy control samples, similar to MacSweeney et al. [98], who performed alike experiments in the same year. Recently, Wittek et al. [99] have introduced a novel imaging technique using time resolved 3D ultrasound combined with speckle tracking to gain full-field displacement and strain measures of AAA wall motions. They were able to differentiate between wall motion of aged, atherosclerotic and AAA patients. 3D displacement fields such as the one obtained in [99] can be used for inverse FEM analyses to obtain the *in vivo* mechanical state utilizing more advanced material models [100]. However, as it is still difficult to obtain exact fiber orientations *in vivo*, and as it has been proven that AAA wall architecture varies significantly depending on the location [53], these inverse FEM analyses still rely on significant and uncertain assumptions. Other recent studies utilized, e.g., Doppler ultrasound [101] or time-resolved ECG-gated CT imaging [102].

Experiments performed *ex vivo* allow for the quantification of intrinsic material properties due to controlled forces and displacements. Most studies here focused on uniaxial extension, as they are the easiest to perform and only require a rather small sample size. Additionally, mounting the specimen is usually easy, and hence tests can be performed until failure. The first to perform *ex vivo* tests on human AAA walls were Sumner et al. [103] and Drangova et al. [104], reporting greater stiffness of AAA specimen when compared to AA. In 1994 He and Roach [57] performed uniaxial extension tests in axial direction up to a pre-defined load. They assumed incompressibility and calculated the stress-strain

behavior, showing a non linear stress-strain curve and fitted it to an exponential function, i.e.

$$\sigma = ae^{b\epsilon}, \tag{1.1}$$

with σ being the stress, ϵ the strain and a and b are material parameters. Uniaxial extension tests in only one direction were also performed by Vorp et al. [105] and Raghavan et al. [106], testing their specimens until failure and utilizing a modified Michaelis-Menton model with three material parameters K,A and B, i.e.

$$\epsilon = [K + A/(B+\sigma)]\sigma, \tag{1.2}$$

assuming an isotropic response of the AAA wall. All three material parameters were stated to have a physical meaning, namely the contribution to stiffness of elastin, collagen and the strain needed until complete collagen recruitment. Raghavan et al. [10] introduced a hyperelastic continuum-based constitutive model in 2000, which has been widely used in later computational stress analysis studies despite limitations such as an inaccurate prediction of multiaxial relations. The model assumed again isotropy, and consists of two mechanical parameters α and β as follows

$$W = \alpha(I_{\mathrm{B}} - 3) + \beta(I_{\mathrm{B}} - 3)^2, \tag{1.3}$$

where $I_{\mathrm{B}} = \mathrm{tr}\mathbf{b} = \mathrm{tr}(\mathbf{F}\mathbf{F}^{\mathrm{T}})$ is the first invariant of the left Cauchy Green tensor $\mathbf{b}$, with $\mathbf{F}$ being the deformation gradient. Uniaxial tensile tests in both circumferential and axial direction until failure were performed by Thubikar et al. [107], Pierce et al. [108] and Sassani et al. [109], all reporting a stiffer behavior in the circumferential direction.

Despite having several advantages as mentioned above, uniaxial tensile tests are insufficient to describe multi-axial *in vivo* conditions as AAA tissues experience inside the body. The first to perform the more suitable biaxial tensile tests were Vande Geest et al. in 2006 [110]. They reported an increase in anisotropy compared to healthy AA tissue with a stiffening in the circumferential direction. In a subsequent study they introduced an anisotropic strain-energy function W, which has been extensively used in various studies. Thus,

$$W = b_0\exp[(1/2)\mathrm{b}_1\mathrm{E}_{\theta\theta}^2] + \exp[(1/2)\mathrm{b}_2\mathrm{E}_{\mathrm{zz}}^2] + \exp(\mathrm{b}_3\mathrm{E}_{\theta\theta}\mathrm{E}_{\mathrm{zz}}) - 3, \tag{1.4}$$

where E_{ij} and b_i are components of the Green-Lagrange strain tensor and material parameters, respectively [111]. Subsequent biaxial extension tests were performed by Tong et al. [112] and O'Leary et al. [113]. Further studies without own experimental data developed independent constitutive models to capture the anisotropic behavior of AAA tissue such as Rodríguez et al. [14], who defined two collagen fiber families contributing to the anisotropic behavior. The model contained five parameters and was based on [39]. Growth and remodeling of AAAs have been a target for constitutive modeling as well. An evolving model was proposed by Watton et al. in 2004 [114], including microstructural changes such as remodeling of collagen due to loss in elastin. In 2008 Volokh and Vorp [115] proposed a coupled mathematical model to simulate growth and rupture, pointing out that a

quantitative calibration of their model still needs further clinical data. Gasser et al. [116] examined the spatial orientation of collagen fibers and related them to their mechanics in 2012, using a Fung-type phenomenological model, assuming a change in collagen fiber mechanics dependent on their orientation, and a statistically motivated constitutive model, where the undulation limit changed with fiber orientation in their piecewise analytic expression for the first Piola-Kirchhoff stress. The study used theoretical assumptions on, e.g., collagen fiber crimp, without experimental validation, which remains pending.

1.3.4 Rupture Risk Assessment

Most aneurysms are not detected at early stages and remain clinically silent. Usually they are found during incidental exams or screening programs, which have been established in some countries for men above the age of 65 [117]. If not treated, many AAA tend to expand until failure. The incident of rupture is associated with a mortality rate of 75 to 90 % [5]. It occurs when, from the mechanical point of view, the local strength of the material (i.e. the degenerated aortic wall) is not sufficient to bear the pressure-induced peak wall stress (PWS) [78]. There is currently no medication available to stop AAA expansion and to prevent rupture. Thus, AAA repair is performed if the rupture risk exceeds the risk of the intervention, either by surgical or minimal invasive repair. Surgical repair has a 30-day mortality rate of 4 %, whereas for minimal invasive repair the rate is around 2 % [118].

It is currently not possible to quantify the patient-specific rupture risk reliably. Therefore, the standard criterion is still the diameter criterion, which was established based on the Law of Laplace. It assumes that rupture risk increases with an increased diameter. Lacking other criteria, it still remains the most frequently used one, although several studies have proven that a single diameter is not able to predict rupture risk accurately [119, 120]. Based on a large cohort of interventions a diameter of 55 mm was chosen as the maximum diameter for men, and 50 mm for women [121]. However, it has been proven that small AAAs can rupture and that many large aneurysms do not tend to rupture at all [122].

Expansion rate has been proposed as another mean to assess AAA rupture risk, assuming that a fast expansion rate is linked to a negative remodeling in the AAA wall [123]. An expansion rate of 6 mm per year is considered to bear a high risk for rupture [124]. However, a recent study found that monitoring maximum diameter expansion is not a good predictor for the AAA expansion rate [125]. Steinbaeck and colleagues [126] suggested in 2000 that ILT growth was correlated with expansion rate and in 2010 Parr and colleagues [127] found a median or large ILT volume to be associated with a rapid volumetric growth of the aneurysm.

Geometry of a AAA has been considered as a potential indicator for rupture risk. Fillinger et al. [128] were able to find links between tortuosity, asymmetry and rupture risk. On a basis of 259 patients they found a higher rupture risk for AAA with less tortuosity and

higher asymmetry. Asymmetry was proposed as a rupture risk by Doyle et al. [129], finding that posterior wall stresses were proportional to AAA asymmetry.

The thickness of the AAA, which has been reported to vary locally [53], was considered as a potential rupture risk criterion as well. However, wall thickness varied at rupture sites as well, as a thick wall might suggest severe inflammatory processes and pose the same rupture risk as thin walls [130]. Martufi and Gasser [125] provided a comprehensive review on rupture risk assessment and summarized influences on AAA wall strength such as female gender, presence of ILT, ruptured AAAs in family history, thick walls, hypoxia and diabetes. All of the mentioned factors were reported as wall weakening factors and were proposed to be included in future rupture risk predictions.

The prediction of the resulting wall strength underlies various modeling assumptions. Biomechanical simulations of AAAs are critically dependent on accurate three-dimensional reconstructions of patient-specific AAA geometries, realistic loading and boundary conditions and appropriate constitutive models for AAA tissues, which consider the underlying (remodeled) microstructure [125]. The most important factor for precise predictions has been discussed to be the correct geometrical representation of the AAA [10, 131]. Although these studies claimed that the material model does not have a significant impact we were able to show that varying microstructure does influence wall stress magnitudes and locations considerably, and should be considered [132]. Additionally, inclusion of the ILT and accounting for the non-homogeneous distribution of wall strength and thickness has been shown to have a considerable impact on the outcome of simulations [133]. For a summary of recent computational studies on AAA wall stress distributions see Chapter 4.1.

1.4 Organization of the Thesis

The dissertation is a compilation of four scientific papers which cover the experimental analysis of healthy abdominal aortas and AAAs, and their subsequent computational modeling.

1. **G.A. Holzapfel, J.A. Niestrawska, R.W. Ogden, A.J. Reinisch, A.J. Schriefl**

   Modelling non-symmetric collagen fiber dispersion in arterial walls, Journal of the Royal Society Interface, 12:20150188, 2015.

   The first paper introduces a novel non-symmetric collagen dispersion model, as previous studies by our group found significantly less dispersion out-of-plane (radial-axial plane) than in-plane (circumferential-axial plane) in healthy AA. A new structure tensor was constructed with a bivariate von Mises distribution. The structure tensor was then included into a strain-energy function which accommodated both

structural and mechanical features of the material, extending the rotationally symmetric dispersion model proposed by Gasser et al. [134]. The main contribution of the author was the implementation of the model into the finite element analysis program FEAP, [135] and the simulation of the representative examples, see Chapter 2.4.

2. **J.A. Niestrawska, C. Viertler, P. Regitnig, T.U. Cohnert, G. Sommer, G.A. Holzapfel**

   Microstructure and mechanics of healthy and aneurysmatic abdominal aortas: experimental analysis and modeling, Journal of the Royal Society Interface, 13:20160620, 2016.

   In this study the material properties of layer-specific healthy AA and AAA wall samples were systematically compared by means of biaxial tensile testing linked to the 3D microstructure. The microstructure was investigated by a combination of optical clearing, second-harmonic generation imaging and subsequent quantification of 3D fiber dispersion and alignment. Remarkable differences were found between healthy and diseased arteries, yielding a novel set of three structural and three material parameters. Especially the out-of-plane dispersion of collagen fibers was found to be significantly increased in AAAs compared to AA walls. The results of this study highlight the need to incorporate the structural differences into finite element simulations to reliably predict the actual *in vivo* state.

3. **J.A. Niestrawska, D.Ch. Haspinger, G.A. Holzapfel**

   The influence of fiber dispersion on the mechanical response of aortic tissues in health and disease: A computational study, Computer Methods in Biomechanics and Biomedical Engineering, *in press*.

   The third paper studies the influence of changes in structural components on the mechanical behavior, utilizing the data which was provided by the second paper: a novel set of three structural and three material parameters for the three layers of the AA as well as for the AAA wall. In particular, the influence of three different fiber dispersions was studied. The results showed significant differences in magnitudes and distribution of stresses and highlighted the need to incorporate these structural differences into finite element studies to obtain more accurate stress predictions.

4. **J.A. Niestrawska, P. Regitnig, C. Viertler, T.U. Cohnert, G.A. Holzapfel**

   The role of tissue re-modeling in mechanics and pathogenesis of abdominal aortic aneu-rysms, submitted.

   The final study is a direct continuation of the second paper, studying the changes in the microstructure, the histology and mechanics in AAAs and linking them to disease progression. We were able to define three disease stages based on collagen

recruitment points with significant differences in parameters such as collagen orientation, elastin and SMC content, and neo-adventitia formation. The study yielded a novel hypothesis for AAA pathogenesis, which was derived from a systematic comparison of histological, structural and mechanical changes in AAA walls.

This PhD thesis is extended by the following additional journal papers:

- R. Gehwolf, A. Wagner, C. Lehner, A. Bradshaw, C. Scharler, J.A. Niestrawska, G.A. Holzapfel, H.-C. Bauer, H. Tempfer and A. Traweger, *Pleiotropic roles of the matricellular protein Sparc in tendon maturation and ageing*, Scientific Reports, 6:32635, 2016.

  This study examined the influence of the protein Sparc on tendons in various aspects utilizing mouse Achilles tendons. One of these aspects was the variation in the microstructure, which was examined via SHG image analysis by the author of this thesis.

- D. Ch. Haspinger, S.-I. Murtada, J.A. Niestrawska, G. A. Holzapfel, *A numerical analysis of the interrelation between extracellular smooth muscle orientation and the intracellular filament overlap in the human abdominal aorta*, in preparation.

  In this study the influence of growth and remodeling mechanisms of SMCs on the mechanical behavior of aortas was analyzed by modifying a recently proposed chemo - mechanically coupled model with two families of muscle fibers and a non-symmetric filament overlap behavior. It is based on the Master thesis of D. Ch. Haspinger, which was supervised by the other three authors.

- G. Sommer, Ch. Benedikt, J.A. Niestrawska, G. Hohenberger, C. Viertler, P. Regitnig, T.U. Cohnert, G.A. Holzapfel, *Mechanical response of human subclavian and iliac arteries to extension, inflation and torsion*, submitted.

  This study examined the mechanical and structural differences between human subclavian and iliac arteries, utilizing extension-inflation experiments and examining residual stresses and SHG imaging. The author of this thesis contributed with the analysis of the SHG images to the work.

- M. Frank, J.A. Niestrawska, G.A. Holzapfel, G. Debotton, *Micromechanics-based modeling of the mechanical response of the media*, in preparation.

  In this paper, a periodic unit cell with periodic boundary conditions was applied to simulate the mechanical behavior of the media, only based on histological data. The data, structural data extracted from SHG images of healthy AA specimen and mechanical data from biaxial tensile tests, were analyzed and provided by the author of this thesis.

Finally, the following conference proceedings are also part of this thesis:

- J.A. Niestrawska, A.J. Reinisch, A.J. Schriefl, R.W. Ogden, G.A. Holzapfel, *Computational modeling of non-symmetric collage fiber dispersion*, 9th European Solid Mechanics Conference, Madrid, July 6 – 10, 2015
- R. Gehwolf, A. Wahner, C. Lehner, H. Tempfer, A.D. Bradshaw, J.A. Niestrawska, G.A. Holzapfel, H.C. Bauer, A. Traweger, *Age matters: molecular mechanisms contributing to tendon senescence*, Bone Joint J October 2015, 97–B (SUPP 11) 20
- J.A. Niestrawska, T.U. Cohnert, G.A. Holzapfel, *Mechanics and microstructure of healthy human aortas and AAA tissues: experimental analysis and modeling*, ECCOMAS 2016, Crete Island, Greece, June 5 – 10, 2016
- J.A. Niestrawska, G.A. Holzapfel, *Modelling of microstructure and mechanics of healthy and aneurysmatic abdominal aortas*, CMMBE 2016, Tel Aviv, Israel, September 20 – 22, 2016
- G.A. Holzapfel, J.A. Niestrawska, O. Gültekin, R.W. Ogden *The importance of considering the microstructure of soft biological tissues: A general fiber dispersion model with related analysis*, Workshop: Maths form the body 2017, Brescia, Italy, 29. – 31. May, 2017
- J.A. Niestrawska, D.Ch. Haspinger, G.A. Holzapfel, *Modeling the non-symmetric microstructure of healthy and aneurysmatic abdominal aortas*, 23rd Congress of the ESB, Sevilla, Spain, July 2 – 5, 2017
- J.A. Niestrawska, D.Ch. Haspinger, G.A. Holzapfel, *Non-Symmetric Fiber Dispersion of the Aortic Wall: A Computational Analysis*, COMPLAS 2017, Barcelona, Spain, September 5 – 7, 2017

  J.A. Niestrawska, T.U. Cohnert, G.A. Holzapfel, *Modeling tissue re-modeling during the pathogenesis of abdominal aortic aneurysms*, VAM 2018, Boston, USA, June 21 – 23, 2018
- J.A. Niestrawska, P. Regitnig, Ch. Viertler, T.U. Cohnert, G.A. Holzapfel, *The role of tissue re-modelling in mechanics and pathogenesis of abdominal aortic aneurysms*, WCB 2018, Dublin, Ireland, July 8 – 12, 2018

2 MODELING NON-SYMMETRIC COLLAGEN FIBER DISPERSION IN ARTERIAL WALLS

New experimental results on the collagen fiber dispersion in human arterial layers have shown that the dispersion in the tangential plane is more significant than that out-of-plane. A rotationally symmetric dispersion model is not able to capture this distinction. For this reason we introduce a new non-symmetric dispersion model, based on the bivariate von Mises distribution, which is used to construct a new structure tensor. The latter is incorporated in a strain-energy function that accommodates both the mechanical and structures features of the material, extending our rotationally symmetric dispersion model (TC Gasser, RW Ogden, GA Holzapfel. Hyperelastic modeling of arterial layers with distributed collagen fiber orientations. *J. R. Soc. Interface,* 3:15–35, 2006). We provide specific ranges for the dispersion parameters and show how previous models can be deduced as special cases. We also provide explicit expressions for the stress and elasticity tensors in the Lagrangian description that are needed for a finite element implementation. Material and structural parameters were obtained by fitting predictions of the model to experimental data obtained from a human abdominal aortic adventitia. In a finite element example we analyze the influence of the fiber dispersion on the homogeneous biaxial mechanical response of aortic strips, and in a final example the non-homogeneous stress distribution is obtained for circumferential and axial strips under fixed extension. It has recently become apparent that this more general model is needed for describing the mechanical behaviour of a variety of fibrous tissues.

2.1 Introduction

Physiological and pathological changes in the cardiovascular system directly influence the mechanical behaviour of arterial walls [23]. It is therefore of crucial importance to improve understanding of the mechanical properties of the constituents of arterial walls, including the inherent features of anisotropy and nonlinearity. These properties, amongst others, pose formidable challenges in the constitutive modeling and numerical analysis of such tissues and can be clearly connected to the underlying structure of the tissues. The passive mechanical behaviour of an arterial wall is governed mainly by the matrix material (which consists of water, elastin, proteoglycans, etc.) and the collagen fiber reinforcement. The anisotropy is associated with the local mean alignment of the collagen fibers, which also stiffen their response when under tension, leading to their significant nonlinear characteristics. The fibers are not perfectly aligned but are dispersed around their mean direction, and the amount and character of the dispersion depends on the topography, the particular layer of the vessel considered and the respective (patho)physiological condition, *inter alia*.

Fiber dispersion in arterial walls has been documented and analyzed in, for example, [136–139]; for an overview of the structural quantification of collagen fibers in arterial walls, see [140]. In particular, the study in [139] identified the presence of two fiber families in the intima, media and adventitia of human aortas; they are helically and almost symmetrically arranged with respect to the cylinder axis. Often a third and sometimes a fourth family is present in the intima in the respective axial and circumferential directions. The recent work [141] has revealed that while helical fiber structures are present in human elastic arteries, in more muscular arteries (as for the murine basilar artery) and veins (such as the porcine jugular vein) a transition from the helical arrangement to two nearly orthogonal fiber families aligned in the circumferential and axial directions can be observed, and it is suggested that this is to ensure optimal efficiency of the vasculature. Observations of dispersion for other tissues, including the myocardium, corneas and articular cartilage, can be found in [142, 143], [144, 145] and [146], respectively.

Several mechanical models accounting for the dispersion of collagen fibers have been proposed. Fiber dispersion can be represented either directly by incorporation in a strain-energy function via a probability density function (PDF) or by a generalized structure tensor, for example. Following [147] these two approaches are referred to as 'angular integration' (AI) and 'generalized structure tensor' (GST). The authors of [147] compared the results of the two formulations on the basis of the energy function introduced in [39] and the generalized structure tensor in [134]. As was pointed out in, for example, [148] one approach is to consider the strain energy $w(\lambda)$ of a single collagen fiber as a function of the fiber stretch λ and to integrate this over the unit sphere S to obtain the total free-energy function Ψ_{f} of the fibers per unit reference volume, i.e.

$$\Psi_{\mathrm{f}} = n \int_S \rho(\mathbf{N}) w(\lambda) \mathrm{d}S, \tag{2.1}$$

where n is the numbers of fibers per unit reference volume, $\mathbf{N}$ is a unit vector describing the orientation of an individual fiber, and ρ is the relative angular density of fibers normalized according to

$$\frac{1}{4\pi} \int_S \rho(\mathbf{N}) \mathrm{d}S = 1. \tag{2.2}$$

The region of the unit sphere where fibers are in tension is defined by the set of $\mathbf{N}$ for which $\lambda > 1$, where $\lambda = (\mathbf{C} : \mathbf{N} \otimes \mathbf{N})^{1/2}$ is the stretch in the direction $\mathbf{N}$, $\mathbf{C}$ is the right Cauchy–Green tensor and a double contraction is defined by $\mathbf{C} : \mathbf{N} \otimes \mathbf{N} = (\mathbf{C}\mathbf{N}) \cdot \mathbf{N}$. This is the AI approach.

In the GST approach the energy function is associated with a generalized structure tensor $\mathbf{H}$ and is given by

$$\Psi_{\mathrm{f}} = \Psi_{\mathrm{f}}(\mathbf{C}, \mathbf{H}), \tag{2.3}$$

where $\mathbf{H}$ is defined by

$$\mathbf{H} = \frac{1}{4\pi} \int_{\Omega} \rho(\mathbf{M}) \mathbf{M} \otimes \mathbf{M} \mathrm{d}\Omega, \qquad \text{with} \qquad \mathrm{tr}\mathbf{H} = 1, \tag{2.4}$$

the latter following from (2.2).

By comparing these approaches we see that (2.1) requires integration over the unit sphere at each point, while for the strain-energy function (2.3) no such integration is needed once $\mathbf{H}$ has been determined by $(2.4)_1$ or prescribed. On the one hand, the AI approach allows identification and exclusion of individual fibers under compression, while on the other hand this is not quite so straightforward on the basis of $(2.4)_1$. For a detailed discussion of the latter issue, see [149, 150].

In chronological order we now provide a short overview of the main existing continuum mechanical models which take fiber dispersion into account. Probably the study [151] was the first to consider fiber dispersion in the analysis of fibrous connective tissues, with the tissue structure (fiber orientation) being accounted for in the strain energy via an orientation density function. The approach [152] incorporates a two-dimensional AI distribution in a strain-energy function based on the Beta distribution, but neglects the out-of-plane dispersion of the fibers, while a planar fiber dispersion was used in [153] with a Gaussian PDF to study the biaxial behaviour of arterial walls and aortic valves. In [154] the Gaussian distribution was used to compute so-called splay invariants to represent 2D and 3D fiber dispersions, which the authors applied to aortic valve tissues.

In [39] the use of an exponential strain-energy function was motivated following [155], and this model was extended to the case of fiber dispersion in [134] based on the structure tensor $(2.4)_1$. Therein, we used a rotationally symmetric distribution of collagen fibers. In addition, the model [134] was applied to several other tissues, including the cornea [156] and articular cartilage [157], while in [158], the constitutive model of [39] was applied with the fiber orientations uniformly distributed over the azimuthal angle. A structure tensor based on a planar counterpart of that in [134] was defined in [159, 160] and used in [161].

A PDF based on the von Mises distribution taking account of a non-rotationally symmetric fiber dispersion and based on the micro-sphere model was suggested in [162], and an ellipsoidal distribution with a power-law strain-energy function, based on the AI formulation, was employed in [163] and applied to cartilage. Based on the AI approach with the von Mises distribution the authors in [164] derived a closed-form solution for a simple exponential fiber stress-strain law and applied their model to planar biaxial extension of a bioartificial tissue. The study [165] adopted the model of [134] and included the limiting case of an in-plane arrangement of fibers following the AI approach, which was also used in [166] with a planar von Mises distribution to examine the in-plane dispersion of collagen fibers. In [116] the Bingham distribution was used and was claimed to be ‘clearly superior

Table 2.1: Overview of the main existing continuum mechanical models which take fiber dispersion into account, listed in chronological order of appearance. The column 'Formulation' describes the approach originally presented in the cited paper (GST = generalized structure tensor, AI = angular integration); PDF = probability density function; 'Parameters' refer to the parameters describing the fiber dispersion (not material or any other parameters). The abbreviations 'RS', 'NS' and 'IP' refer to rotationally symmetric, non-symmetric and in-plane, respectively. For the parameters in some of the references listed we have used notation from the present paper for consistency.

Authors/Reference	Formulation	PDF	Parameters	2D/3D	Dispersion
Sacks [152]	AI	Beta	γ, δ	2D	IP
Driessen et al. [153]	AI	Gaussian	σ	2D	IP
Freed et al. [168]	AI/GST	Gaussian	σ	2D/3D	RS
Gasser et al. [134]	GST	von Mises	κ	3D	RS
Alastrué et al. [162]	AI	von Mises	various	3D	NS
Ateshian et al. [163]	AI	ellipsoidal	ξ_i, α_i, $i = 1,2,3$	3D	NS
Raghupathy and Barocas [164]	AI	von Mises	b	2D	IP
Federico and Gasser [165]	AI	von Mises	b	3D	RS
Agianniotos et al. [166]	AI	von Mises	b	2D	IP
Gasser et al. [116]	AI	Bingham	κ_1, κ_2	3D	NS
Pandolfi and Vasta [167]	GST/AI	von Mises	$\kappa, \hat{\kappa}$	3D	RS
Holzapfel and Ogden [149]	AI	von Mises	$A, B, C, D, \bar{\kappa}$	2D/3D	RS/NS
Melnik et al. [150]	GST	von Mises	κ	3D	RS
Present work	GST	bivariate von Mises	κ_{ip}, κ_{op}	3D	RS/NS/IP

to the π-periodic von Mises distribution in modeling the collagen organization in vascular tissue', which we have not found to be the case in the present study. The model [134] was extended in [167] to incorporate a higher-order statistical measure of dispersion in order to reduce differences between the GST and AI formulations. In the recent paper [149] we have introduced a fiber dispersion model with a weighted energy function that allows the exclusion of fibers which are under compression. The model, based on the AI approach, has been developed for plane strain and for three-dimensional deformations appropriate for finite element implementation (see also the discussion in [150] on the exclusion of compressed fibers using the GST approach). A summary of the main models discussed above is listed in Table 2.1.

The model in [134] has proved to be very successful, but recently it was shown in [139] that an axisymmetric model of collagen fiber dispersion is not appropriate, and a more general dispersion model is required to accommodate the new findings. Hence, based on the structure tensor approach initiated in [134] we introduce here a bivariate von Mises distribution that enables the dispersion data to be captured. In particular, for arteries, the out-of-plane dispersion is relatively narrow while the in-plane dispersion is more significant. The present work provides a natural extension of the constitutive setting documented in [39, 134] to a more general context.

This work is structured as follows. In Section 2.2 we introduce the mathematical framework for describing fiber dispersion illustrated by the use of the bivariate von Mises distribution. This is particularly appropriate for use with the new experimental data, which indicate that the current models are not sufficiently general to capture the collagen fiber structure. Then we introduce a probability density function which accounts for these experimental observations, and it is shown how the new model reproduces several special cases from the literature. The continuum mechanical framework associated with the dispersion structure introduced in Section 2.2 is presented in Section 2.3. In Section 2.4 the theory of Section 2.3 is applied in three representative numerical simulations with the aim of showing the efficacy and capability of the proposed structural model. Finally, Section 2.5 summarizes the proposed fiber dispersion model and discusses future developments of our work.

2.2 Mathematical Representation of Fiber Dispersion

2.2.1 Structure Tensor for the Fiber Dispersion

Motivated by the experimental results documented in [19], we introduce the coordinate system shown in Figure 2.1, where the unit vector $\mathbf{N}$ is an arbitrary fiber direction in the reference (undeformed) configuration, expressed in terms of the two angles Φ and Θ by

$$\mathbf{N}(\Phi,\Theta) = \cos\Theta\cos\Phi\,\mathbf{e}_1 + \cos\Theta\sin\Phi\mathbf{e}_2 + \sin\Theta\,\mathbf{e}_3, \tag{2.5}$$

where $\Phi \in [0, 2\pi]$, $\Theta \in [-\pi/2, \pi/2]$ and $\mathbf{e}_1, \mathbf{e}_2, \mathbf{e}_3$ are unit rectangular Cartesian basis vectors. Locally, $\mathbf{e}_1$ and $\mathbf{e}_2$ define the tangential plane of a cylindrical coordinate system and $\mathbf{e}_3$ the corresponding outward radial direction. For a circular cylinder, $\mathbf{e}_1$ is taken to be the circumferential direction and $\mathbf{e}_2$ the axial direction. Although the coordinate system is similar to that introduced in [134], there is a subtle but important difference: our approach does not involve symmetry about a preferred direction since recent experimental results [19] have suggested that the fiber dispersion is not rotationally symmetric.

We describe $\rho(\mathbf{N})$, which appears in (2.1), as the probability density of the fiber orientation $\mathbf{N}$ in the reference configuration as a function of Φ and Θ. In the following we write either $\rho(\mathbf{N})$ or $\rho(\Phi,\Theta)$, and this is normalized according to (2.2), equivalently

$$\frac{1}{4\pi}\int_S \rho(\Phi,\Theta)\mathrm{d}S = 1, \tag{2.6}$$

where $\mathrm{d}S = \cos\Theta\mathrm{d}\Phi\mathrm{d}\Theta$. [Note that the usual spherical polar angles are $\pi/2-\Theta$ and Φ.]

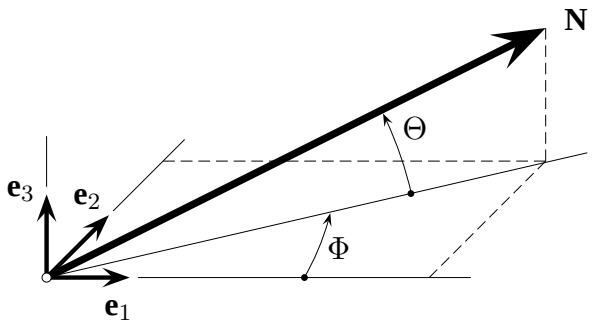

Figure 2.1: A unit vector $\mathbf{N}(\Phi,\Theta)$ representing a general fiber direction defined by the angles Φ and Θ with respect to rectangular Cartesian unit basis vectors $\mathbf{e}_1,\mathbf{e}_2,\mathbf{e}_3$.

Another requirement is that the PDF has to be independent of the sense of $\mathbf{N}$ so that $\rho(\mathbf{N}) \equiv \rho(-\mathbf{N})$, which is equivalent to $\rho(\Phi,\Theta) = \rho(\Phi+\pi,-\Theta)$. Based on the experimental results presented in [19], we introduce two additional symmetries, namely the in-plane symmetry $\rho(\Phi,\Theta) = \rho(\Phi+\pi,\Theta)$ and the out-of-plane symmetry $\rho(\Phi,\Theta) = \rho(\Phi,-\Theta)$.

It is assumed that the material behaviour does not depend on the sense of $\mathbf{N}$, so that the strain energy depends on $\mathbf{N}$ only through the tensor product $\mathbf{N}\otimes\mathbf{N}$ ([39]; see also [134] and [169]), via a symmetric second-order tensor, introduced in $(2.4)_1$, which we now write as

$$\mathbf{H} = \frac{1}{4\pi}\int_{\Phi=0}^{2\pi}\int_{\Theta=-\pi/2}^{\pi/2} \rho(\Phi,\Theta)\mathbf{N}\otimes\mathbf{N}\cos\Theta \mathrm{d}\Phi\mathrm{d}\Theta, \tag{2.7}$$

the components of which involve only $\rho(\mathbf{N})$ and the sines and cosines of the angles Φ, Θ. The tensor $\mathbf{H}$ is a structure tensor involving the fiber dispersion via $\rho(\mathbf{N})$. This is associated with a dispersion of fibers about a single mean direction, the mean direction of $\mathbf{N}$, which, according to the data in [19], has a very small component out-of-plane. We therefore assume here that the mean fiber direction, say $\mathbf{M}$, lies in the tangential plane defined by $\mathbf{e}_1$ and $\mathbf{e}_2$. An explicit expression for $\mathbf{M}$ will be written down below.

In terms of its components H_{ij} we write $\mathbf{H} = H_{ij}\mathbf{e}_i\otimes\mathbf{e}_j$ and note that, due to the symmetries of $\rho(\mathbf{N})$, the off-diagonal components H_{13} and H_{23} vanish, and the only non-zero components of $\mathbf{H}$ are therefore H_{12} and the diagonal components H_{11},H_{22},H_{33}. Thus, $\mathbf{H}$ has four non-zero components, and because $\mathrm{tr}\mathbf{H} = 1$ by $(2.4)_2$, only three of them are independent:

$$H_{11}, \quad H_{22}, \quad H_{12}, \quad \text{with} \quad H_{33} = 1 - H_{11} - H_{22}. \tag{2.8}$$

In [19] it was also observed that the dispersions in the two planes are essentially independent, which means that the PDF can be decomposed in the form

$$\rho(\Phi,\Theta) = \rho_{\mathrm{ip}}(\Phi)\rho_{\mathrm{op}}(\Theta), \tag{2.9}$$

where $\rho_{\text{ip}}(\Phi)$ and $\rho_{\text{op}}(\Theta)$ describe the in-plane and out-of-plane dispersions, respectively. Since the symmetry of the PDF has to be fulfilled, we require that

$$\rho_{\text{ip}}(\Phi) = \rho_{\text{ip}}(\Phi + \pi), \quad \rho_{\text{op}}(\Theta) = \rho_{\text{op}}(-\Theta).$$

Without taking explicit account of these symmetries the normalization in equation (2.6) is now written

$$\frac{1}{4\pi} \int_0^{2\pi} \rho_{\text{ip}}(\Phi) \mathrm{d}\Phi \int_{-\pi/2}^{\pi/2} \rho_{\text{op}}(\Theta) \cos\Theta \mathrm{d}\Theta = 1. \tag{2.10}$$

Without loss of generality we can choose the normalization of ρ_{ip} so that

$$\frac{1}{2\pi} \int_0^{2\pi} \rho_{\text{ip}}(\Phi) \mathrm{d}\Phi = 1 \tag{2.11}$$

and hence (2.10) reduces to

$$\int_{-\pi/2}^{\pi/2} \rho_{\text{op}}(\Theta) \cos\Theta \mathrm{d}\Theta = 2. \tag{2.12}$$

Let us now define

$$\kappa_{\text{op}} = \frac{1}{4} \int_{-\pi/2}^{\pi/2} \rho_{\text{op}}(\Theta) \cos^3\Theta \mathrm{d}\Theta, \tag{2.13}$$

which is a measure of the out-of-plane dispersion and is consistent with the definition, in slightly different notation, given in equation (4.1) in [134] for the case in which the dispersion is rotationally symmetric. By definition, κ_{op} is non-negative and from (2.12) and (2.13) it must satisfy $\kappa_{\text{op}} \leq 1/2$. Thus,

$$0 \leq \kappa_{\text{op}} \leq 1/2. \tag{2.14}$$

If $\rho_{\text{op}} \equiv 1$, giving an isotropic distribution, then $\kappa_{\text{op}} = 1/3$. Note that if $\rho_{\text{ip}} = 1$ then (2.11) is automatically satisfied, but on the other hand equation (2.11) does not necessarily imply that $\rho_{\text{ip}} = 1$. However, when $\rho_{\text{ip}} = 1$ we obtain $H_{11} = H_{22} = \kappa_{\text{op}}$, $H_{33} = 1 - 2\kappa_{\text{op}}$ and $H_{12} = 0$ and this corresponds to a transversely isotropic distribution with mean fiber direction $\mathbf{e}_3$. The lower limit $\kappa_{\text{op}} = 0$ corresponds to the case in which all the fibers are in the $\mathbf{e}_3$ direction (no dispersion), while the upper limit $\kappa_{\text{op}} = 1/2$ corresponds to a planar distribution in the ($\mathbf{e}_1$, $\mathbf{e}_2$) plane. For isotropy we have $\rho_{\text{ip}} = \rho_{\text{op}} = 1$ and $\kappa_{\text{op}} = 1/3$. In general ρ_{ip} and ρ_{op} are separate measures of the fiber dispersions, in-plane and out-of-plane, respectively.

We now define $\bar{\kappa}_{11}, \bar{\kappa}_{22}$ and $\bar{\kappa}_{12}$ by

$$\bar{\kappa}_{11} = \frac{1}{2\pi}\int_0^{2\pi} \rho_{\mathrm{ip}}(\Phi)\cos^2\Phi \mathrm{d}\Phi, \quad \bar{\kappa}_{22} = \frac{1}{2\pi}\int_0^{2\pi} \rho_{\mathrm{ip}}(\Phi)\sin^2\Phi \mathrm{d}\Phi, \tag{2.15}$$

$$\bar{\kappa}_{12} = \frac{1}{2\pi}\int_0^{2\pi} \rho_{\mathrm{ip}}(\Phi)\sin\Phi\cos\Phi \mathrm{d}\Phi. \tag{2.16}$$

and hence by (2.11)

$$\bar{\kappa}_{11} + \bar{\kappa}_{22} = 1. \tag{2.17}$$

Together, $\bar{\kappa}_{11}, \bar{\kappa}_{22}$ and $\bar{\kappa}_{12}$ characterize the in-plane dispersion. Note that $\bar{\kappa}_{12} = 0$ when $\rho_{\mathrm{ip}} = 1$ and also when the mean in-plane direction is either $\mathbf{e}_1$ or $\mathbf{e}_2$, as discussed below.

In general, we now have

$$H_{ab} = 2\kappa_{\mathrm{op}}\bar{\kappa}_{ab}, \quad a,b \in \{1,2\}, \quad H_{11} + H_{22} = 2\kappa_{\mathrm{op}}, \quad H_{33} = 1 - 2\kappa_{\mathrm{op}}. \tag{2.18}$$

At this point we note that the structure tensor $\mathbf{H}$ has the form

$$\mathbf{H} = \sum_{j=1}^{3} H_{jj}\mathbf{e}_j \otimes \mathbf{e}_j + H_{12}(\mathbf{e}_1 \otimes \mathbf{e}_2 + \mathbf{e}_2 \otimes \mathbf{e}_1), \tag{2.19}$$

and we emphasize, as noted above, that it is associated with a dispersion that has a single mean direction. We shall relate this to the model of dispersion discussed in [134] when considering special cases in Section 2.2.2.

An alternative way of writing the above representation is the form

$$\mathbf{H} = A\mathbf{I} + B\mathbf{M} \otimes \mathbf{M} + (1 - 3A - B)\mathbf{M}_{\mathrm{n}} \otimes \mathbf{M}_{\mathrm{n}}, \tag{2.20}$$

where the unit vector $\mathbf{M} = \cos\alpha\,\mathbf{e}_1 + \sin\alpha\,\mathbf{e}_2$ is the in-plane mean fiber direction, α being the angle between $\mathbf{M}$ and $\mathbf{e}_1$, and $\mathbf{M}_{\mathrm{n}}$ is a unit out-of-plane vector (see Figure 2.2), while A and B are constants.

By comparing (2.19) and (2.20) we find that the components H_{ij} are related to A, B and the angle α by

$$H_{11} = A + B\cos^2\alpha, \quad H_{22} = A + B\sin^2\alpha, \quad H_{12} = B\sin\alpha\cos\alpha, \tag{2.21}$$

from which we obtain

$$2A = 2\kappa_{\mathrm{op}} - B, \quad B^2 = (H_{11} - H_{22})^2 + 4H_{12}^2, \tag{2.22}$$

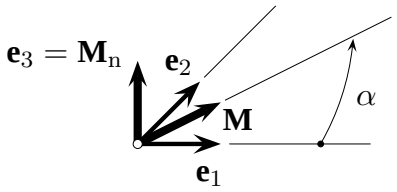

Figure 2.2: Unit vector $\mathbf{M}$ in the ($\mathbf{e}_1$, $\mathbf{e}_2$) plane, α is the angle between $\mathbf{M}$ and $\mathbf{e}_1$, while $\mathbf{M}_\mathrm{n}= \mathbf{e}_3$ is the unit out-of-plane vector given by $\mathbf{e}_1 \times \mathbf{e}_2$.

and

$$\tan 2\alpha = \frac{2\bar{\kappa}_{12}}{\bar{\kappa}_{11} - \bar{\kappa}_{22}}. \tag{2.23}$$

By defining $B = 2\kappa_{\mathrm{op}}\bar{B}$ and $A = \kappa_{\mathrm{op}}\bar{A}$ we obtain

$$\bar{A} = 1 - \bar{B}, \quad \bar{B}^2 = (\bar{\kappa}_{11} - \bar{\kappa}_{22})^2 + 4\bar{\kappa}_{12}^2, \tag{2.24}$$

where $\bar{A}$ and $\bar{B}$ depend only on the in-plane distribution. Note that $\bar{B}$ is invariant with respect to the rotation of the in-plane axes.

For any given distribution ρ_{ip} we can calculate $\bar{\kappa}_{11}, \bar{\kappa}_{22}$ and $\bar{\kappa}_{12}$ and hence the angle α and the constants $\bar{A}$ and $\bar{B}$, while κ_{op} is obtained when ρ_{op} is given. Note that $\mathbf{H}$ contains only two independent parameters. Note also that for $\alpha = 0$ or $\pi/2$ the dispersion parameter $\bar{\kappa}_{12} = 0$.

In the next subsection we consider a particular choice of the density functions ρ_{ip} and ρ_{op}.

Using the Bivariate von Mises Distribution as the Dispersion Distribution

The work [19] documented angular data sets for the in-plane collagen dispersions of the intima, media and adventitia of human non-atherosclerotic thoracic and abdominal aortas and common iliac arteries. The out-of-plane angles were measured separately for each layer, showing that the out-of-plane dispersions are very similar at all anatomic locations and for each layer. Moreover, each mean fiber angle was found to be very close to tangential. Motivated by these results we now model, as illustrative examples, each of $\rho_{\mathrm{ip}}(\Phi)$ and $\rho_{\mathrm{op}}(\Theta)$ with π-periodic von Mises distributions [170], so the overall PDF is a bivariate von Mises distribution, featuring the symmetries that were discussed in Section 2.2.1.

For $\rho_{\mathrm{ip}}(\Phi)$ we consider the basic von Mises distribution

$$\rho_{\mathrm{ip}}(\Phi) = \frac{\exp(a\cos 2\Phi)}{I_0(a)}, \tag{2.25}$$

where the so-called concentration parameter a is a constant and $I_0(a)$ is the modified Bessel function of the first kind of order 0 defined by

$$I_0(x) = \frac{1}{\pi}\int_0^\pi \exp(x\cos\alpha)\mathrm{d}\alpha, \tag{2.26}$$

which provides a normalization factor leading to (2.11) independently of a. Equation (2.25) corresponds to a distribution that is symmetric about $\Phi = 0$. Plots of the circular distribution (2.25) for different concentration parameters a are shown in Figure 2.3, and we note that as $a \to \infty$, ρ_{ip} becomes a delta function. For this special case of symmetry we use the notation κ_{11}, κ_{22} and κ_{12}. It follows from (2.25) using the definitions (2.15) and (2.16) that $\kappa_{12} = 0$ and

$$\kappa_{11} = \frac{1}{2} + \frac{I_1(a)}{2I_0(a)}, \qquad \kappa_{22} = \frac{1}{2} - \frac{I_1(a)}{2I_0(a)}, \tag{2.27}$$

where

$$I_1(x) = \frac{1}{\pi}\int_0^\pi \exp(x\cos\alpha)\cos\alpha\mathrm{d}\alpha, \tag{2.28}$$

is the modified Bessel function of the first kind of order 1.

If the distribution is symmetrical about $\Phi = \alpha$ instead of $\Phi = 0$ then Φ is replaced by $\Phi - \alpha$ in (2.25) and the appropriate values of $\bar{\kappa}_{11}$ and $\bar{\kappa}_{12}$ are given by

$$\bar{\kappa}_{11} = \kappa_{11}\cos^2\alpha + \kappa_{22}\sin^2\alpha, \qquad \bar{\kappa}_{12} = (\kappa_{11} - \kappa_{22})\sin\alpha\cos\alpha, \tag{2.29}$$

and $\bar{\kappa}_{22}$ is given by (2.17). From now on, whenever $\kappa_{12} = 0$ we use the notation κ_{ip} instead of κ_{22}.

Equation (2.12) is satisfied by taking $\rho_{\mathrm{op}}(\Theta)$ to be a von Mises distribution of the form

$$\rho_{\mathrm{op}}(\Theta) = 2\sqrt{\frac{2b}{\pi}}\frac{\exp[b(\cos 2\Theta - 1)]}{\mathrm{erf}(\sqrt{2b})}, \tag{2.30}$$

where b is a constant concentration parameter and erf is the error function defined by

$$\mathrm{erf}(x) = \frac{2}{\sqrt{\pi}}\int_0^x \exp(-\xi^2)\mathrm{d}\xi. \tag{2.31}$$

Note that (2.30) has a similar shape to (2.25) but is marginally different from the distribution used in [134], and gives a somewhat better fit to the narrow out-of-plane dispersion.

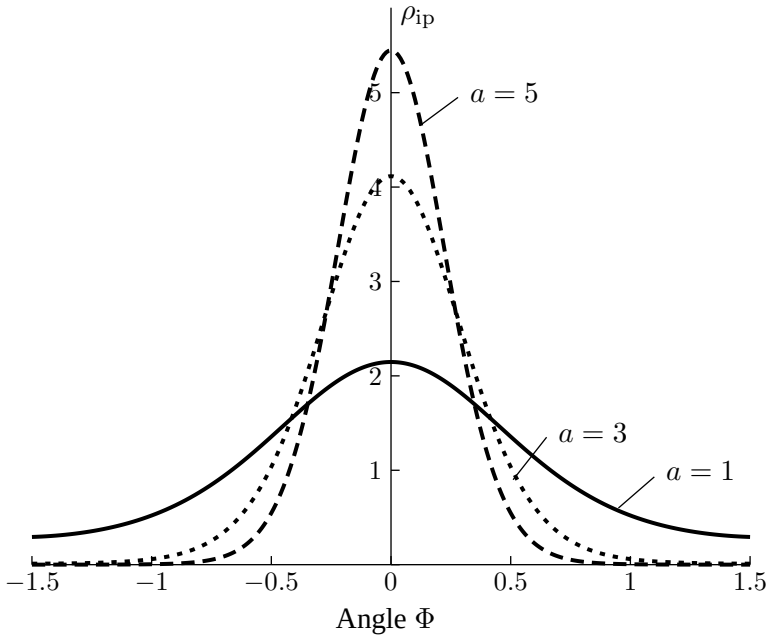

Figure 2.3: The von Mises distribution (2.25) plotted against Φ for three different values of the parameter a: $(1,3,5)$, corresponding to the continuous, short dashed and long dashed curves, respectively. For $a = 0$ we have $\rho_{\text{ip}} \equiv 1$, while for $a \to \infty$, ρ_{ip} becomes a delta function.

For the distribution (2.30), a closed form expression for κ_{op} from (2.13) is obtained in the form

$$\kappa_{\text{op}} = \frac{1}{2} - \frac{1}{8b} + \frac{1}{4}\sqrt{\frac{2}{\pi b}}\frac{\exp(-2b)}{\operatorname{erf}(\sqrt{2b})}. \tag{2.32}$$

Figure 2.4 shows a plot of κ_{op} as a function of the concentration parameter b. Note in particular that $\kappa_{\text{op}} = 1/3$ when $b = 0$.

We use maximum likelihood estimates to obtain the parameters a and b in the PDFs, $\rho_{\text{ip}}(\Phi)$ and $\rho_{\text{op}}(\Theta)$, from the angular data sets of [19]. Although it is possible to determine the parameters of a PDF by minimizing the sum of squared errors, this method has several disadvantages, as pointed out in [19], and hence we prefer to identify the parameters by using a maximum likelihood estimate. In Figure 2.5 we show experimental data from the adventitia of a human non-atherosclerotic abdominal aorta obtained from picrosirius-polarization, in combination with a universal stage [19]. To produce the fit we used the maximum likelihood estimate to obtain the concentration parameters a and b. In Figure 2.5(a) we show the in-plane bi-modal distribution of ρ_{ip} of Φ with $\alpha = \pm 47.99^\circ$ giving $a = 2.54$, which is obtained from (2.25) using $\Phi + \alpha$ and $\Phi - \alpha$ instead of Φ. In Figure 2.5(b) we show the out-of-plane probability density ρ_{op} of Θ obtained from (2.30), where $b = 19.44$.

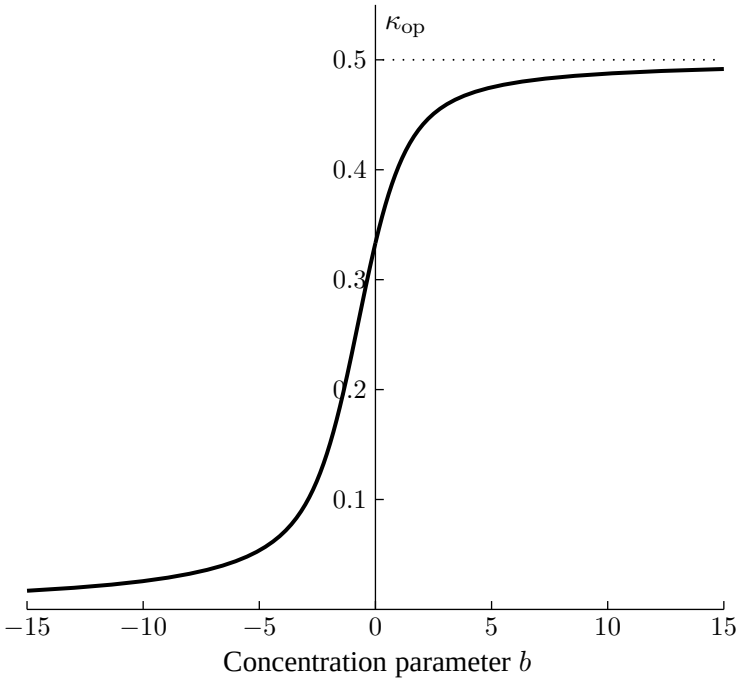

Figure 2.4: Plot of κ_{op} vs. the concentration parameter b according to equation (2.32). Note that $0 \leq \kappa_{\text{op}} \leq 1/2$ and $\kappa_{\text{op}} = 1/3$ when $b = 0$.

2.2.2 Special Cases of Fiber Dispersions

Our model includes several existing dispersion models as special cases of (2.20), which are discussed in the following section.

Transversely Isotropic Dispersion

In [134] we considered a transversely isotropic dispersion for which $\mathbf{H}$ has the form

$$\mathbf{H} = \kappa \mathbf{I} + (1 - 3\kappa)\mathbf{M} \otimes \mathbf{M}, \tag{2.33}$$

where κ is a single dispersion parameter associated with a transversely isotropic dispersion about $\mathbf{M}$. Note that here we are taking $\mathbf{M}$ to lie in the $(\mathbf{e}_1, \mathbf{e}_2)$ plane (see Figure 2.2). In [134] κ had the form

$$\kappa = \frac{1}{4} \int_0^{\pi} \rho(\Theta_\kappa) \sin^3 \Theta_\kappa \mathrm{d}\Theta_\kappa,$$

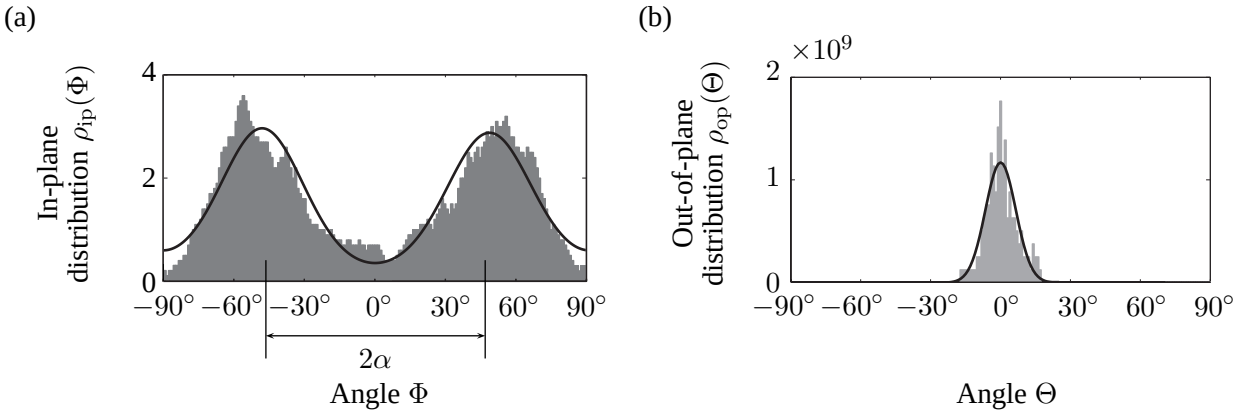

Figure 2.5: (a) Probability density $\rho_{ip}(\Phi+\alpha)$, $\rho_{ip}(\Phi-\alpha)$ plotted against Φ with the concentration parameter $a = 2.54$ and with two mean fiber directions located at $\alpha = \pm 47.99^\circ$; (b) probability density $\rho_{op}(\Theta)$ against Θ with the parameter $b = 19.44$.

where Θ_κ is measured from $\mathbf{M}$ and is different from the Θ used here. The connection between Θ_κ and Θ is obtained from $\mathbf{M}\cdot\mathbf{N} = \cos\Theta_\kappa$, with $\mathbf{N}$ given by (2.5) and $\mathbf{M} = \cos\alpha\,\mathbf{e}_1 + \sin\alpha\,\mathbf{e}_2$, in the form $\cos\Theta_\kappa = \cos\Theta\cos(\Phi-\alpha)$.

Equation (2.33) is recovered as a special case of (2.20) by taking $\kappa = 1-2\kappa_{op}$, which corresponds to $A = \kappa$, $B = 1-3\kappa$.

Perfect Alignment

If both concentration parameters a and b become infinite, there is no dispersion in either plane and we obtain the model proposed in [39]. With $a \to \infty$, ρ_{ip} becomes an in-plane delta function, and with $b \to \infty$ we have $\kappa_{op} \to 1/2$. The structure tensor is then $\mathbf{H} = \mathbf{M}\otimes\mathbf{M}$, and all fibers are oriented in the in-plane direction of $\mathbf{M}$. This corresponds to $A = 0$, $B = 1$ in (2.20).

Isotropic Dispersion

An isotropic fiber dispersion is represented by a uniform dispersion in each plane, meaning that $\rho(\Phi,\Theta)$ is independent of Φ and Θ, with $\rho_{ip} = \rho_{op} = 1$, so that, for the von Mises distributions, $a = b = 0$, while $\kappa_{op} = 1/3$, and the structure tensor is given by $\mathbf{H} = \frac{1}{3}\mathbf{I}$. Thus, there is no preferred direction ($\kappa = 1/3$), with $A = 1/3$, $B = 0$ in (2.20).

Table 2.2: Special cases of the present model based on the von Mises distributions (2.25) and (2.30). The abbreviations used are: TI = transversely isotropic dispersion, ID = isotropic dispersion, PA = perfect alignment, PD = planar dispersion, PI = planar isotropic dispersion.

Case	Conc. Parameter	Dispersion Parameter	Structure Tensor $\mathbf{H}$	Reference
TI	–	$\kappa = 1-2\kappa_{\text{op}}$	$\kappa\mathbf{I}+(1-3\kappa)\mathbf{M}\otimes\mathbf{M}$	[134]
PA	$a\to\infty, b\to\infty$	$\kappa_{\text{op}}\to 1/2$, $\kappa = 0$	$\mathbf{M}\otimes\mathbf{M}$	[39]
ID	$a=b=0$	$\kappa_{\text{op}}=\kappa=1/3$	$\frac{1}{3}\mathbf{I}$	[18, 134]
PD	$b\to\infty$	$\kappa_{\text{op}}\to 1/2$, $\kappa=\bar{\kappa}_{22}$	$\kappa\mathbf{1}+(1-2\kappa)\mathbf{M}\otimes\mathbf{M}$	[159, 169]
PI	$a\to 0, b\to\infty$	$\kappa_{\text{op}}\to 1/2$	$\frac{1}{2}\mathbf{1}$	[116, 169]

Planar Dispersion

A dispersion with fibers oriented only in-plane was presented in [159, 169]. In this case there is no out-of-plane contribution to $\mathbf{H}$, which can be written as

$$\mathbf{H} = \kappa\mathbf{1} + (1-2\kappa)\mathbf{M}\otimes\mathbf{M}, \tag{2.34}$$

where $\mathbf{1}$ is the two-dimensional identity in the considered plane with the normalization and dispersion parameter given by

$$\frac{1}{\pi}\int_{-\pi/2}^{\pi/2}\rho(\Theta)\mathrm{d}\Theta = 1, \qquad \kappa = \frac{1}{\pi}\int_{-\pi/2}^{\pi/2}\rho(\Theta)\sin^2\Theta\mathrm{d}\Theta. \tag{2.35}$$

Note that the normalization $(2.35)_1$ is equivalent to (2.11) bearing in mind the different range of angles used, and κ is equivalent to $\bar{\kappa}_{22}$ as defined in $(2.15)_2$. The in-plane PDF $\rho(\Theta)$ satisfies $\rho(-\Theta)=\rho(\Theta)$. For the von Mises distribution (2.30) this corresponds to $b\to\infty$ and $\kappa_{\text{op}}\to 1/2$. Equation (2.34) is obtained from (2.20) by setting $A=\kappa=\bar{\kappa}_{22}$, $B=1-2\kappa$. Note that this is a two-dimensional distribution but its application is not restricted to use in 2D.

Planar Isotropic Dispersion

If a dispersion features perfect out-of-plane alignment, $b\to\infty$ and $\kappa_{\text{op}}\to 1/2$, and is fully dispersed in-plane so that $a\to 0$, $\rho_{\text{ip}}=1$, then it is planar isotropic. For this case, the structure tensor is simply $\mathbf{H}=\frac{1}{2}\mathbf{1}$, corresponding to $A=1/2$, $B=0$ in (2.20).

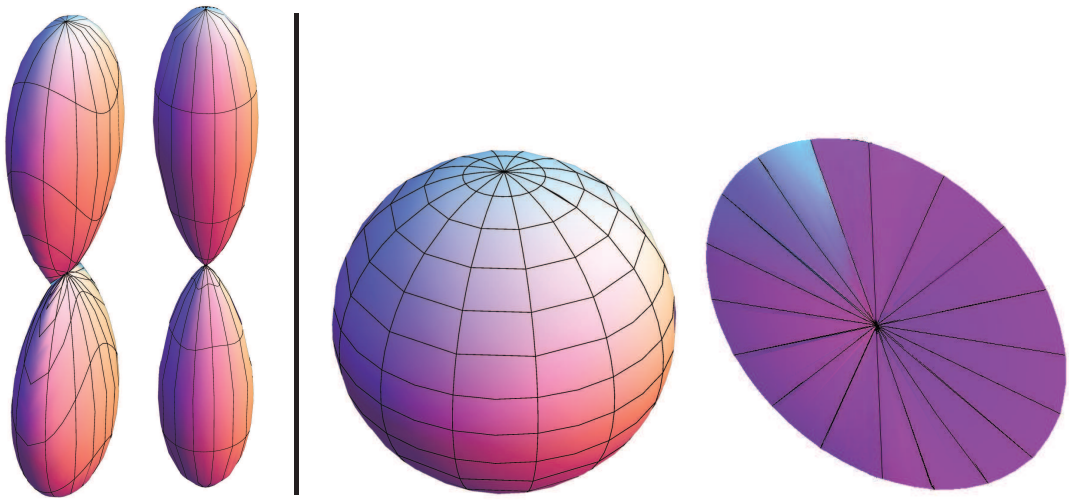

(a) (b) (c) (d) (e)

Figure 2.6: Visualization of the fiber dispersion defined by $\rho(\mathbf{N})\,\mathbf{N}$, with $\rho = \rho_{\text{ip}}(\Phi)\rho_{\text{op}}(\Theta)$ according to (2.25) and (2.30), where the distance from the centre to the surface represents the probability of finding a fiber in the direction $\mathbf{N}$. The plots have been scaled differently and represent (a) a non-rotationally symmetric dispersion, (b) a rotationally symmetric dispersion, (c) perfectly aligned fibers, (d) a 3D isotropic fiber dispersion and (e) a planar fiber dispersion. The planar isotropic case corresponds to a circle in (e).

Summary of the Special Cases

The special cases discussed above are summarized in Table 2.2. Figure **??** is a visualization of $\rho(\mathbf{N})\mathbf{N}$ for (a) the general case for which $\mathbf{H}$ is given by equation (2.20), (b) the transversely isotropic dispersion given in Section 2.2.2 with $\mathbf{H}$ given by (2.33), (c) the case of perfect alignment according to Section 2.2.2, (d) the isotropic case according to Section 2.2.2 and (e) the case of planar dispersion given by equation (2.34).

2.3 Continuum Mechanical Framework

We consider a (stress-free) reference configuration, denoted Ω_0, and a deformed (spatial) configuration, denoted Ω. The deformation map $\chi(\mathbf{X})$ transforms a material point $\mathbf{X} \in \Omega_0$ into a spatial point $\mathbf{x} \in \Omega$. With this deformation map we define the deformation gradient $\mathbf{F}(\mathbf{X}) = \partial\chi(\mathbf{x})/\partial\mathbf{X}$ and its determinant $J = \det\mathbf{F}(\mathbf{X})$, where J is the local volume ratio; we require $J > 0$.

Following [171, 172] we apply the multiplicative decomposition of $\mathbf{F}$ into a spherical (dilatational) part $J^{1/3}\mathbf{I}$ and a unimodular (distortional) part $\overline{\mathbf{F}} = J^{-1/3}\mathbf{F}$, with $\det\overline{\mathbf{F}} = 1$. We define the right Cauchy–Green tensor and its modified counterpart as $\mathbf{C} = \mathbf{F}^{\mathrm{T}}\mathbf{F}$ and $\overline{\mathbf{C}} = \overline{\mathbf{F}}^{\mathrm{T}}\overline{\mathbf{F}}$, respectively, with the related invariants $I_1 = \mathrm{tr}\,\mathbf{C}$ and $\bar{I}_1 = \mathrm{tr}\,\overline{\mathbf{C}}$.

Since we treat an artery as an elastic material, we assume the existence of a strain-energy function $\Psi(\mathbf{C}, \mathbf{H}_4, \mathbf{H}_6)$ that depends on the macroscopic deformation through $\mathbf{C}$ and the underlying tissue structure through the structure tensors $\mathbf{H}_4, \mathbf{H}_6$, which describe the fiber alignment and dispersion for two fiber families. Based on (2.20) these are defined by

$$\mathbf{H}_i = A\mathbf{I} + B\mathbf{M}_i \otimes \mathbf{M}_i + (1 - 3A - B)\mathbf{M}_{\mathrm{n}} \otimes \mathbf{M}_{\mathrm{n}}, \qquad i = 4, 6 \tag{2.36}$$

and $\mathbf{M}_4$ and $\mathbf{M}_6$ lie in the $(\mathbf{e}_1, \mathbf{e}_2)$ plane, and $\mathbf{M}_{\mathrm{n}}$ normal to that plane.

For computational purposes, we assume that it is possible to split the strain-energy function into two parts as $\Psi(\mathbf{C}, \mathbf{H}_4, \mathbf{H}_6) = \Psi_{\mathrm{vol}}(J) + \Psi_{\mathrm{iso}}(\overline{\mathbf{C}}, \mathbf{H}_4, \mathbf{H}_6)$, as shown in [173], [134]. The function Ψ_{vol} is a purely volumetric contribution while Ψ_{iso} represents the energy contribution of an isochoric (volume preserving) deformation through $\overline{\mathbf{C}}$. The second Piola–Kirchhoff stress tensor $\mathbf{S}$ is given by $\mathbf{S} = 2\partial\Psi/\partial\mathbf{C}$. Using the decoupled form of Ψ we can identify two stress contributions so that $\mathbf{S} = \mathbf{S}_{\mathrm{vol}} + \mathbf{S}_{\mathrm{iso}}$. Using well-known results from tensor analysis (see, e.g., [173]), and the chain rule we obtain

$$\mathbf{S}_{\mathrm{vol}} = pJ\mathbf{C}^{-1}, \qquad \mathbf{S}_{\mathrm{iso}} = J^{-2/3}\mathrm{Dev}\overline{\mathbf{S}}, \tag{2.37}$$

where $p = \mathrm{d}\Psi_{\mathrm{vol}}(J)/\mathrm{d}J$ is the constitutive equation for the hydrostatic pressure and

$$\overline{\mathbf{S}} = 2\frac{\partial\Psi_{\mathrm{iso}}}{\partial\overline{\mathbf{C}}} \tag{2.38}$$

is the so-called 'fictitious' isochoric second Piola–Kirchhoff stress tensor. The deviator in the Lagrangian configuration is defined by $\mathrm{Dev}(\bullet) = \mathbb{P} : (\bullet)$, where $\mathbb{P} = \mathbb{I} - \frac{1}{3}\mathbf{C}^{-1} \otimes \mathbf{C}$ is a projection tensor that furnishes the correct deviatoric operator in the Lagrangian setting, and $(\mathbb{I})_{ABCD} = \frac{1}{2}(\delta_{AC}\delta_{BD} + \delta_{AD}\delta_{BC})$ is a fourth-order identity tensor.

The related elasticity tensor $\mathbb{C}$ in the Lagrangian description is written in the decoupled form

$$\mathbb{C} = 2\frac{\partial\mathbf{S}(\mathbf{C})}{\partial\mathbf{C}} = \mathbb{C}_{\mathrm{vol}} + \mathbb{C}_{\mathrm{iso}}, \quad \mathbb{C}_{\mathrm{vol}} = 2\frac{\partial\mathbf{S}_{\mathrm{vol}}}{\partial\mathbf{C}}, \quad \mathbb{C}_{\mathrm{iso}} = 2\frac{\partial\mathbf{S}_{\mathrm{iso}}}{\partial\mathbf{C}}. \tag{2.39}$$

According to [173] we have the specification

$$\mathbb{C}_{\mathrm{vol}} = J\tilde{p}\mathbf{C}^{-1} \otimes \mathbf{C}^{-1} - 2Jp\mathbf{C}^{-1} \odot \mathbf{C}^{-1} \tag{2.40}$$

and

$$\mathbb{C}_{\text{iso}} = \mathbb{P} : \overline{\mathbb{C}} : \mathbb{P}^{\text{T}} + \frac{2}{3}\text{Tr}(J^{-2/3}\overline{\mathbf{S}})\tilde{\mathbb{P}} - \frac{2}{3}(\mathbf{C}^{-1} \otimes \mathbf{S}_{\text{iso}} + \mathbf{S}_{\text{iso}} \otimes \mathbf{C}^{-1}). \tag{2.41}$$

In (2.40) we have used the notation $\mathbf{C}^{-1} \odot \mathbf{C}^{-1} = -\partial \mathbf{C}^{-1}/\partial \mathbf{C}$, where the symbol $\odot$ denotes the tensor product according to the rule

$$(\mathbf{C}^{-1} \odot \mathbf{C}^{-1})_{ABCD} = \frac{1}{2}(C^{-1}_{AC} C^{-1}_{BD} + C^{-1}_{AD} C^{-1}_{BC}), \tag{2.42}$$

and the scalar function $\tilde{p}$ is defined by $\tilde{p} = p + J\text{d}p/\text{d}J$ with the constitutive equation for p given in the line after equation (2.37). In (2.41) we have also used the definitions

$$\overline{\mathbb{C}} = 4J^{-4/3}\frac{\partial^2 \Psi_{\text{iso}}(\overline{\mathbf{C}})}{\partial \overline{\mathbf{C}} \partial \overline{\mathbf{C}}}, \qquad \text{Tr}(\bullet) = (\bullet) : \mathbf{C}, \qquad \tilde{\mathbb{P}} = \mathbf{C}^{-1} \odot \mathbf{C}^{-1} - \frac{1}{3}\mathbf{C}^{-1} \otimes \mathbf{C}^{-1}, \tag{2.43}$$

where $\overline{\mathbb{C}}$ is the fourth-order fictitious elasticity tensor, $\text{Tr}(\bullet)$ is the trace and $\tilde{\mathbb{P}}$ is the modified projection tensor of fourth-order. The related spatial stress and elasticity tensors may be derived by push-forward operations on (2.37) and $(2.39)_1$, respectively [173]. It should be noted here that the compressible formulation is introduced for computational purposes, and the incompressibility condition has to be enforced by a numerical scheme, one example of which is the Augmented Lagrangian method (see, e.g., [174]).

We emphasize that for a specific material we need to specify Ψ_{iso} and hence to calculate its derivatives with respect to $\overline{\mathbf{C}}$, which affects the two expressions (2.38) and $(2.43)_1$. In the next subsection such a specification is provided.

2.3.1 Anisotropic Strain-energy Function

Each of the structure tensors $\mathbf{H}_4$ and $\mathbf{H}_6$ depends on two dispersion parameters. We assume that these are the same for each fiber family. Our approach follows the work of [39] in which the contributions Ψ_{g} and Ψ_{f} of the ground matrix (non-collagenous material) and the fibers to the strain energy are added. The artery is treated as an incompressible, elastic and fiber-reinforced material with the fiber dispersion accounted for both in-plane and out-of-plane. Hence, superposition of energies reads

$$\Psi_{\text{iso}} = \Psi_{\text{g}}(\overline{\mathbf{C}}) + \sum_{i=4,6} \Psi_{\text{f}i}(\overline{\mathbf{C}}, \mathbf{H}_i). \tag{2.44}$$

Following [39, 175] we model the ground substance with a neo-Hookean material $\Psi_{\text{g}} = c(\bar{I}_1 - 3)/2$, where the parameter c is the shear modulus in the reference configuration. For the fiber contributions $\Psi_{\text{f}i}$, we adopt the exponential functions [134]

$$\Psi_{\text{f}i}(\overline{\mathbf{C}}, \mathbf{H}_i) = \frac{k_1}{2k_2}[\exp(k_2 \overline{E}_i^2) - 1], \quad i = 4, 6, \tag{2.45}$$

Table 2.3: Parameters for the proposed model.

Parameter	Interpretation	Range	Identification
c [kPa]	Stiffness of (isotropic) ground matrix	$(0,\infty)$	Mechanical tests
k_1 [kPa]	Stress-like parameter	$[0,\infty)$	
k_2 [–]	Dimensionless parameter	$[0,\infty)$	
κ_{ip}	Dispersion in-plane	$[0,1]$	Histology/Imaging
κ_{op}	Dispersion out-of-plane	$[0,1/2]$	
$\mathbf{M}_4$, $\mathbf{M}_6$	Mean fiber directions	$\alpha \in [0,\pi/2]$	
$\mathbf{M}_{\text{n}}$	Normal to the mean fiber plane	–	

where k_1 is a parameter with the dimensions of stress and k_2 a dimensionless parameter, while

$$\overline{E}_i = \mathbf{H}_i : (\overline{\mathbf{C}} - \mathbf{I}) \tag{2.46}$$

is a Green–Lagrange strain-like quantity which can be interpreted as an averaged or weighted fiber strain, depending on the fiber dispersion through the structure tensor $\mathbf{H}_i$ and the (isochoric) macroscopic deformation through $\overline{\mathbf{C}}$.

Since $\text{tr}\mathbf{H}_i = 1$, we can write $\overline{E}_i = \mathbf{H}_i : \overline{\mathbf{C}} - 1$. Using the definitions (2.36) of the structure tensors $\mathbf{H}_4$ and $\mathbf{H}_6$ we obtain

$$\overline{E}_i = A\bar{I}_1 + B\bar{I}_i + (1 - 3A - B)\bar{I}_{\text{n}} - 1, \tag{2.47}$$

where

$$\bar{I}_i = \overline{\mathbf{C}} : \mathbf{M}_i \otimes \mathbf{M}_i, \quad i = 4,6, \qquad \bar{I}_{\text{n}} = \overline{\mathbf{C}} : \mathbf{M}_{\text{n}} \otimes \mathbf{M}_{\text{n}}. \tag{2.48}$$

The invariants $I_i = J^{2/3}\bar{I}_i$ and $I_{\text{n}} = J^{2/3}\bar{I}_{\text{n}}$ are the squares of the stretches in the directions $\mathbf{M}_i$ and $\mathbf{M}_{\text{n}}$, respectively. A summary of the parameters used is provided in Table 2.3.

The strain-energy function used in the proposed model reads

$$\Psi_{\text{iso}} = \frac{c}{2}(\bar{I}_1 - 3) + \frac{k_1}{2k_2} \sum_{i=4,6} \left\{ \exp\left[k_2 \overline{E}_i^2\right] - 1 \right\}. \tag{2.49}$$

Following [39], we make the common assumption that the fibers do not resist any compression and are only active in tension. The invariants I_i are used as switches between fiber compression and tension so that the anisotropic part $\Psi_{\text{f}i}$ only contributes to the strain energy when $I_4 > 1$ or $I_6 > 1$. If one or more of these conditions is not satisfied then the relevant part of the anisotropic function is omitted from (2.49). For example, if I_4 and I_6 are less than (or equal to) 1, then the tissue response is purely isotropic. For discussion of subtle points regarding the choice of switching criteria, see [149].

In the expressions for the stress and the elasticity tensor we need to calculate $\partial\Psi_{\rm iso}/\partial\overline{\mathbf{C}}$ and $\partial^2\Psi_{\rm iso}/\partial\overline{\mathbf{C}}\partial\overline{\mathbf{C}}$. By using the chain rule these are obtained as

$$\frac{\partial\Psi_{\rm iso}}{\partial\overline{\mathbf{C}}} = c\mathbf{I} + \psi_i'\mathbf{H}_i, \qquad \frac{\partial^2\Psi_{\rm iso}}{\partial\overline{\mathbf{C}}\partial\overline{\mathbf{C}}} = \psi_i''\mathbf{H}_i\otimes\mathbf{H}_i, \quad i=4,6, \tag{2.50}$$

where $\mathbf{H}_i$ is given by (2.36), and we have introduced the notations

$$\psi_i' = \frac{\partial\Psi_{\rm iso}}{\partial\overline{E}_i} = k_1\overline{E}_i\exp(k_2\overline{E}_i^2), \qquad \psi_i'' = \frac{\partial^2\Psi_{\rm iso}}{\partial\overline{E}_i^2} = k_1(1+2k_2\overline{E}_i^2)\exp(k_2\overline{E}_i^2). \tag{2.51}$$

2.4 Representative Examples

Having identified the *dispersion* parameters of the model in the previous section, we now identify the *mechanical* parameters by fitting the constitutive model to uniaxial data. The parameters are then used to implement the proposed constitutive model into the finite element analysis program FEAP, the results of which for a simple biaxial extension of an 8 element cube are compared with the analytical (MATLAB) result. Finally, numerical results are obtained for the stress distribution in the non-homogeneous extension of strips of an adventitial layer cut out along the axial and circumferential directions.

2.4.1 Parameter Fitting to Experimental Data

In this example we consider the purely incompressible formulation where the strain-energy function is characterized by $\Psi = \Psi(\mathbf{C}, \mathbf{H}_4, \mathbf{H}_6)$. The second Piola–Kirchhoff stress tensor $\mathbf{S}$ is then given by

$$\mathbf{S} = 2\frac{\partial\Psi}{\partial\mathbf{C}} - p\mathbf{C}^{-1} = 2\left(\frac{\partial\Psi}{\partial I_1}\mathbf{I} + \sum_{i=4,6}\frac{\partial\Psi}{\partial I_i}\mathbf{M}_i\otimes\mathbf{M}_i + \frac{\partial\Psi}{\partial I_{\rm n}}\mathbf{M}_{\rm n}\otimes\mathbf{M}_{\rm n}\right) - p\mathbf{C}^{-1}, \tag{2.52}$$

where p in this case denotes the Lagrange multiplier required to enforce incompressibility. From (2.52) the Cauchy stress tensor can be computed simply by $\sigma = \mathbf{F}\mathbf{S}\mathbf{F}^{\rm T}$.

The strain-energy function in the present formulation reads

$$\Psi = \frac{c}{2}(I_1-3) + \frac{k_1}{2k_2}\sum_{i=4,6}\left\{\exp\left[k_2E_i^2\right]-1\right\}, \tag{2.53}$$

where

$$E_i = AI_1 + BI_i + (1-3A-B)I_{\rm n} - 1, \qquad i=4,6. \tag{2.54}$$

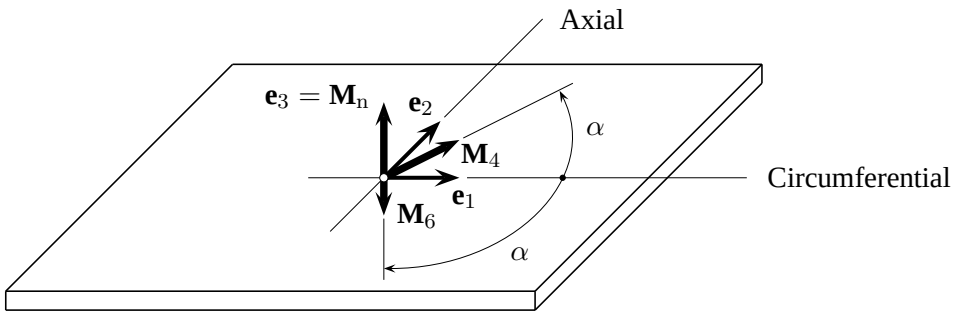

Figure 2.7: A specimen with two symmetric fiber families with mean fiber directions $\mathbf{M}_4$ and $\mathbf{M}_6$ lying in the circumferential/axial plane, each making an angle α with the circumferential direction. The normal direction to the plane is $\mathbf{M}_\mathrm{n}$.

The anisotropic term in (2.53) only contributes when the fibers are extended, i.e. when $I_4 > 1$ or $I_6 > 1$. For the case that one or more of these conditions is not satisfied then the relevant part is omitted from (2.53).

We now consider a tissue specimen with two fiber families in the reference configuration with mean directions illustrated in Figure 2.7. The unit vectors $\mathbf{M}_4$ and $\mathbf{M}_6$, which are symmetrically disposed in the circumferential/axial plane, each make an angle α with the circumferential direction, so that

$$[\mathbf{M}_4] = [\cos\alpha,\ \sin\alpha,\ 0]^\mathrm{T}, \qquad [\mathbf{M}_6] = [\cos\alpha,\ -\sin\alpha,\ 0]^\mathrm{T}, \tag{2.55}$$

while the normal direction to the plane is $[\mathbf{M}_\mathrm{n}] = [0,\ 0,\ 1]^\mathrm{T}$. The deformation gradient matrix and the right Cauchy–Green matrix are

$$[\mathbf{F}] = \mathrm{diag}[\lambda_1, \lambda_2, \lambda_3], \qquad [\mathbf{C}] = \mathrm{diag}[\lambda_1^2, \lambda_2^2, \lambda_3^2], \tag{2.56}$$

where λ_1, λ_2, λ_3 denote the principal stretches. Hence, the required invariants read

$$I_1 = \lambda_1^2 + \lambda_2^2 + \lambda_3^2, \tag{2.57}$$

$$I_i = \mathbf{C} : (\mathbf{M}_i \otimes \mathbf{M}_i) = \lambda_1^2 \cos^2\alpha + \lambda_2^2 \sin^2\alpha, \quad i = 4, 6, \tag{2.58}$$

$$I_\mathrm{n} = \mathbf{C} : (\mathbf{M}_\mathrm{n} \otimes \mathbf{M}_\mathrm{n}) = \lambda_3^2. \tag{2.59}$$

Since I_i is the same for $i = 4$ and 6 we obtain $\psi_4' = \psi_6'$, where here, in analogy with $(2.51)_1$, $\psi_i' = k_1 E_i \exp(k_2 E_i^2)$, $i = 4, 6$. By using E_i in the scalar stress function (2.53) we obtain the derivatives of the strain-energy function as

$$\frac{\partial \Psi}{\partial I_1} = \frac{c}{2} + 2A\psi_4', \qquad \frac{\partial \Psi}{\partial I_i} = B\psi_i', \quad i = 4, 6, \qquad \frac{\partial \Psi}{\partial I_\mathrm{n}} = 2(1 - 3A - B)\psi_4'. \tag{2.60}$$

Table 2.4: Summary of material and structural parameters.

	Material parameters			Structural parameters		
	c [kPa]	k_1 [kPa]	k_2 [–]	κ_{ip} [–]	κ_{op} [–]	α [$^\circ$]
Value	10.07	5.89	21.62	0.116	0.493	$\pm 47.99^\circ$
R^2	0.998			0.877	0.916	[–]

Hence, the non-zero components of the Cauchy stress are

$$\sigma_{11} = [c+4(A+B\cos^2\alpha)\psi_4']\lambda_1^2 - p, \tag{2.61}$$

$$\sigma_{22} = [c+4(A+B\sin^2\alpha)\psi_4']\lambda_2^2 - p, \tag{2.62}$$

$$\sigma_{33} = [c+4(1-2A-B)\psi_4']\lambda_3^2 - p. \tag{2.63}$$

The constants A and B can be deduced from (2.21) and (2.22) as

$$A = 2\kappa_{\text{op}}\kappa_{\text{ip}}, \qquad B = 2\kappa_{\text{op}}(1-2\kappa_{\text{ip}}). \tag{2.64}$$

Together with the incompressibility condition ($\lambda_1\lambda_2\lambda_3 = 1$), the implicit equations (2.61)–(2.63) with $\sigma_{22} = \sigma_{33} = 0$ can then be used to obtain p, λ_2 and λ_3 in terms of λ_1, thus giving an expression for σ_{11} in terms of λ_1, the material parameters c, k_1 and k_2 and the structural parameters κ_{ip}, κ_{op} and α.

To determine the material parameters of our model, we use the structural data provided in Figure 2.5 (mean fiber angle α and concentration parameters a, b) and experimental data (from uniaxial tension tests) from the adventitia of a human non-atherosclerotic abdominal aorta. A least–squares objective function is chosen as the L^2-norm of the error between the model prediction of the Cauchy stress in the circumferential and the axial directions, and the corresponding experimental data. We use the function LSQNONLIN in MATLAB[1], which utilizes the Levenberg–Marquardt algorithm to find the minimum. The dispersion parameters κ_{ip} from $(2.27)_2$ with the value of a, and κ_{op} from (2.32) with the value of b can be determined from the imaging data provided in Figure 2.5. Imaging and material data were obtained from different but comparable tissues.

To quantify the goodness of the fit, we calculate the coefficient of determination R^2, which is given by

$$R^2 = 1 - \frac{S_{\text{err}}}{S_{\text{tot}}}, \tag{2.65}$$

where S_{err} and S_{tot} are the sums of squares of the differences between model/experiment and the mean of experiment/experiment, respectively [176]. We obtained a good fit with $R^2 = 0.998$. The parameters identified are listed in Table 2.4. Figure 2.8 shows the result of fitting the proposed model to data from uniaxial tension tests.

[1] Version R2010b, by The MathWorks Inc., Massachusetts, USA

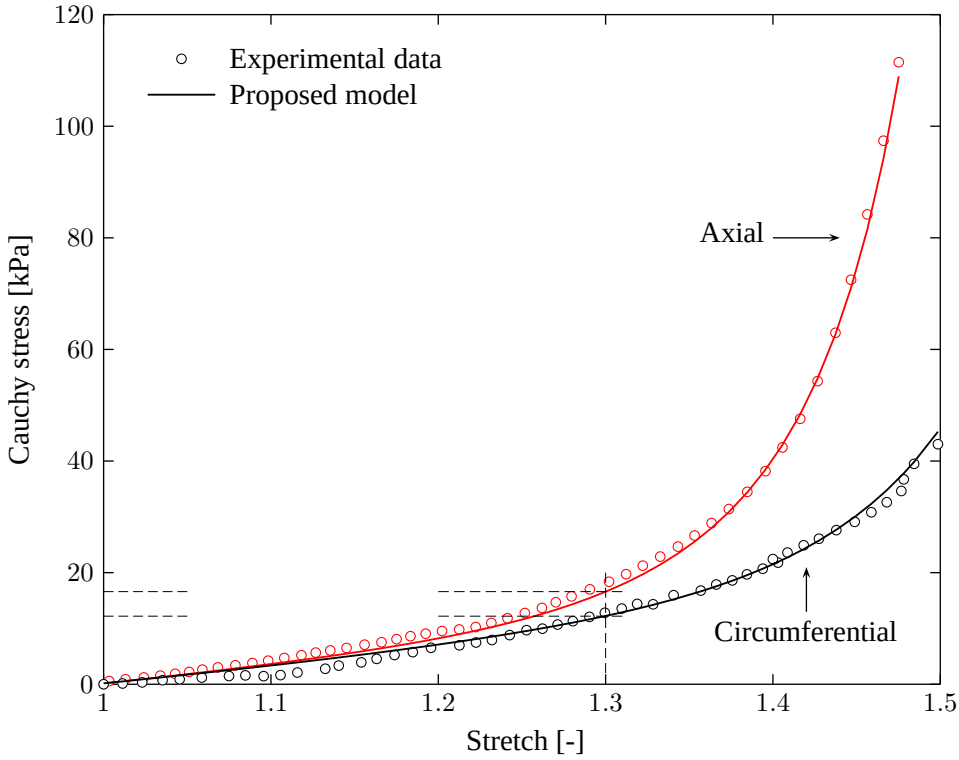

Figure 2.8: Fitting of the proposed model to the results of a uniaxial tension test. The good quality of fit is reflected in the high coefficient of determination, $R^2 = 0.998$. The model (Cauchy) stresses at a stretch of 1.3 are 16.6 (axial) and 12.2 kPa (circumferential) – see also Figure 2.11.

2.4.2 Biaxial Extension: Comparison of MATLAB and Finite Element Results

In this section we demonstrate the efficacy of the proposed constitutive model by using eight hexahedral $Q1/P0$ finite elements for a cube ($10 \times 10 \times 10$), which is reinforced by two symmetric fiber families, as depicted in Figure 2.7. The cube is subjected to homogeneous biaxial extension in the $1,2$-plane, which here we call 'in-plane', as shown in Figure 2.9; the $2,3$-plane we call 'out-of-plane'. The mesh is unstructured according to Figure 2.9. The material parameters used are those documented in Table 2.4. We investigate four different cases of fiber dispersion: (I) structural parameters taken from Table 2.4, which is the reference case; (II) high alignment out-of-plane and isotropy in-plane; (III) less alignment out-of-plane and isotropy in-plane; (IV) isotropy in both out-of-plane and in-plane. For a summary see Table 2.5.

The maximum of each stretch, (λ_1, λ_2) in the 1 and 2 direction, respectively, is 1.15 and the corresponding Cauchy stresses $(\sigma_{11}, \sigma_{22})$ are computed from equations (2.61)–(2.63) using MATLAB. In addition, these relationships are compared with results obtained from

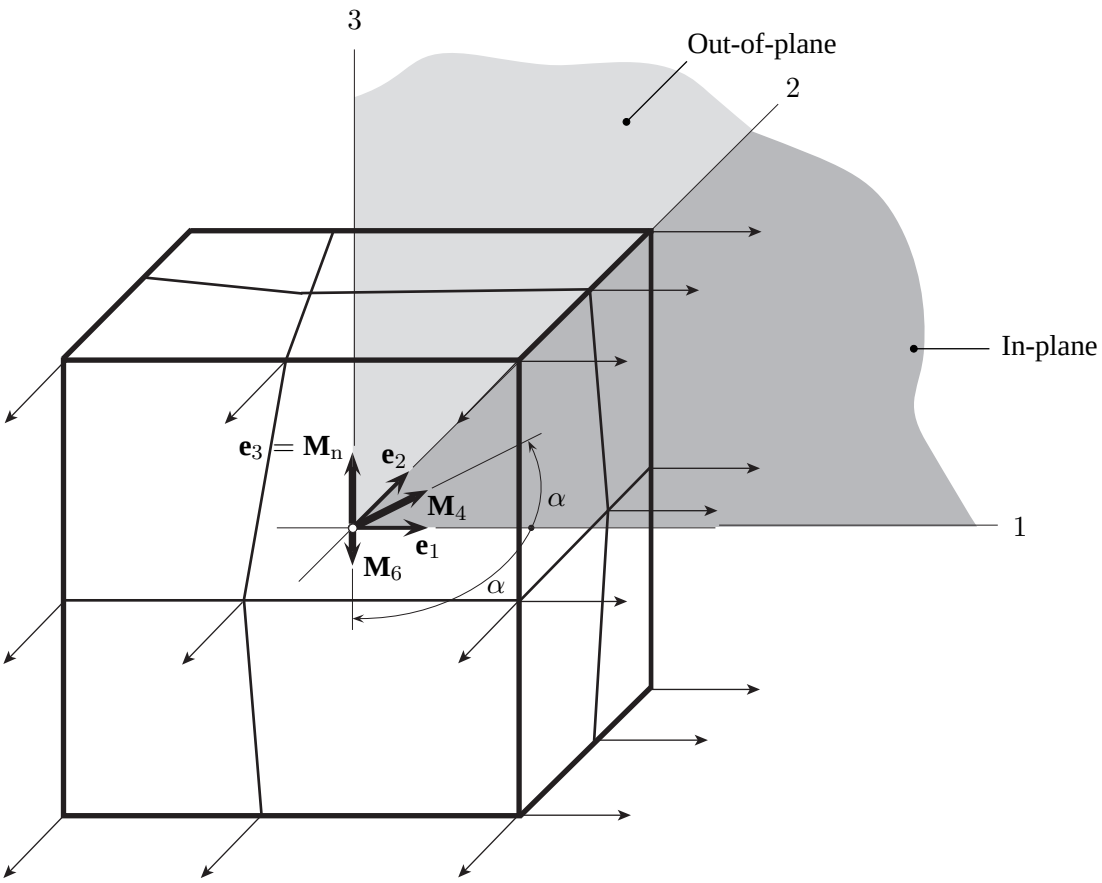

Figure 2.9: Unstructured mesh of a cube discretized by eight hexahedral finite elements. The cube is reinforced by two symmetric fiber families and subjected to homogeneous equibiaxial extension in the $1,2$-plane, illustrated by arrows.

a finite element computation using FEAP [135]. The cube is stretched simultaneously in the 1 and 2-directions under displacement-driven conditions using the Newton–Raphson method. Figures 2.10(a),(b) show plots of the Cauchy stresses σ_{11} and σ_{22} versus the stretches λ_1 and λ_2, respectively. Note that for case (IV) the stresses in the 1 and 2-directions are the same since the in-plane and out-of-plane dispersions are isotropic.

2.4.3 Extension of Adventitial Strips

In this section we illustrate the results of the finite element implementation of the proposed constitutive model, simulating uniaxial extension tests related to experiments on strips performed in our lab in Graz. The strips were taken from an adventitial layer cut out along the axial and circumferential direction of a human non-atherosclerotic abdominal aorta.

Table 2.5: Four different cases of fiber dispersion for the homogeneous biaxial extension of a cube. The material parameters are taken from Table 2.4.

Case	Description	Dispersion parameters
I	Structural parameters from table 2.4	$\kappa_{\text{ip}} = 0.116$, $\kappa_{\text{op}} = 0.493$
II	High alignment out-of-plane and isotropy in-plane	$\kappa_{\text{ip}} = 0.5$, $\kappa_{\text{op}} = 0.48$
III	Less alignment out-of-plane and isotropy in-plane	$\kappa_{\text{ip}} = 0.5$, $\kappa_{\text{op}} = 0.45$
IV	Isotropy in out-of-plane and in-plane	$\kappa_{\text{ip}} = 0.5$, $\kappa_{\text{op}} = 1/3$

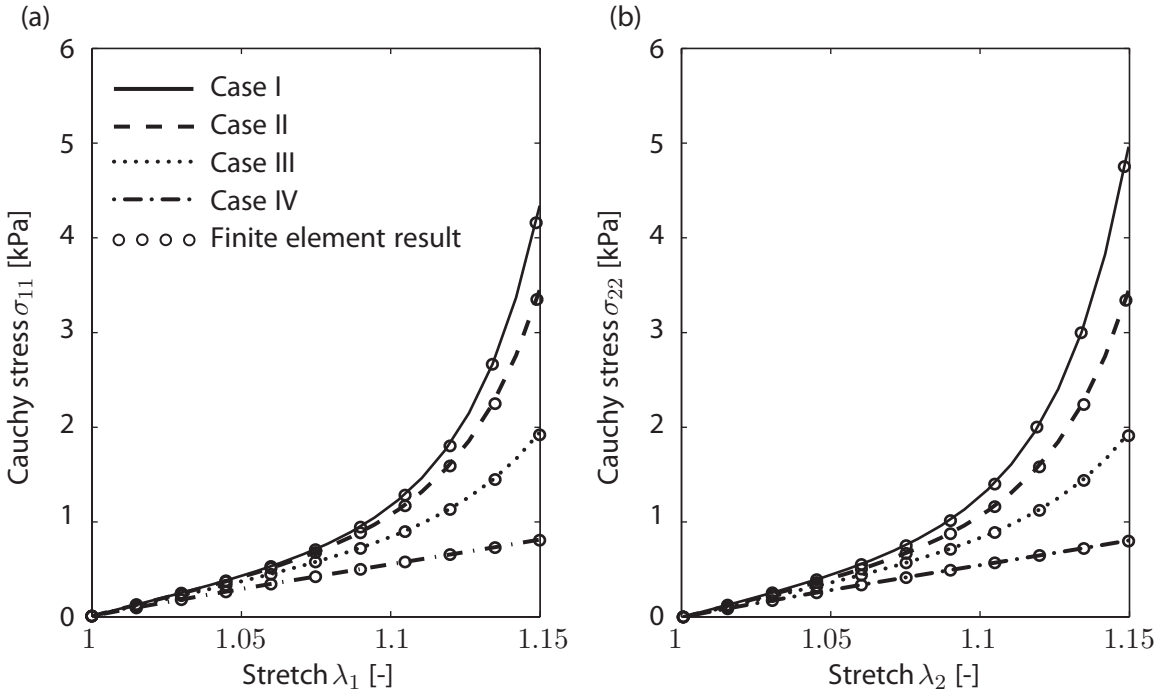

Figure 2.10: Homogeneous biaxial extension of a cube (compare with Figure 2.9): panels (a) and (b) show plots of Cauchy stresses σ_{11}, σ_{22} versus stretches λ_1, λ_2 in the 1 and 2-directions. The four different cases of fiber dispersion are listed in Table 2.5, where (I) is the reference case with parameters given in Table 2.4. The circles represent finite element results while the curves are obtained from a MATLAB computation.

The strips, each with initial length, width and thickness of 10.0, 3.0 and 0.5 mm, respectively, were subjected to a stretch of 1.3. Both ends of each strip were constrained so as to model the mounting in the testing machine and were not allowed to deform. The resulting deformation of each strip was therefore non-homogeneous. We assume uniform material parameters over the adventitial strips with values provided in Table 2.4. Two symmetric fiber families, as shown in Figure 2.7, are assumed to make an angle α of $\pm 47.99^\circ$ with

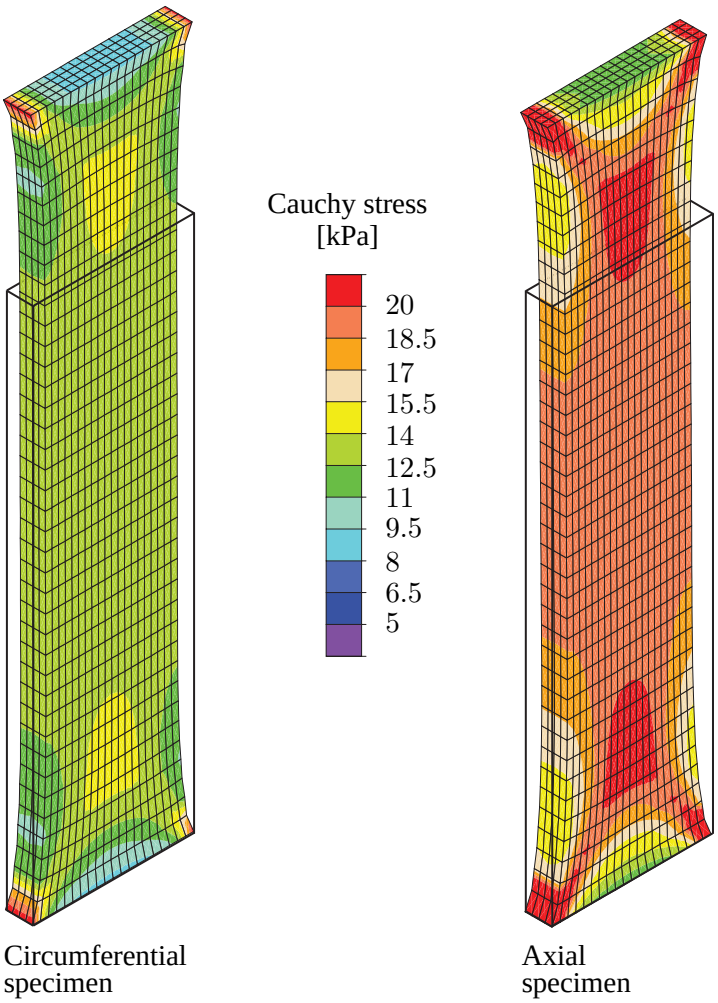

Figure 2.11: Finite element results of circumferential and axial specimens from the adventitia, subjected to a stretch of 1.3. The Cauchy stress is plotted in the direction of the applied displacement. The undeformed (initial) configuration is indicated by solid lines.

the circumferential direction and to show a distribution characterized by $\kappa_{\text{ip}} = 0.116$ and $\kappa_{\text{op}} = 0.493$, as also provided in Table 2.4. We use 3200 hexahedral elements, applying the mixed $Q1/P0$ element throughout the simulation. Figure 2.11 shows the finite element results of the circumferential and axial specimens, subjected to a stretch of 1.3. Both circumferential and axial specimens show that the Cauchy stresses in the adventitia can be modelled within the experimentally predicted range of stresses (compare with the experimental results in Figure 2.8). It turns out that the (axial and circumferential) stresses in the middle of the specimens are slightly higher than the model stresses provided in Figure 2.8, which is due to the boundary conditions used in the present example.

2.5 Discussion

As several previous approaches have shown (see, for example, [134, 157, 168]) incorporation of fiber dispersion into a continuum mechanical framework for soft biological tissues is a challenging and important task. Indeed the mechanical response of such tissues depends significantly on the tissue structure, in particular the arrangement of the fiber dispersion.

One of the main goals of our previous papers, e.g. [39, 134], has been to incorporate the structure of biological tissues into our models in order to capture the physiological and pathological mechanical mechanisms. Recent experimental data have shown the need for a more general model that takes account of the non-symmetric arrangement of collagen fibers. This motivates the introduction, in the present paper, of the bivariate von Mises distribution for describing the collagen fiber dispersion. By fitting the bivariate probability density function to angular distribution data gained from imaging/histological analysis, we can determine structural parameters that can be integrated within the framework of continuum mechanics, in particular hyperelasticity. This allows us to define a strain-energy function from which the stress and the elasticity tensors can be computed, thus facilitating an efficient implementation of the model into a finite element code.

The proposed constitutive model introduces a new structure tensor which incorporates in-plane and out-of-plane fiber dispersions in a clear and simple way, leading to an invariant-based formulation of the strain-energy function, generalizing our previous models [39, 134]. The strain-energy function can incorporate different structure tensors for different fiber families. In particular, the work [19] showed that the number of fiber families depends on the location of the artery and the type of layer, although in most cases two collagen fiber families were reported. For the most general case considered here the structure tensor has three independent components, and these reduce to two when there is in-plane symmetry (with parameters κ_{ip} and κ_{op}) or one when there is rotational symmetry about a single preferred direction (with parameter κ). Various special cases have been highlighted in Section 2.2.2, capturing the cases of rotational symmetry, in-plane dispersion, transverse isotropy and isotropy.

We have constructed a specific energy function that illustrates the efficacy of the model using three specific examples. In the first example we have demonstrated a good fit of the model to experimental data using identified structural parameters as a fixed set. The model was then used to illustrate the effect of fiber dispersion on biaxial extension experiments, including a comparison of analytical and finite element results. Finally, we have analyzed the three-dimensional non-homogeneous stress response for a given overall extension of adventitial strips in the circumferential and axial directions obtained from a human abdominal aorta. The resulting stress responses deviate significantly from each other due to the different mechanical and structural properties in the two directions.

More data are required to determine the detailed dispersion of collagen fibers, not only for the arterial wall but also for other types of fibrous tissues. To inform the modeling process, second-harmonic generation, for example, in combination with optical clearing [177] is a powerful technique for obtaining collagen fiber dispersion data from various types of tissues.

In order to analyze the data within a continuum framework two main approaches are used. First the 'angular integration' (AI) approach, which is computationally expensive because it involves an integration over the unit sphere. It does, however, allow the exclusion of fibers undergoing compression. With the 'generalized structure tensor' (GST) approach, it is possible to extract structural parameters and to include them in the continuum mechanical framework to account for the fiber dispersion. For an artery that exhibits a dispersion with a strong alignment in-plane, the GST seems to be a feasible and very efficient method, although it does require a minor modification in order to exclude fibers which are under compression [150].

For further development, as mentioned above, many more data are needed to inform the modeling process. In particular, there is a pressing need to obtain *in vivo* data in order to construct more realistic models of tissue and organ mechanics. The model can also be extended to incorporate inelastic effects such as damage, viscoelasticity and muscle activation.

3 MICROSTRUCTURE AND MECHANICS OF HEALTHY AND ANEURYSMATIC ABDOMINAL AORTAS: EXPERIMENTAL ANALYSIS AND MODELING

Abstract. Soft biological tissues such as aortic walls can be viewed as fibrous composites assembled by a ground matrix and embedded families of collagen fibers. Changes in the structural components of aortic walls such as the ground matrix and the embedded families of collagen fibers have shown to play a significant role in the pathogenesis of aortic degeneration. Hence, there is a need to develop a deeper understanding of the microstructure and the related mechanics of aortic walls. In this study tissue samples from 17 human abdominal aortas (AA) and from 11 abdominal aortic aneurysms (AAA) are systematically analyzed and compared with respect to their structural and mechanical differences. The collagen microstructure is examined by analyzing data from second-harmonic generation imaging after optical clearing. Samples from the intact AA wall, their individual layers and the AAA wall are mechanically investigated using biaxial stretching tests. A bivariate von Mises distribution was used to represent the continuous fiber dispersion throughout the entire thickness, and to provide two independent dispersion parameters to be used in a recently proposed material model. Remarkable differences were found between healthy and diseased tissues. The out-of-plane dispersion was significantly higher in AAA when compared with AA tissues, and with the exception of one AAA sample, the characteristic wall structure, as visible in healthy AAs with three distinct layers, could not be identified in AAA samples. The collagen fibers in the abluminal layer of AAAs lost their waviness and exhibited rather straight and thick struts of collagen. A novel set of three structural and three material parameters is provided. With the structural parameters fixed the material model was fitted to the mechanical experimental data, giving a very satisfying fit although there are only three material parameters involved. The results highlight the need to incorporate the structural differences into finite element simulations as otherwise simulations of AAA tissues might not be good predictors for the actual *in vivo* stress state.

3.1 Introduction

An abominal aortic aneurysm (AAA) is a local bulging of the abdominal aorta characterized by segmental weakening of the blood vessel. It is often accompanied by the development of an intraluminal thrombus [84, 178]. In general, AAAs are clinically silent and without medical treatment AAAs may grow until rupture [11]. The event of rupture is associated with a significant mortality rate up to 85% [6]. However, the only current treatment of AAA is elective surgical repair, which carries a high mortality risk, especially in older patients, and it does not necessarily improve survival [7]. Therefore a reliable prediction

of rupture risk for individual AAAs is of high relevance in order to assess when the risk of rupture justifies repair [179]. The decision for elective surgical repair is presently based on indicators such as the aneurysm diameter [180], which are more a 'rule-of-thumb' than a scientific criterion, and therefore often unreliable, especially as they do not take into account individual AAA characteristics such as the tissue microstructure.

When seen from a biomechanical point of view, rupture as a material failure occurs when the peak wall stress exceeds the local strength of the arterial wall [181]. As the material properties of the abdominal aorta depend largely on the complex network structure of elastin and collagen, which are the most important structural and primary load bearing proteins in the arterial wall [182], changes in the structural components play a significant role in the pathogenesis of aneurysms. Hence there is a need to develop a deeper understanding of the structure in the abdominal aorta and its ongoing (localized) reorganization during the disease process.

As acquisition of patient-specific three-dimensional (3D) images becomes easier, the utilization of finite element (FE) analysis and biomechanics help to better understand the influence of structural changes on the mechanics. Related numerical models require physiologically determined material and structural parameters. Some mechanical data are available on healthy human abdominal aortas [183, 184]. However, mechanical human tissue data coupled to structural information do not currently exist to be utilized for FE simulations neither for healthy nor for AAA tissues.

Biaxial extension tests on AAAs are documented in, e.g., [110, 112, 113], reporting anisotropic responses with stiffer behavior in the circumferential direction. The studies [107–109] performed uniaxial extension tests until failure also reporting a stiffer circumferential direction. In addition circumferential stiffening was reported in the studies [97, 98, 103], who measured the pressure modulus of AAA tissues. Contrary to these studies isotropy was claimed in [106], who performed uniaxial extension tests. Following this assumption uniaxial tension tests were also performed in, e.g., [53, 57, 185–189], testing only one direction of the specimens (either axial or circumferential).

AAA simulations are often based either on linear material laws and the AAA tissue is often treated as an isotropic elastic material [190–193] or, if anisotropic material laws are utilized, simulations are based on structural data obtained from healthy tissues [108]. However, studies such as [13] have shown that a more advanced constitutive description of AAA tissues is critical for a proper prediction of AAA wall stresses. Additionally, we have identified substantial differences in the structure between healthy aortic tissues and tissues taken from AAAs. Especially the out-of-plane collagen dispersion in AAAs differs significantly in comparison with healthy tissue. Figure 3.1 shows representative second-harmonic generation (SHG) images of the collagen structure in a healthy abdominal aortic media and a AAA tissue taken from the middle portion of the wall thickness. The corresponding histograms of the angular dispersion of fiber angles clearly show a higher

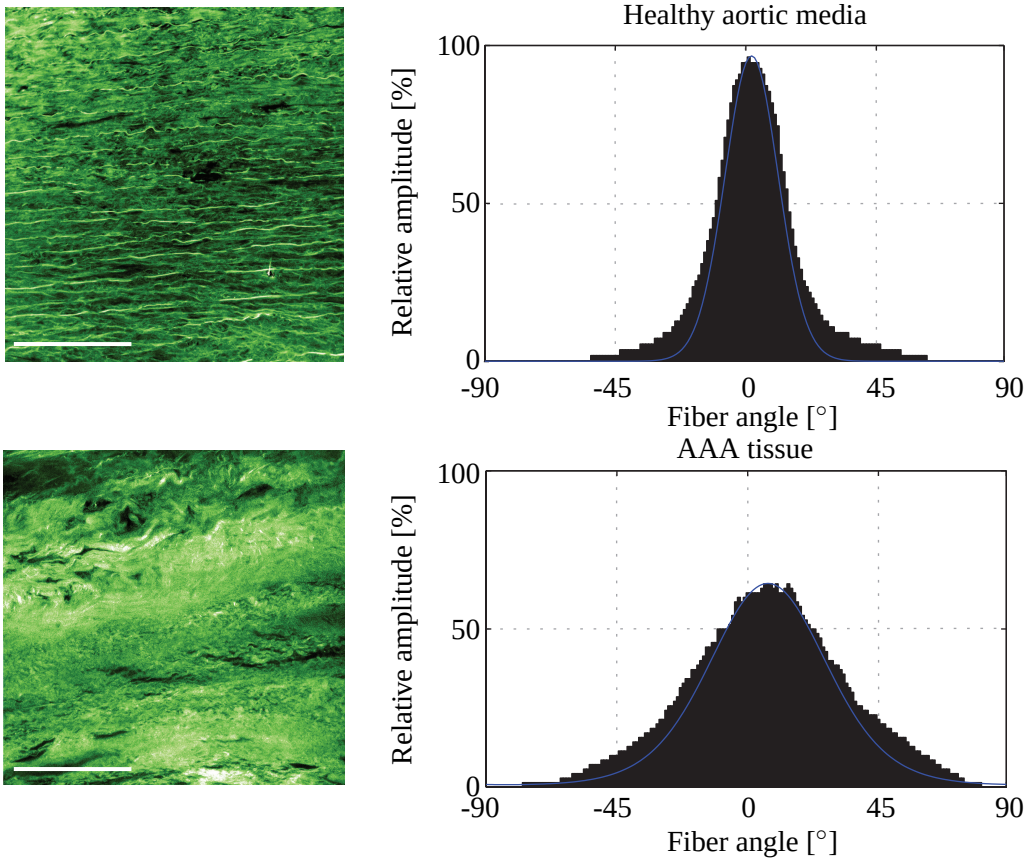

Figure 3.1: Representative SHG images of the collagen structure in a healthy abdominal aortic media (above) and a AAA tissue taken from the middle portion of the wall thickness (below). Corresponding graphs show the angular dispersion (relative amplitude in %) of collagen fiber orientations, which is narrower for a healthy aortic media (smaller dispersion of fibers), when compared with AAA tissue (higher fiber dispersion). Scale bar is 100μm.

out-of-plane dispersion for the AAA tissue. This finding highlights the need for the incorporation of the AAA structure into related FE simulations as otherwise the numerical results may not be a good prediction of the *in vivo* state.

Although the pathogenesis and material properties of AAAs have been topics of several studies more recently [110, 112, 116, 194–196], the specific events leading to AAA development still remain unclear. To the authors' knowledge, no biaxial mechanical data combined with the corresponding microstructure of both healthy (layer-specific) and aneurysmatic aortic tissues are yet available. To further increase the understanding and to improve rupture risk prediction it is necessary to study effects of localized wall changes (shown, e.g., for cerebral aneurysms in [197]) by combining the microstructure with patient-specific mechanical data and systematically compare these changes with healthy abdominal aortic tissues. Such a knowledge can then be used to improve numerical models incorporating

structure-based nonlinear material models, as was recently performed in [198] where the biaxial response of porcine aortic tissues was combined with the related microstructure identified using histological slices.

The aim of the present study is to systematically analyze and compare the material properties of layer-specific healthy abdominal aortic tissue with tissue taken from AAA wall samples, by means of biaxial stretching tests and their link with the 3D microstructure using a combination of optical clearing, SHG imaging and subsequent automated quantification of the 3D fiber dispersion and alignment. First the utilized materials and methods are explained, involving tissue clearing and SHG imaging, biaxial stretching tests, a recently published material model used to capture the non-symmetric collagen fiber dispersion in arterial walls and the related mechanics, data fitting and the statistical analysis. Subsequently the results are presented, first the structural data and then the biaxial mechanical data. Differences between structural and material parameters are compared utilizing statistical tools, and correlations between these parameters are investigated. Finally the results are discussed and put into context with the current literature.

3.2 Materials and Methods

Seventeen human abdominal aortas (AA) with non-atherosclerotic intimal thickening, from 7 women and 10 men (63 ± 11 (SD) yr, range 45-84), were collected as intact tubes within 24 h of death and stored in 0.9% physiological saline solution at 4°C until testing. Additionally, eleven wall samples from (true) abdominal aortic aneurysms (AAA) (69 ± 8 (SD) yr; range 53-76; 1 woman, 10 men) were collected from open aneurysm repair at the anterior side at the Department of Vascular Surgery, Medical University Graz, Austria, and stored in Dulbecco's Modified Eagle's Medium (DMEM) at 4°C until testing. The AAA samples were mostly small pieces with the longitudinal direction marked by a surgical clip or suture. Both the use of autopsy and AAA materials from human subjects were approved by the Ethics Committee of the Medical University of Graz (27-250 ex 14/15).

3.2.1 AA and AAA Microstructure

Sample Preparation

Intact aortic tubes were cut open along the longitudinal direction and small samples, approximately 15×5 mm in size, were acquired from both the healthy and the aneurysmatic specimens, with the longer side marking the longitudinal direction. Subsequently, the samples were cleared using a protocol according to [177]. First the specimen were dehydrated by submerging them into a graded ethanol series, consisting of 50, 70, 95 and twice 100% concentrated ethanol solutions. Subsequently the specimen were stored at 100% benzyl

alcohol – benzyl benzoate (BABB) for at least 12 h after initially submerging them into a 1 : 2 solution of ethanol:BABB for 4 h. All steps were performed at room temperature. Whenever the thrombus, covering the corresponding aneurysmatic wall, was available a small piece was fixed in 4% neutral-buffered formalin (pH 7.4), embedded in paraffin and prepared for histological investigations to determine the thrombus age according to [112].

Second-Harmonic Generation Imaging

To identify the 3D collagen structure of the samples SHG imaging was performed at the Institute of Science and Technology in Klosterneuburg, Austria. An imaging set-up consisting of a 'Chameleon' Titan Saphir laser (Coherent, Inc., USA) integrated into a TriM Scope II confocal microscope (LaVision BioTec GmbH, Germany) was used. The excitation wavelength was tuned to 880 nm and the detection of the backscattered signal was achieved using a gallium arsenide-phosphide detector and a BP 460/50 emission filter. Images (z-stacks, 3 μm steps, and cross-section images in (x,z)-plane) were acquired using a Leica IMM CORR CS2 20× water immersion objective with a working distance of 0.68 mm.

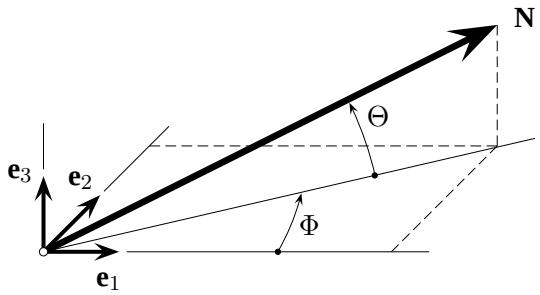

Figure 3.2: Unit vector **N** representing a general fiber direction defined by the two angles Φ and Θ with respect to rectangular Cartesian unit basis vectors $\mathbf{e}_1$, $\mathbf{e}_2$, $\mathbf{e}_3$ [199].

Microstructural Analysis of Collagen fiber Orientation

Morphological collagen data were extracted from 3D images (z-stack) by combining Fourier power spectrum analysis and wedge filtering, as described in [139, 177]. The analysis yielded discrete angular distributions of relative amplitudes which resembled the fiber orientations. To describe a general fiber direction a coordinate system characterized by the unit rectangular Cartesian basis vectors $\mathbf{e}_1$, $\mathbf{e}_2$, $\mathbf{e}_3$, as shown in Fig. 3.2, was used [199], with the unit vector **N** representing a general fiber direction in the (unloaded) reference configuration, defined by the two angles $\Phi \in [0, 2\pi]$ and $\Theta \in [-\pi/2, \pi/2]$. For a circular

cylinder $\mathbf{e}_1$ is taken to be the circumferential direction and $\mathbf{e}_3$ the radial direction, therefore we refer to the angles Φ and Θ as the in-plane and out-of-plane angle, respectively.

The in-plane and out-of-plane collagen fiber orientations were fitted using a bivariate von Mises distribution $\rho(\Theta,\Phi) = \rho_{\text{ip}}(\Phi)\rho_{\text{op}}(\Theta)$ for the probability density ρ of $\mathbf{N}$ (in-plane and out-of-plane dispersions are essentially independent [19]), with the particular choice [199]

$$\rho_{\text{ip}}(\Phi) = \frac{\exp[a\cos 2(\Phi \pm \alpha)]}{I_0(a)}, \qquad \rho_{\text{op}}(\Theta) = 2\sqrt{\frac{2b}{\pi}}\frac{\exp[b(\cos 2\Theta - 1)]}{\text{erf}(\sqrt{2b})}, \tag{3.1}$$

where $\rho_{\text{ip}}(\Phi) = \rho_{\text{ip}}(\Phi + \pi)$ and $\rho_{\text{op}}(\Theta) = \rho_{\text{op}}(-\Theta)$ describe the in-plane and out-of-plane dispersions, respectively. In (3.1) a and b are (constant) concentration parameters, i.e. fitting parameters, which define the shape of the von Mises distributions, $I_0(a)$ is the modified Bessel function of the first kind of order 0 and α is the angle between the mean fiber direction and the circumferential direction $\mathbf{e}_1$.

According to [199] we introduce the two scalar quantities κ_{ip} and κ_{op} which measure the in-plane and out-of-plane dispersion, respectively (they are used in the strain-energy function introduced in Section 3.2.3). Thus,

$$\kappa_{\text{ip}} = \frac{1}{2} - \frac{I_1(a)}{2I_0(a)}, \qquad \kappa_{\text{op}} = \frac{1}{2} - \frac{1}{8b} + \frac{1}{4}\sqrt{\frac{2}{\pi b}}\frac{\exp(-2b)}{\text{erf}(\sqrt{2b})}, \tag{3.2}$$

where $0 \leq \kappa_{\text{ip}} \leq 1$ and $0 \leq \kappa_{\text{op}} \leq 1/2$. If both concentration parameters a and b become infinite, then the collagen fibers are perfectly aligned.

Layer-specific thicknesses were measured from out-of-plane images using FIJI (`http://fiji.sc/Fiji`, Ashburn, VA) [200]. They were used for the calculation of the dispersion parameters κ_{ip} and κ_{op} and the angle α of the intact AA wall. For example, the parameter κ_{ip} for the AA wall was calculated as the sum of the layer-specific κ_{ip} where the individual κ_{ip} was weighted with respect to the layer-specific thickness.

3.2.2 AA and AAA Mechanics

Sample Preparation

In regard to AA tissue, adjacent to the small samples which were prepared for SHG imaging, two squared samples with the dimension 20×20 mm were cut out to obtain one 'composite' patch (intact wall) and one medial patch (after the intimal and adventitial layers were peeled off), used for mechanical testing. In addition, a cruciform sample with the dimension 35×35 mm adjacent to the other two samples was cut out with a punching tool so that a central region of the sample with the dimension 5×5 mm remained, see Fig. 3.3

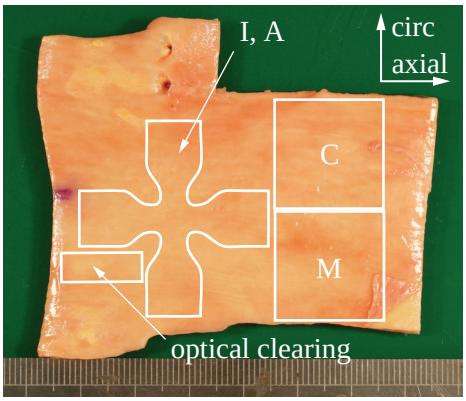

Figure 3.3: AA tissue showing contours of the samples, which were prepared from the specimen (I ... intima, M ... media, A ... adventitia, C ... composite).

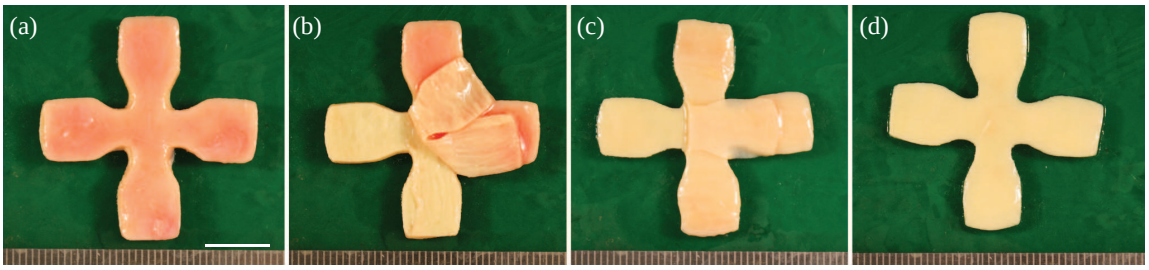

Figure 3.4: Steps of preparing AA tissue for layer-specific biaxial testing: (a) cruciform sample of the intact wall; (b) separation of the adventitia (there are still some medial patches visible on the adventitia which were peeled off later); (c) separation of the thin intimal layer; (d) medial layer left after the layer separation process. Scale bar is 10 mm.

(the cruciform shape was designed using the FE method to minimize the inhomogeneity of the stress state in the central region [201]). Subsequently, intimal and adventitial patches required for testing were manually separated from the media. The layers were clearly distinguishable and minor fractions of the media could mostly be removed from the intima and the adventitia, see Fig. 3.4.

For the adventitia and the intima cruciform samples had to be used because the sample thickness was very thin (< 0.4 mm). Instead of piercing the hooks directly into the samples the hooks were placed in sandpaper which was then glued to the arms of the samples. Especially by piercing the hooks directly into the intima we have frequently observed rupture even before mounting the sample into the testing machine. Intima and adventitia were thin enough to exhibit a homogeneous stress state in the central region of the cruciform sample. Intact wall and media sample were too thick (> 0.7 mm) to be tested with the cruciform sample geometry, and hence were tested using the well-established squared geometry.

Similar to the healthy squared wall samples, a patch with dimension 20×20 mm was cut out from the AAA wall (sometimes two patches could be obtained). A clear identification of separable layers was impossible in most AAA samples, hence only the intact AAA wall was tested. The mean thickness of both AA and AAA samples was measured according to [202]. Subsequently, black tissue markers were applied by spraying on the surface of each sample generating a scattered pattern suitable for optical tracking.

Biaxial Tensile Tests

All samples were mounted in a biaxial testing device via hooked surgical sutures. The samples were submerged into a bath filled with 0.9% physiological saline solution and heated up to $37 \pm 0.1^{\circ}$C. During testing normal and shear deformations were quantified according to [203], and it was found that negligible shear stresses were present throughout the testing.

A stretch-driven protocol was used for testing, and executed with a stepwise increase of 0.025 stretch until rupture, starting with 2.5% deformation. Each sample was tested using the following protocol for each stretch increment: $\lambda_{\text{axial}} : \lambda_{\text{circ}} = 1:1,\ 1:0.75,\ 0.75:1,\ 1:0.5$ and $0.5:1$, where λ_{axial} denotes the stretch in the axial direction while λ_{circ} is the stretch in the circumferential direction. After each increase in stretch four preconditioning cycles were conducted and the fifth was then used for data recording and analysis. Throughout the test the samples were loaded quasi-statically at a rate of 3 mm/min. It is worth noting that the used biaxial testing protocol covers a large range of deformations including the *in vivo* situation, and hence provides data for a unique set of material parameters. As the results, especially for the adventitial samples, were very sensitive to initial preloads, zero strain was defined at a tissue configuration under 0.005 N load.

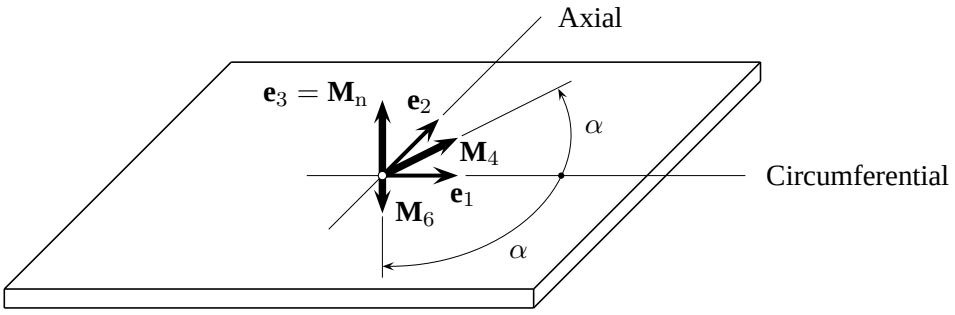

Figure 3.5: Sample with two symmetric fiber families with mean fiber directions $\mathbf{M}_4$ and $\mathbf{M}_6$, each making an angle α with the circumferential direction $\mathbf{e}_1$. The normal direction to the plane is $\mathbf{M}_{\text{n}}$ [199].

3.2.3 Material Model

We introduce the deformation gradient $\mathbf{F}$, the right Cauchy–Green tensor $\mathbf{C} = \mathbf{F}^{\mathrm{T}}\mathbf{F}$ [173], and two symmetric fiber families with the (in-plane) mean fiber directions, i.e.

$$\mathbf{M}_4 = \cos\alpha\mathbf{e}_1 + \sin\alpha\mathbf{e}_2, \qquad \mathbf{M}_6 = \cos\alpha\mathbf{e}_1 - \sin\alpha\mathbf{e}_2, \tag{3.3}$$

where the mean fiber directions $\mathbf{M}_4$ and $\mathbf{M}_6$ make an angle α with the circumferential direction $\mathbf{e}_1$. In addition, we introduce the invariants I_1, I_4, I_6 and I_{n} according to

$$I_1 = \mathrm{tr}\mathbf{C}, \qquad I_i = \mathbf{C} : \mathbf{M}_i \otimes \mathbf{M}_i, \quad i = 4,6, \qquad I_{\mathrm{n}} = \mathbf{C} : \mathbf{M}_{\mathrm{n}} \otimes \mathbf{M}_{\mathrm{n}}, \tag{3.4}$$

where $\mathbf{M}_{\mathrm{n}}$ is a unit out-of-plane vector, see Fig. 3.5.

To mathematically quantify the fiber dispersion we use the generalized structure tensors $\mathbf{H}_4$ and $\mathbf{H}_6$ which describe the material behavior [199], i.e.

$$\mathbf{H}_i = A\mathbf{I} + B\mathbf{M}_i \otimes \mathbf{M}_i + (1 - 3A - B)\mathbf{M}_{\mathrm{n}} \otimes \mathbf{M}_{\mathrm{n}}, \qquad i = 4,6, \tag{3.5}$$

where the constants A and B are

$$A = 2\kappa_{\mathrm{op}}\kappa_{\mathrm{ip}}, \qquad B = 2\kappa_{\mathrm{op}}(1 - 2\kappa_{\mathrm{ip}}). \tag{3.6}$$

Assuming that the aorta can be modeled as a purely elastic, incompressible and fiber-reinforced material, the structure tensors $\mathbf{H}_i$ are incorporated into the decoupled strain-energy function Ψ according to

$$\Psi = \Psi_{\mathrm{g}}(\mathbf{C}) + \sum_{i=4,6} \Psi_{\mathrm{f}i}(\mathbf{C}, \mathbf{H}_i) + p\mathbf{I}, \tag{3.7}$$

where p represents the Lagrange multiplier which enforces incompressibility and $\mathbf{I}$ is the second-order unit tensor. The strain-energy function Ψ_{g} represents the ground matrix, i.e.

$$\Psi_{\mathrm{g}}(\mathbf{C}) = \frac{c}{2}(I_1 - 3), \tag{3.8}$$

where c is a parameter, and $\Psi_{\mathrm{f}i}$ represents the contribution of the two fiber families, i.e.

$$\Psi_{\mathrm{f}i}(\mathbf{C}, \mathbf{H}_i) = \frac{k_1}{2k_2}\left\{\exp\left[k_2(I_i^\star - 1)^2\right] - 1\right\}, \qquad i = 4,6, \tag{3.9}$$

with the stress-like parameter $k_1 > 0$, the dimensionless parameter $k_2 > 0$ and the generalized invariants $I_i^\star$ according to

$$I_i^\star = \mathrm{tr}(\mathbf{H}_i\mathbf{C}) = AI_1 + BI_i + (1 - 3A - B)I_{\mathrm{n}}, \qquad i = 4,6, \tag{3.10}$$

which includes the mean fiber directions $\mathbf{M}_i$ in form of the invariants I_i and the two dispersion parameters κ_{ip} and κ_{op}, as introduced in Section 3.2.1, in form of the constants A and B.

The material model utilizes three structural parameters (κ_{ip}, κ_{op}, α) which can be determined by structural analysis (in the present study using SHG images) and three material parameters (c, k_1, k_2), which are determined by fitting the model to the mechanical data (in the present study to the data obtained from biaxial stretching tests).

3.2.4 Data Fitting and Statistical Analysis

After the structural parameters have been determined as described above, fitting of the material model to the biaxial experimental data was performed. Data from all five testing protocols ($1:1$, $1:0.75$, $0.75:1$, $1:0.5$, $0.5:1$) in both axial and circumferential directions were fitted simultaneously, utilizing the optimization toolbox 'lsqnonlin' in MATLAB (2012b, The MathWorks, Inc., Massachusetts, United States). As the structural parameters κ_{ip}, κ_{op} and α were known from structural analysis, and hence kept constant throughout the fitting procedure, the only three fitting parameter were c, k_1 and k_2. To evaluate the 'goodness of fit' the coefficient of determination R^2 was used.

Our study resulted in 3D distributions of amplitudes in 1° resolution, representing the in-plane and out-of-plane collagen dispersions in AAs and AAAs in combination with the corresponding mechanical data obtained from biaxial stretching tests, and yielded structural and material parameters for incorporation in a recently proposed micro-structurally motivated material model [199].

Values for the material parameters are reported as the medians and interquartile ranges (middle fifties), as we cannot assume a normal distribution due to the small sample cohort and outliers can affect the mean and standard deviation severely. Linear regression analysis was carried out to test possible correlations between the material and the structural parameters as well as patient data, utilizing Pearson's correlation coefficient. Significant correlations between the median values of the material and structural properties were tested by utilizing the Mann-Whitney U-test. Differences were considered statistically significant if the p value was less than 0.05, corresponding to a 95% confidence. All statistical analysis was performed using MATLAB (2012b, The MathWorks, Inc., Massachusetts, United States).

Table 3.1: Patient information of all tested AAA specimens: age, gender (F = female; M = male), maximum diameter D, smoker, pack years, hypertension, aneurysm ruptured, thrombus, clinical signs of inflammation (inflam), diabetes, and relative thrombus age (all in phase III according to [112]; a lower number refers to a younger thrombus).

Patient #	Age [yr]	Gender	D [mm]	Smoker y/n	Pack years	Hypertension y/n	Ruptured y/n	Thrombus y/n	Inflam y/n	Diabetes y/n	Thrombus age
AAA-1	75	M	58	y	50	n	n	y	n	y	335
AAA-2	74	M	85	y	50	y	y	y	n	n	370
AAA-3	74	M	63	y	40	y	n	y	n	y	N/A
AAA-4	55	M	85	y	40	y	n	y	y	n	320
AAA-5	74	M	66	y	20	y	n	y	y	y	350
AAA-6	53	M	53	y	50	y	n	y	n	y	380
AAA-7	72	F	55	y	20	y	n	n	n	n	320
AAA-8	76	M	70	y	25	y	n	y	n	y	N/A
AAA-9	74	M	74	y	105	y	n	y	n	n	N/A
AAA-10	61	M	130	y	90	y	y	y	n	y	N/A
AAA-11	72	M	65	y	30	n	n	y	n	y	340

3.3 Results

3.3.1 Study Population

All 17 AA samples could be analyzed for structural data. In total, mechanical testing succeeded for 4 intimal, 9 medial, 9 adventitial samples and 7 samples for the intact AA wall. Additionally, all eleven samples of AAA walls could be analyzed structurally and, except for one, succeeded in being tested biaxially. With the exception of one sample, all wall samples were covered by a thrombus which was analyzed to obtain its relative age. According to [112], all thrombi were in phase III (intermediate), in which the erythrocytes are disrupted and proteins are washed out of the fibrin network. The relative age is here defined by a number in between 300 and 400 where these two numbers indicate the bounds to phase II and phase IV, respectively; hence a number closer to 300 corresponds to a relatively younger thrombus within phase III than a number closer to 400.

With the exception of one AAA sample, all aneurysms exhibited a maximum diameter of $\geq$55 mm, which is a size where intervention in men is typically advocated (or 50 mm in women, or if the maximal diameter increases more than 5–10 mm in one year), see [85, 180, 204]; the average aneurysm diameter was 73 ± 20 mm, range 53–130 mm. Two samples (AAA-2, AAA-10) were collected from a ruptured aneurysm. The sizes of AAA-1 and AAA-4 were big enough to prepare two samples for the biaxial stretching tests. Hence, subsequently they are labeled as AAA-1.1, AAA-1.2, AAA-4.1 and AAA-4.2. For a summary of the patient information of all tested AAA samples see Table 3.1.

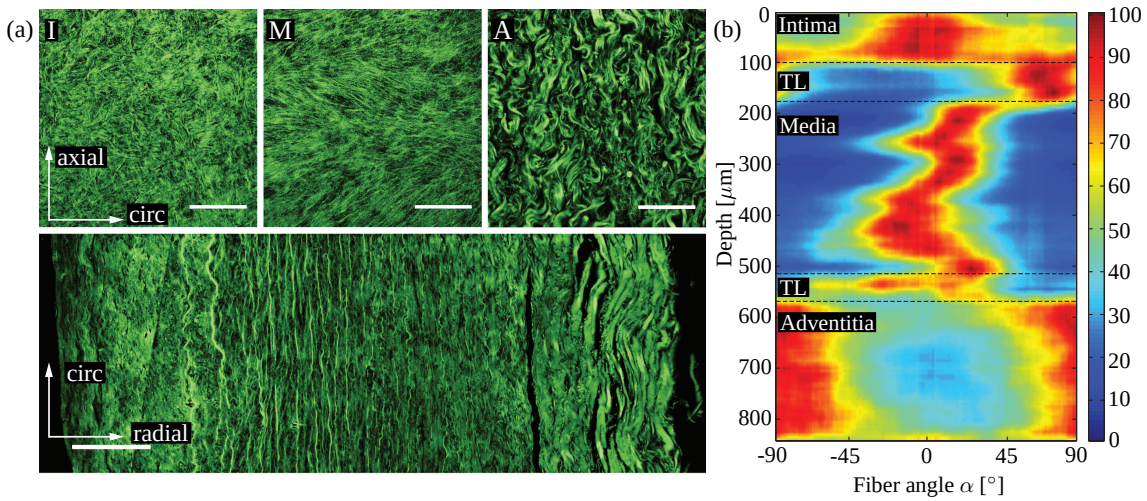

Figure 3.6: Layered structure of a representative healthy abdominal aorta: (a) three SHG images on the top showing in-plane sections of the intima (I), media (M) and adventitia (A), while on the bottom an image through-the-thickness is displayed, scale bar is 100 μm; (b) intensity plot showing collagen fiber orientation and dispersion through the depth of the aortic wall starting with the intima, followed by a transition layer (TL) around the location of the membrana elastica interna, then the media, followed by another transition layer around the location of the membrana elastica externa and finally the adventitia – dark red depicts no dispersion and blue relates to no fibers.

3.3.2 Structural Data

Abdominal Aorta (AA)

Figure 3.6(a) shows SHG images of a representative sample; the three images on the top display in-plane sections of the intima (I), media (M) and adventitia (A), while on the bottom an image through-the-thickness is displayed. Consistent with [19] the healthy abdominal aorta consists of three distinguishable layers with a 'carpet-like' structure in (I) and two families of fibers in (M), more oriented towards the circumferential direction, while (A) shows wavy and thicker fiber bundles more oriented towards the axial direction. The image through-the-thickness displays the intima on the left, then a transition layer and the highly oriented media, and then, after another transition layer, the wavy collagen of the adventitia.

The intensity plot of Fig. 3.6(b) depicts the collagen fiber orientation and dispersion through the aortic wall. A fiber angle of 0° denotes the circumferential direction, whereas 90° denotes the axial direction. Dark red depicts no dispersion, whereas blue shows no fibers. The images were taken starting from the intimal side. Hence the intima can be seen in the first 100 μm in the intensity plot, showing a rather strong dispersion around the circumferential direction. That is followed by a transition layer (TL) observed as a (rapid)

Table 3.2: Structural parameters (κ_{ip}, κ_{op}, α) for the intima, media, adventitia and the intact wall of the abdominal aortas determined from SHG images; n indicates the number of samples.

	Intima		Media		Adventitia		Intact Wall	
	Median	$[Q1;Q3]$	Median	$[Q1;Q3]$	Median	$[Q1;Q3]$	Median	$[Q1;Q3]$
κ_{ip}	0.261 ($n=7$)	[0.214;0.283]	0.208 ($n=17$)	[0.165;0.255]	0.232 ($n=16$)	[0.192;0.282]	0.237 ($n=7$)	[0.212;0.287]
κ_{op}	0.484 ($n=17$)	[0.468; 0.488]	0.487 ($n=17$)	[0.481; 0.489]	0.466 ($n=17$)	[0.459;0.479]	0.479 ($n=17$)	[0.473;0.482]
α	3.25° ($n=7$)	[1.09;6.13]	6.91° ($n=17$)	[5.269;9.715]	77.53° ($n=16$)	[67.04;84.02]	24.46° ($n=7$)	[22.45;30.18]

orientation change of collagen fibers towards the axial direction around the location of the membrana elastica interna, which then changes back to the circumferential direction in the media. The images show two counter-rotating fiber families around the circumferential direction. Subsequently another transition layer around the location of the membrana elastica externa is reached, displaying a rather smooth transition of thinner medial collagen to thicker wavy collagen fiber bundles in the adventitia, appearing in two fiber families and being oriented more towards the axial direction.

Although the tissues were not loaded the fibers displayed a highly organized structure both in the tangential plane of the aorta and through the thickness of the wall, which enabled the determination of structural data, i.e. the dispersion parameters κ_{ip} and κ_{op}, and the angle α between the mean fiber direction and the circumferential direction which were averaged over the thickness of the separate layers. The structural parameters for the individual layers and for the intact wall are summarized in Table 3.2.

The out-of-plane dispersion κ_{op} was rather low in all three healthy layers. Especially for the intima and media the fibers were highly aligned, with a median for κ_{op} close to 0.5 (0.484 ± 0.019 and 0.487 ± 0.008, respectively). The wavy structure of the collagen fibers in the adventitia in the unloaded configuration resulted in a slightly higher out-of-plane dispersion, i.e. $\kappa_{op} = 0.466 \pm 0.020$. The fiber families in the media were aligned closer to the circumferential direction than reported in [19], with a median angle of $\alpha = 6.91^\circ \pm 4.4^\circ$, while the fiber families in the adventitia were aligned closer to the axial direction with $\alpha = 77.53^\circ \pm 17.0^\circ$. For a summary of the dispersion parameters κ_{ip}, κ_{op} and the angle α in form of box-and-whisker plots see Fig. 3.7(a)-(c), while Fig. 3.7(d) shows the thicknesses of the intact AA wall and each individual layer, with a mean ratio 20 : 49 : 31 for Intima:Media:Adventitia, which is consistent with [19].

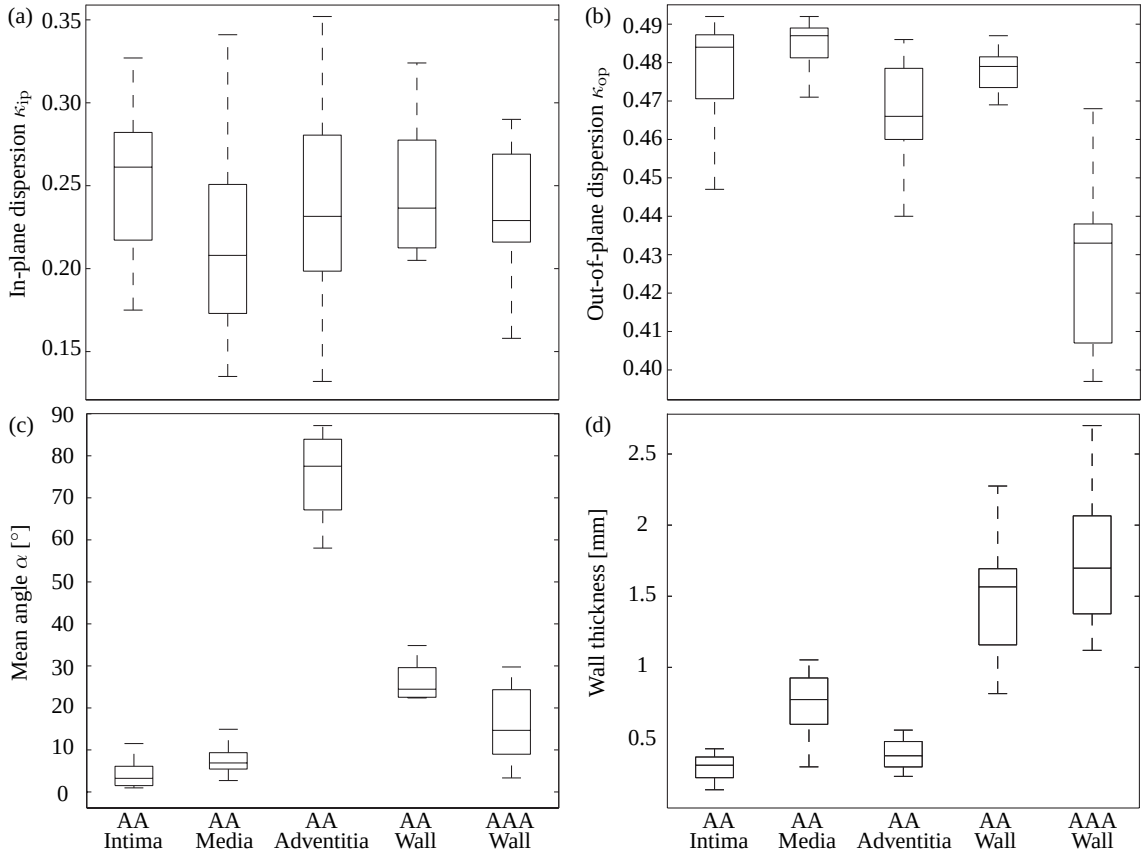

Figure 3.7: Box-and-whisker plots of the structural parameters and the wall thickness for the abdominal aorta (AA), the individual layers, and for the AAA wall: (a) in-plane dispersion parameter κ_{ip}; (b) out-of-plane dispersion parameter κ_{op}; (c) mean fiber angle α; (d) wall thickness. AAA wall data refer to Section 3.3.2.

Abdominal Aortic Aneurysm (AAA)

Within the AAA wall specific layers could not be identified, except for sample AAA-6, and the characteristic wall structure, as visible in healthy abdominal aortic wall with three distinct layers, was not present. Even in samples without atherosclerotic alterations the structure was remarkably different from those obtained from AAs. By comparing the tissue samples with each other a substantial variability in fiber architecture, fiber diameter and waviness could be identified, even within the same AAA sample. In general, most samples showed a degenerated luminal layer with calcification and sometimes small fat cells, and thin straight struts of collagen oriented more towards the circumferential direction. Towards the abluminal side these struts thickened, but were still oriented more towards the circumferential direction. In addition, cystic medial degeneration could be seen, including larger adipocytes. For the structural analysis only those images were considered which

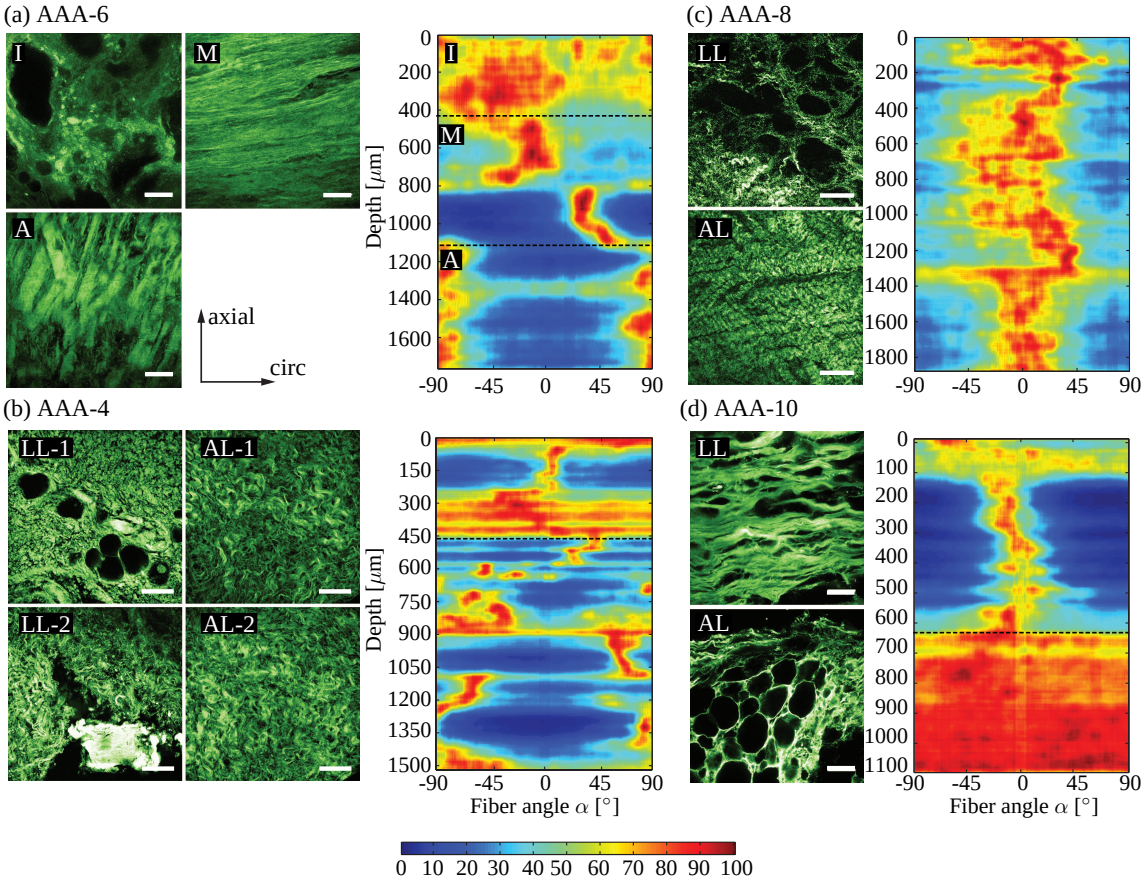

Figure 3.8: SHG images and intensity plots for AAA samples: (a) layered structure of sample AAA-6 (I: intima, M: media, A: adventitia) which was the only AAA sample to exhibit a layer-specific character. The intensity plot shows three distinct layers – a rather calcified intima, two fiber families in media and adventitia; (b) structure of luminal layer (LL) and abluminal layer (AL) of two patches taken from adjacent locations (-1, -2) of sample AAA-4 displaying differences. The lower left image (LL-2) shows wavy collagen fibers and calcification. The first 450 μm in the intensity plot shows a highly disturbed structure followed by an adventitia-like structure with two alternating fiber families; (c) collagen structure of sample AAA-8 in (LL) and (AL). The intensity plot shows collagen preferably oriented towards the circumferential direction throughout the wall; (d) ruptured sample AAA-10 containing a (LL) with a highly oriented collagen structure and a significant number of adipocytes towards the (AL) side. The intensity plot shows a collagen structure highly oriented towards the circumferential direction followed by a rather isotropic (AL). All intensity plots start at the top with the (LL). Scale bar is 100 μm.

Table 3.3: Structural parameters (κ_{ip}, κ_{op}, α) for the AAA wall determined from SHG images.

Patient #	κ_{ip}	κ_{op}	α
AAA-1	0.290	0.397	26.00
AAA-2	0.229	0.438	3.33
AAA-3	0.276	0.398	13.97
AAA-4	0.223	0.413	24.33
AAA-5	0.261	0.438	9.05
AAA-6	0.202	0.468	9.22
AAA-7	0.216	0.428	29.74
AAA-8	0.265	0.407	8.98
AAA-9	0.207	0.464	18.41
AAA-10	0.158	0.461	7.87
AAA-11	0.269	0.438	15.37
Median	0.229	0.438	13.97
$[Q1;Q3]$	$[0.209;0.268]$	$[0.409;0.455]$	$[9.998;22.85]$

did *not* show calcification or adipocytes, as otherwise the averaged dispersion parameter values would have been distorted.

Sample AAA-6 exhibited a strikingly healthy architecture, had the smallest diameter (53 mm) and was covered by the oldest thrombus of all samples. It showed a rather isotropic intimal side, two fiber families oriented more towards the circumferential direction in the media and an adventitia-like structure with highly aligned fibers oriented more towards the axial direction, see Fig. 3.8(a). In-plane images of the intima also showed small fat cells and calcification at the luminal side (not considered for structural analysis), explaining the rather isotropic structure seen in the intensity plot at the top until a depth of about $400\,\mu$m, see Fig. 3.8(a), while the media showed straight collagen fibers resulting in high and narrow intensities in the intensity plot (depth between 400 and $1100\,\mu$m). Remarkably, the collagen fibers in the abluminal layers of AAAs lost their waviness and exhibited rather straight and thick struts of collagen. Samples AAA-1, AAA-3, AAA-5, AAA-7, and AAA-11 exhibited a similar collagen structure throughout the thickness as seen in the adventitia of sample AAA-6, and having lost the layered structure. Samples AAA-1 and AAA-7 showed alternating fiber families with a mean fiber angle $\alpha = \pm 26^\circ$ and $\alpha = \pm 29.74^\circ$, respectively, whereas the other samples were oriented closer to the circumferential direction, also exhibiting alternating fiber families.

The two patches taken from adjacent locations of sample AAA-4 showed an intact abluminal layer (AL) similar to a healthy adventitia layer, see Fig. 3.8(b). However, no media was visible as the wavy collagen fibers were infiltrated with plaque and adipocytes. The upper left image (LL-1) in Fig. 3.8(b) (where (LL) stands for luminal layer) shows bright 'stains' representing a rather degenerated collagen structure. The lower left image (LL-2) shows

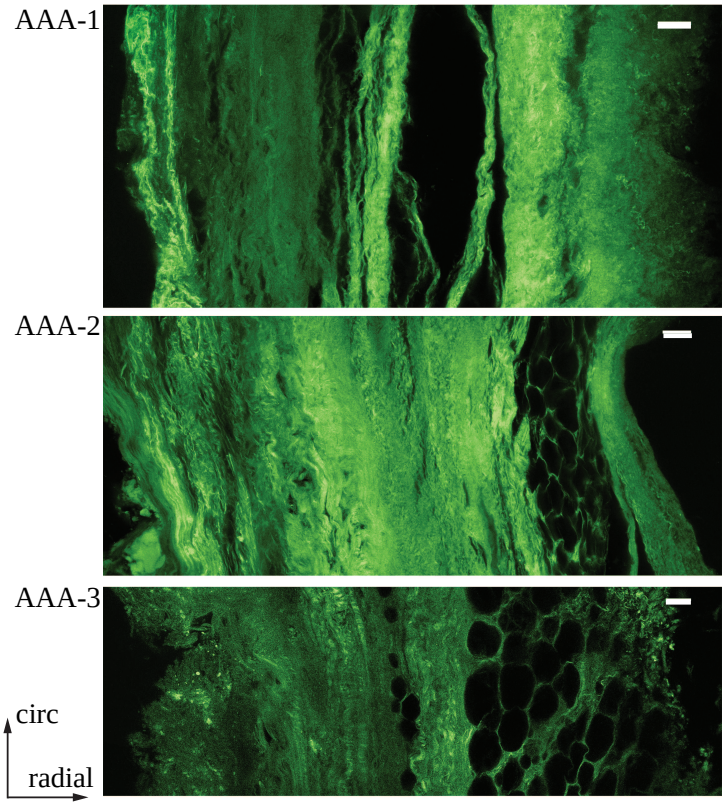

Figure 3.9: Collagen structure in the circumferential/radial plane of samples AAA-1, AAA-2 and AAA-3 indicating high dispersion of collagen fibers. Luminal side: left; abluminal side: right. Scale bar is 100 μm.

an adjacent region in the same luminal layer, exhibiting a different structure with wavy collagen fibers and calcification. The first 450 μm in the intensity plot shows a disturbed structure merging into two alternating fiber families.

The (AL) of sample AAA-8 showed thickened collagen struts still wavy but oriented more towards the circumferential direction, see Fig. 3.8 (c). Towards the (LL) the fibers became thinner and looked more like in a healthy adventitia, merging into a disturbed collagen structure. The intensity plot shows fibers preferably oriented towards the circumferential direction throughout the wall, ending with some more anisotropic structure, resembling the degeneration at the luminal side. Both ruptured samples (AAA-2 and AAA-10) showed a significant amount of cystic medial degeneration, infiltrated with adiposytes in the (AL), preceded by a highly organized collagen structure in the (LL) oriented more towards the circumferential direction, see Fig. 3.8 (d). The (AL) is rather isotropic as can be seen from the intensity plot. Sample AAA-9 showed a similar structure to the two ruptured samples.

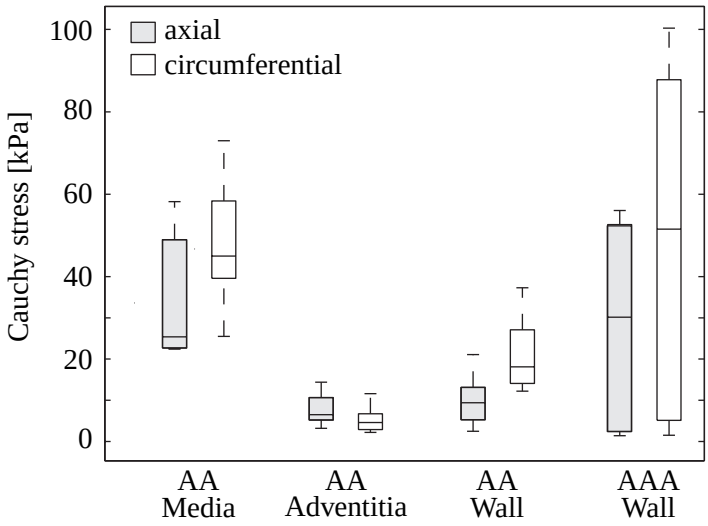

Figure 3.10: Box-and-whisker plots of the Cauchy stress at 1.15 stretch in the axial and circumferential directions for the abdominal aorta (AA) (media, $n = 6$; adventitia, $n = 6$; wall, $n = 7$), and the AAA wall ($n = 7$).

The structural parameters for the AAA wall determined from SHG images are summarized in Table 3.3 and illustrated in form of box-and-whisker plots in Fig. 3.7(a)-(c), while Fig. 3.7(d) shows the AAA wall thickness. The structural parameters for the samples AAA-1 and AAA-4 were only taken from one sample. All AAA samples with the exception of sample AAA-10, which is the ruptured one, showed a similarly high alignment of collagen fibers with a median of $\kappa_{\text{ip}} = 0.229 \pm 0.057$, and the in-plane dispersion did not show any statistical difference with respect to intact AA walls, compare with Tables 3.2 and 3.3. The out-of-plane dispersion was significantly higher ($p < 0.0001$) in AAA samples when compared with healthy (control) samples, as clearly visualized in Fig. 3.7(b) (lower dispersion parameter κ_{op} for AAA walls). In addition, Fig. 3.9 shows the collagen structure of three AAA samples through the thickness indicating a higher out-of-plane dispersion when compared with the layered structure of a healthy abdominal aorta, see, e.g., the image on the bottom of Fig. 3.6(a). Finally, when compared with intact AA walls, AAA samples showed a smaller mean fiber angle α ($p = 0.06$), see Table 3.2.

3.3.3 Biaxial Mechanical Data

The material parameters (c, k_1, k_2) for the abdominal aorta samples and the AAA walls are summarized in Tables 3.4 and 3.5, respectively, whereas the associative structural data, which were used for fitting the individual samples, are summarized in Tables 3.2 and 3.3. The median of R^2 was 0.95 ± 0.05, 0.98 ± 0.03, 0.95 ± 0.12, 0.96 ± 0.04 and 0.93 ± 0.03

Table 3.4: Material parameters (c, k_1, k_2) and related coefficient of determination (R^2) for the intima, media, adventitia and the intact wall of the abdominal aortas determined from biaxial stretching tests; n indicates the number of samples.

	Intima ($n=4$)		Media ($n=9$)		Adventitia ($n=9$)		Intact Wall ($n=7$)	
	Median	$[Q1;Q3]$	Median	$[Q1;Q3]$	Median	$[Q1;Q3]$	Median	$[Q1;Q3]$
c [kPa]	33.86	[6.88;98.76]	16.08	[10.34;30.52]	3.77	[2.18;4.97]	11.59	[4.13;19.93]
k_1 [kPa]	7.79	[4.90,55.00]	11.68	[2.32;22.81]	0.36	[0.06;1.70]	2.66	[1.15;11.64]
k_2 [-]	139.1	[41.95;243.31]	7.18	[2.94;22.78]	45.88	[21.10;69.85]	19.25	[9.93;26.06]
R^2	0.95	[0.93;0.98]	0.98	[0.07;0.99]	0.95	[0.84;0.97]	0.96	[0.94;0.97]

Table 3.5: Material parameters (c, k_1, k_2) and related coefficient of determination (R^2) for the AAA samples determined from biaxial stretching tests. Samples AAA-2 and AAA-10, the two which originate from the ruptured aneurysms, were considered as outliers due to the extreme wall stiffness, and hence were excluded from the statistical analysis of the material parameters.

Patient #	c [kPa]	k_1 [kPa]	k_2 [-]	R^2
AAA-1.1	1.08	0.45	53.33	0.90
AAA-1.2	1.50	1.71	157.89	0.99
AAA-2	0.50	26.94	220.70	0.68
AAA-3	0.23	2.94	28.54	0.89
AAA-4.1	1.66	5.82	99.91	0.98
AAA-4.2	0.54	8.00	100.07	0.94
AAA-5	3.72	2.73	123.52	0.90
AAA-6	3.39	5.49	61.00	0.56
AAA-7	2.47	0.92	12.49	0.97
AAA-8	0.57	4.02	1.44	0.99
AAA-10	600.60	5.70	3315.60	0.76
AAA-11	2.56	0.75	47.33	0.93
Median	1.58	2.84	57.17	0.94
$[Q1;Q3]$	[0.57;2.56]	[0.92;5.49]	[28.54;100.07]	[0.90;0.98]

for the intima, media, adventitia, intact AA wall and AAA wall, respectively. In addition, Fig. 3.10 shows box-and-whisker plots of the Cauchy stress at 1.15 stretch in the axial and circumferential directions for the abdominal aorta (AA) and for the AAA wall; stresses in the circumferential direction of the walls were always higher compared with the axial direction.

Within the healthy group the intima showed a relatively short toe region with a rapid stiffening at a low stretch ($\lambda \sim 1.025$), as also documented in [184], whereas the adventitia was rather compliant ($c = 3.77 \pm 2.79$, $k_1 = 0.36 \pm 1.64$), stiffened at higher stretches and

displayed a significantly higher k_2 value in comparison with the media and the intact wall ($\lambda \sim 1.2$, $k_2 = 45.88 \pm 48.75$). Therefore only one intima sample, not shown in Fig. 3.10, reached a stretch of 1.15. In regard to AA walls, the parameter c for AAA walls was significantly lower ($p = 0.0004$), see Tables 3.4 and 3.5, and Fig. 3.11. However, the dimensionless parameter k_2 with 57.17 ± 71.53, resembling the exponential stiffening of the loading curves due to the collagen fibers, was significantly higher than for AA walls ($k_2 = 19.25 \pm 16.13$, $p = 0.025$). Interestingly, by comparing the adventitia of AAs with AAA tissue the k_2 value was not significantly different between the two groups ($p = 0.40$), however, AAA tissue differed significantly in both the c value ($p = 0.028$) and the k_1 value ($p = 0.022$) with respect to the adventitia of AAs. Figure 3.12 shows equibiaxial mechanical responses (stretch ratio of 1 : 1) of 12 AAA patches.

Linear regression analysis was carried out to test for possible correlations between material and structural parameters, and patient data. Two cases were identified to correlate significantly, see Fig. 3.13.

3.4 Discussion

To the authors' knowledge this is the first study to provide structural data for healthy human (layer-specific) abdominal aortic samples and AAA walls in combination with mechanical data for studying the physiology and pathology of human aortas such as abdominal aortic aneurysms. We have shown that AAA tissues, in contrast to tissues obtained from healthy abdominal aortas, display a substantial variability in fiber architecture, fiber diameter and waviness and in material properties. A combination of optical clearing and SHG imaging was utilized to analyze the 3D microstructure without damaging the tissue structure due to cutting, and the mechanical data were obtained from biaxial stretching tests. The used material model that takes account of the identified non-symmetric arrangement of collagen fibers (Tables 3.2 and 3.3), documented in [199] and reviewed in Section 3.2.3, was capable of providing good fits for the samples of the abdominal aorta, their individual layers and the AAA samples (see Tables 3.4 and 3.5), although there are only three material parameters involved. A novel set of structural and material parameters for the material model [199] is provided to be used in finite element simulations.

In the following section we discuss the obtained structural and mechanical data of the two groups of tissues.

3.4.1 Structural Data

A human abdominal aorta with non-atherosclerotic intimal thickening is composed of three layers, which can clearly be distinguished and dissected. The obtained structural data were similar to those documented in [19], however, the angles α between the mean fiber

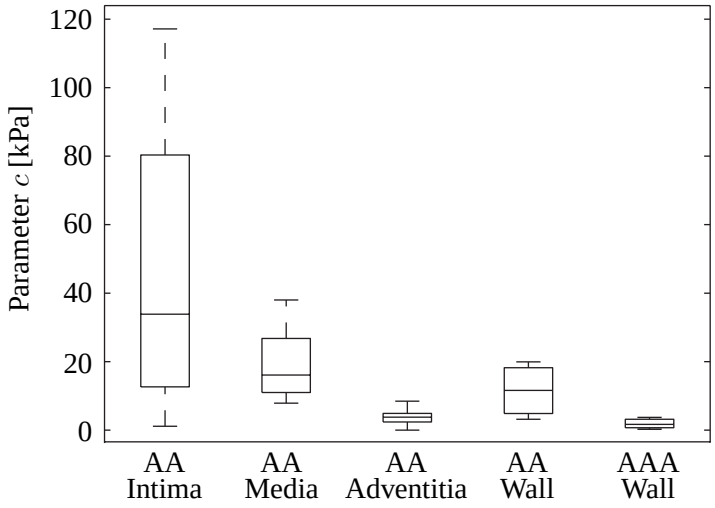

Figure 3.11: Box-and-whisker plots of the parameter c for the abdominal aorta (AA), the individual layers, and for the AAA wall.

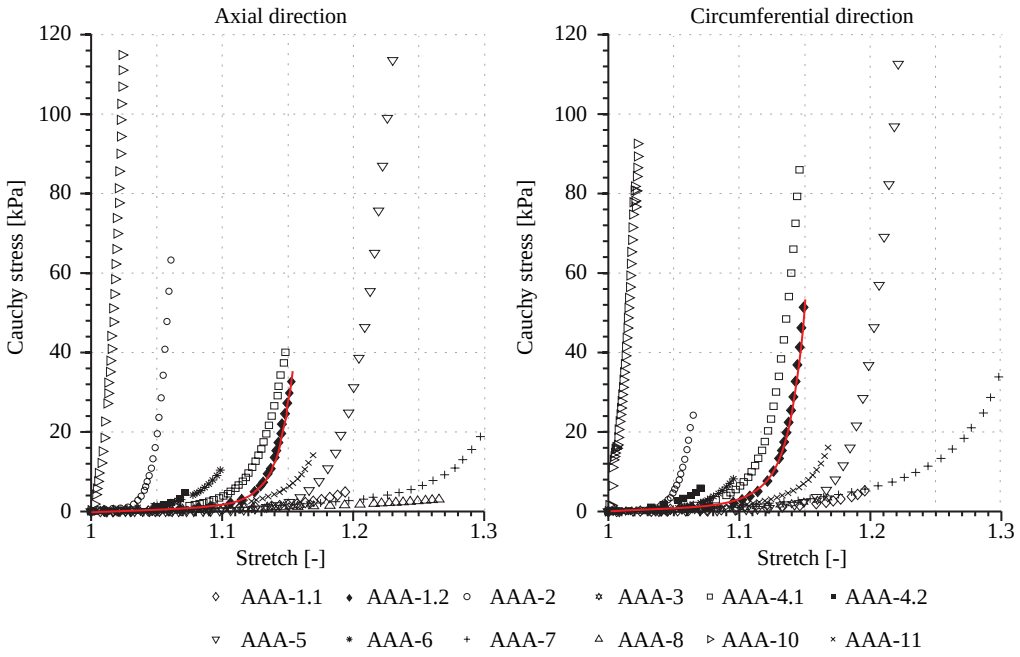

Figure 3.12: Cauchy stress versus stretch behavior of 12 AAA patches obtained from equibiaxial mechanical tests indicating a substantial variability in the mechanical response: (a) axial direction; (b) circumferential direction. The two samples AAA-2 and AAA-10 originate from ruptured aneurysms. The red curves depict an exemplary model fit to sample AAA-1.2.

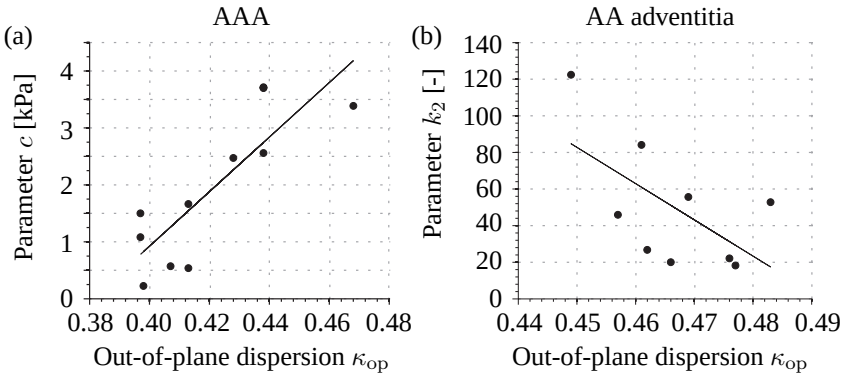

Figure 3.13: Significant correlation of material with structural parameters: (a) parameter c in model (3.8) with out-of-plane dispersion parameter κ_{op} for AAA tissues; (b) parameter k_2 in model (3.9) with κ_{op} for AA adventitial tissues.

direction and the circumferential direction, especially in the media, were smaller than those reported in [19] where polarized microscopy was used in combination with a universal stage. This is most likely due to the different methodology used: in the present study the aortic wall was not pre-stretched, the structure of the tissues were analyzed in the (unloaded) reference configuration and SHG imaging was used. For a short and recent summary of imaging modalities that can reveal the fibrous microstructure including an original investigation of optical polarization tractography to visualize the fiber structure in the bovine carotid artery see [205].

The study [116] also performed an analysis of AAA collagen fiber dispersion in order to gain structural data in the unloaded reference configuration. However, the study has some drawback, which we could avoid. For example, the measurements were performed manually during histological imaging using polarized light microscopy, which requires embedding the sample in paraffin and mechanical sectioning and staining with picrosirius red so that only a very small thin slice of a fixed sample can be imaged. Our approach has the advantages that tissue clearing does not change the dimensions of the sample (shown in [177]), in contrast to [116], who reported a necessary back-calculation to the reference configuration of the collagen orientation due to thickening of the sample after fixation. We did not have to cut and stain the samples to prepare histology which may be accompanied by several artifacts such as shrinkage, distortion, overlapping regions, holes due to calcification just to name a few [206]. In the present study we were able to attain a continuous 3D dispersion of the collagen fiber orientations throughout the entire thickness. Finally, our study protocol enabled a systematic comparison of tissues obtained from healthy AA and AAA, and we conclude that the out-of-plane dispersion of collagen was significantly higher in AAA samples than it was in healthy abdominal aortas.

AAA wall samples showed a large variation in tissue composition including plaque, cystic medial necrosis and adipocytes, consistent with findings reported in [207]. Except for sam-

ple AAA-6, the typical layered structure of AA walls, as analyzed in, e.g., [19, 177], could not be detected. This observation is in accordance with the study [196] which shows a complete loss of the normal architecture and loss of the distinction between medial and adventitial collagen organization. Albeit the small sample size we hypothesize that collagen fibers reorient towards the circumferential direction with disease progression, as the angle towards the circumferential direction was lower in AAA wall samples compared with samples obtained from AA walls. This is in accordance with the studies [109, 110, 113, 130], which reported a pronounced increase in the circumferential stiffness for AAA tissue as compared with AA tissue. As collagen turnover is governed by local stress and strain rates [182], supra-physiological stresses in AAAs may be responsible for the collagen fiber realignment towards the circumferential direction. Although in our study the samples were not pre-stretched, fibers in AAA samples often appeared straight and much thicker than collagen in healthy samples.

The examination of two patches (AAA-4.1, AAA-4.2) taken from adjacent locations of sample AAA-4, see Fig. 3.8(b), showed different structural characteristics and some variation in the mechanical behavior. As the significant influence of the collagen structure on the mechanics of healthy and diseased collagenous tissues has long been known, the different microstructure in adjacent regions of a sample may explain the diversity in local AAA stress states [10, 11, 53, 113, 208]. We found no significant influence of the aneurysm diameter on the structural and material parameters, which strengthens the hypothesis that the diameter criterion is insufficient, which is in line with findings in, e.g, [108, 195].

3.4.2 Mechanical Data

In regard to the mechanical data of AA samples, with a mean age of 63 yr, it is the intima which exhibited a rather stiff mechanical behavior. In healthy young individuals, however, the intima is a single layer of endothelial cells resting on a thin basal membrane. It thickens (and stiffens) with age (arteriosclerosis) so that the mechanical contribution of the intima on the overall stiffening of the wall is significant. Comparing our results of the intact AA wall with the behavior reported in [183] we find a similar behavior. Our peak stretches are in the same range as reported in [183], and the overall mechanical behavior was stiffer in the circumferential direction for all samples. Unfortunately, in [183] a phenomenological Fung-type strain-energy function was utilized, which hampers the comparison of the mechanical response. Although there are only three material parameters involved, the model agrees very well with the experimental data of all samples, whereby the three structural parameters were fixed during the fitting process.

A significant difference in the parameter c, relating to the ground matrix, and k_2, relating to the stiffness of the collagen fabric, between healthy and diseased tissues was observed. The median parameter c is significantly lower in AAA tissue in comparison to AA wall samples, indicating a minor isotropic contribution to the strain-energy function for AAAs.

We also know that the elastin content, which is mainly related to the ground matrix, decreases significantly with increasing AAA diameter, see, e.g., [209], which is depicted by the low c values found in the present study. In addition, [110] discussed a decrease in the initial slope of AAA samples compared with AA wall samples, which also corresponds to our findings of a decreased parameter c. The significantly higher value of the parameter k_2 indicates a stiffer behavior of the AAA tissues when compared with healthy AA wall samples, which was also reported in [108, 110]. However, our samples showed a rather compliant behavior at low stretches and a rapid stiffening at higher stretches, which, to the authors' knowledge, was not yet discussed in previous studies. The present findings of straight and parallel collagen fibers in AAA samples is also along the findings of [196], which demonstrate a deposition of aggregated parallel collagen sheets in AAAs that appear rigid, see, e.g., Fig. 2E in [196].

As can be seen from Fig. 3.12 the biaxial mechanical AAA behavior shows a wide variability, which underlines the importance of patient-specific modeling to assess rupture risk. Any difference in the finding to previous studies could be due to this variability which again highlights the need to acquire structural data in combination with mechanical data in each individual case. The fits of the used material model to the experimental data were very good throughout all AAA samples, with the exception of sample AAA-6 ($R^2 = 0.56$). As the only sample, AAA-6 showed a layered structure, similar to a healthy abdominal aorta. The bad fit of sample AAA-6 in comparison to all other samples, in which the typical layered structure was lost, supports the hypothesis that most AAA walls can be captured by one homogeneous material model. However, healthy abdominal aortas need to be modeled by three layers with specific parameters.

Despite the small number of available samples we report significant correlations between material and structural parameters and patient data, which resulted in two cases, see Fig. 3.13: (i) parameter c, relating to the ground matrix, showed a positive correlation with the out-of-plane dispersion parameter κ_{op} for AAA tissues, with a Pearson correlation coefficient of $r = 0.836$; (ii) parameter k_2 correlated with a negative correlation of $r = -0.612$ with κ_{op} for AA adventitial tissues. Although all layers and parameters were investigated for possible correlations only these two cases showed statistically significant correlations.

3.4.3 Concluding Remarks

The present study documents a novel parameter set consisting of microstructural 3D collagen orientation and dispersion linked to mechanical data of the same specimen obtained from biaxial stretching tests. To the authors' knowledge it is the first biaxially determined data set which is linked to the 3D collagen structure of abdominal aortas, their individual layers and of AAA wall samples. Our results highlight the need to incorporate the significantly different AAA wall structure into continuum models as the structure and the mechanical response differ remarkably from healthy AA walls. Otherwise, numerical results from finite element simulations for AAA tissues, often based on parameters for healthy

aortic tissue, are not a good predictor of the *in vivo* stress state or the risk of rupture. Compared to previous studies attempting to identify distributed collagen fiber orientations in artery walls our method yields a continuous distribution of the collagen fabric throughout the thickness without destroying the tissue, therefore allowing also an investigation of specific regions of interest. Additionally, we analyzed and compared the structure and mechanics of samples obtained from healthy abdominal aortas with AAA samples which allowed new insights. In particular, the out-of-plane dispersion of collagen for AAA tissues was significantly higher than in healthy abdominal aortas. The mechanical and structural data showed not only a rather large variability between the samples but also in adjacent regions of the same sample. This leads to the conclusion that the disease progression in AAAs is a highly localized process, leading to variations in structure in adjacent regions of the same AAA wall. Due to the substantial variability in structure and mechanics it is clear that a 'one-fits-all' criterion such as the diameter criterion is not good enough.

In the future, more effort should be made to better investigate collagen fiber undulation and thickness measurement, as straight and thick collagen struts were spotted on several samples throughout the thickness. Improved imaging of the aorta may provide *in vivo* information regarding aortic geometry, structure and anisotropy, and when combined with a hemodynamic assessment it may have the potential to identify patients at high risk and to access rupture risk individually thereby facilitating prophylactic treatment of aneurysms.

Acknowledgements

The authors would like to thank the Institute of Science and Technology, Klosterneuburg, Austria, for its support in SHG imaging, and M. Habenbacher and L. Marx for their support in the experimental study. In addition, we thank A. Donnerer from the Medical University of Graz for his valuable support during tissue harvesting.

4 THE INFLUENCE OF FIBER DISPERSION ON THE MECHANICAL RESPONSE OF AORTIC TISSUES IN HEALTH AND DISEASE: A COMPUTATIONAL STUDY

Abstract. Changes in the structural components of aortic tissues have been shown to play a significant role in the pathogenesis of aortic degeneration. Therefore, reliable stress analyses require a suitable and meaningful constitutive model that captures micro-structural changes. As recent data show, in-plane and out-of-plane collagen fiber dispersions vary significantly between healthy and aneurysmatic aortic walls. The aim of this study is to computationally investigate the influence of fiber dispersion on the mechanical response of aortic tissues in health and disease. In particular, the influence of three different fiber dispersions is studied: (i) non-symmetric fiber dispersion, the most realistic assumption for aortic tissues; (ii) transversely isotropic dispersion, a special case; (iii) perfectly aligned fibers (no dispersion in either plane), another special case. Explicit expressions for the stress and elasticity tensors as needed for the implementation in a finite element code are provided. Three representative numerical examples are studied: planar biaxial extension, inflation of residually stressed and pre-stretched aortic segments and inflation of an idealized abdominal aortic aneurysm (AAA) geometry. For the AAA geometry the case of isotropic dispersion is additionally analyzed. Documented structural and mechanical parameters are taken from human aortas (healthy media/adventitia and AAA). The influence of fiber dispersions upon magnitudes and distributions of stresses and deformations are presented and analyzed. Stresses varied significantly, especially in the AAA case, where material stiffening is significantly influenced by fiber dispersion. The results highlight the need to incorporate the structural differences into finite element simulations to obtain more accurate stress predictions. Additionally, results show the capability of one constitutive model to represent different scenarios of aortic micro-structures allowing future studies of collagen reorientation during disease progression.

4.1 Introduction

Aortic tissues can be viewed as fibrous composites assembled from a ground matrix and embedded families of collagen fibers with orientations that are distributed spatially. It is well established that the mechanical behavior of fibrous tissues such as arterial walls is strongly influenced by the underlying collagen structure, in particular, by collagen orientation *and* dispersion, see, e.g., [210]. It has been shown that during the development of diseases such as an abdominal aortic aneurysm (AAA) the collagen structure changes significantly. For example, collagen fibers in healthy abdominal aortas are considerably dispersed in-plane (circumferential-axial plane), but have a rather small dispersion out-of-plane (circumferential-radial plane) [19, 211]. AAAs, however, show a significantly higher

dispersion out-of-plane. In addition, by means of several samples it has been shown that the characteristic three-layered wall structure, as seen in healthy abdominal aortas, is no longer present in AAAs [211]. A quantification and analysis of the reorientation of the micro-structure are key to better understand disease progression. The recently proposed model by Holzapfel et al. [199] is one that is able to capture the spatially distributed orientations of collagen fibers in arterial tissues, and, therefore, allows to provide a deeper insight into the (pathological) changes of fibrous tissues as occurring in AAAs.

As mentioned, the mechanical response of aortic tissues is strongly influenced by the underlying collagen structure. Nevertheless, several studies which investigate the magnitude and location of peak wall stresses in AAAs have utilized either isotropic models (see, e.g. [10, 52, 190, 191, 193, 212, 213]) or material parameters which were received from healthy aortic tissues ([108]). Early studies have used the law of Laplace to study the influence of the geometry on AAA stresses [214, 215] or modeled AAAs as axisymmetric membranes [52]. Also linear elastic models were used to study AAA stresses [216, 217]; these models are not able to capture the typical nonlinear behavior of aortic tissues. Studies such as those by Vande Geest et al. [110], Tong et al. [112], O'Leary et al. [113], Sassani et al. [109] or Niestrawska et al. [211] have illustrated that AAA tissues are anisotropic, which requires the consideration of appropriate models and parameters to analysis wall stresses. Especially as three-dimensional (3D) imaging data of the wall micro-structure become available it should be combined with mechanical data to ensure more accurate estimates of wall stress magnitudes and related locations.

The influence of material parameters and models on wall stress predictions was studied by several groups, with contradicting results. While the studies by Raghavan and Vorp [10] and Fillinger et al. [11, 12] stated that the peak wall stress is mainly influenced by AAA shape and/or AAA diameter, Polzer et al. [13] stated that it is important to account for nonlinearity when simulating AAA responses. On the basis of the same AAA geometry Rodríguez et al. [14] showed that the use of an anisotropic model yields higher maximum wall stresses when compared with isotropic models. The same group investigated the influence of anisotropy on peak wall stresses. They also studied the impact of the model on five different patient-specific AAA geometries and concluded that the inclusion of anisotropy scales up the magnitude of peak wall stresses [218]. Additionally they studied the outcome of two different anisotropic models, one of them was the model by Holzapfel et al. [39] and the other one by Rodríguez et al. [14], and they deduced that parameters describing the fiber orientation should always be obtained independently from the fitting of the other parameters to stress-strain data. However, the authors fitted the models they compared to different data sets, hence their conclusion on the influence of fiber dispersion is not that compelling.

To the authors' knowledge the influence of different fiber dispersions on the basis of the structural model by Holzapfel et al. [149] using systematic numerical simulations has not yet been studied. In addition, stress distributions obtained from parameter sets taken

from healthy and diseased aortic tissues have not yet been compared. The present paper aims to investigate the influence of three different fiber dispersions: (i) non-symmetric fiber dispersion, which is the most realistic assumption recently introduced by Holzapfel et al. [149]; (ii) transversely isotropic (rotationally symmetric) dispersion, according to Gasser et al. [134], a special case of [149]; (iii) perfectly aligned fibers (no dispersion in either plane), according to Holzapfel et al. [39], another special case of [149]. All three dispersion assumptions are studied with material and structural parameters obtained from the media and adventitia of healthy abdominal aortic walls, and from one AAA sample [211].

The outline of the paper is as follows. In Section 2 the required continuum mechanical framework is provided by briefly explaining the utilized non-symmetric fiber dispersion model [149]. In addition, explicit expressions for the stress and elasticity tensors are provided, as needed for the implementation in a finite element code. In Section 3 the used method is described, i.e. different fiber dispersions are studied using three representative numerical examples, and related finite element simulations are performed. The results of these simulations are then summarized and discussed in Section 4, which is followed by a conclusion.

4.2 Continuum Mechanical Framework

This section briefly reviews the required continuum mechanical framework, with notation according to [173], and summarizes the used non-symmetric fiber dispersion model. It provides the background for the mathematical description of the stress and elasticity tensors needed for the implementation in the general purpose finite element analysis program FEAP [135].

4.2.1 Kinematics

Let Ω_0 be a reference (or undeformed) configuration and Ω its current (or deformed) configuration. The deformation map $\chi(\mathbf{X})$ transforms a material point $\mathbf{X} \in \Omega_0$ into a spatial point $\mathbf{x} \in \Omega$. With this map we define the deformation gradient $\mathbf{F} = \partial\chi(\mathbf{X})/\partial\mathbf{X}$ that allows to map a tangent vector $\mathrm{d}\mathbf{X}$ from the reference to the current configuration via $\mathrm{d}\mathbf{x} = \mathbf{F}\mathrm{d}\mathbf{X}$. The determinant of $\mathbf{F}$ is denoted by J and describes the ratio between the volume in the current and the reference configuration. For incompressible materials, as considered in the present work, J requires to be equal to unity [173]. For subsequent use we decouple $\mathbf{F}$ into a spherical (dilatational) part $J^{1/3}\mathbf{I}$ and a unimodular (distortional) part $\overline{\mathbf{F}} = J^{-1/3}\mathbf{F}$, with $\det\overline{\mathbf{F}} \equiv 1$; the second-order unit tensor is denoted by $\mathbf{I}$. The right Cauchy–Green tensor $\mathbf{C} = \mathbf{F}^{\mathrm{T}}\mathbf{F}$ and the left Cauchy–Green tensor $\mathbf{b} = \mathbf{F}\mathbf{F}^{\mathrm{T}}$ are defined together with their

modified counterparts $\overline{\mathbf{C}} = \overline{\mathbf{F}}^{\mathrm{T}}\overline{\mathbf{F}}$ and $\overline{\mathbf{b}} = \overline{\mathbf{F}}\overline{\mathbf{F}}^{\mathrm{T}}$, respectively, with the related invariants $I_1 = \mathrm{tr}\mathbf{C} = \mathrm{tr}\mathbf{b}$ and $\bar{I}_1 = \mathrm{tr}\overline{\mathbf{C}} = \mathrm{tr}\overline{\mathbf{b}}$.

4.2.2 Non-symmetric Fiber Dispersion Model

Let us now introduce the probability density $\rho(\Theta,\Phi)$ of the (collagen) fiber orientation in the reference configuration in terms of the two angles Θ and Φ [149]. The experimentally observed distribution of the collagen fibers in the aorta is non-symmetric [19, 211] so that we decompose ρ in the form $\rho(\Theta,\Phi) = \rho_{\mathrm{ip}}(\Phi)\rho_{\mathrm{op}}(\Theta)$, where $\rho_{\mathrm{ip}}(\Phi)$ and $\rho_{\mathrm{op}}(\Theta)$ describe the in-plane and out-of-plane dispersions, respectively. For ρ_{ip} and ρ_{op} we consider the von Mises distributions of the forms

$$\rho_{\mathrm{ip}}(\Phi) = \frac{\exp[a\cos 2(\Phi \pm \alpha)]}{I_0(a)}, \qquad \rho_{\mathrm{op}}(\Theta) = 2\sqrt{\frac{2b}{\pi}}\frac{\exp[b(\cos 2\Theta - 1)]}{\mathrm{erf}(\sqrt{2b})}, \tag{4.1}$$

where a and b are constant concentration parameters, $I_0(a)$ is the modified Bessel function of the first kind of order 0, and α denotes the angle between the mean fiber direction and the circumferential direction of the blood vessel. To include the fiber dispersion into a strain-energy function, two scalar measures can be defined according to [149], namely

$$\kappa_{\mathrm{ip}} = \frac{1}{2} - \frac{I_1(a)}{2I_0(a)}, \qquad \kappa_{\mathrm{op}} = \frac{1}{2} - \frac{1}{8b} + \frac{1}{4}\sqrt{\frac{2}{\pi b}}\frac{\exp(-2b)}{\mathrm{erf}(\sqrt{2b})}, \tag{4.2}$$

where $I_1(a)$ is the modified Bessel function of the first kind of order 1, and $0 \leq \kappa_{\mathrm{ip}} \leq 1$ and $0 \leq \kappa_{\mathrm{op}} \leq 1/2$.

We introduce now two symmetric fiber families with the (in-plane) mean fiber directions

$$\mathbf{M}_4 = \cos\alpha\mathbf{e}_1 + \sin\alpha\mathbf{e}_2, \qquad \mathbf{M}_6 = \cos\alpha\mathbf{e}_1 - \sin\alpha\mathbf{e}_2, \tag{4.3}$$

where $\mathbf{e}_1$ denotes the circumferential direction and $\mathbf{e}_2$ the axial direction of the blood vessel. Additionally, we introduce the invariants I_4, I_6 and I_{n}, i.e.

$$I_i = \mathbf{C} : \mathbf{M}_i \otimes \mathbf{M}_i, \quad i = 4,6, \qquad I_{\mathrm{n}} = \mathbf{C} : \mathbf{M}_{\mathrm{n}} \otimes \mathbf{M}_{\mathrm{n}}, \tag{4.4}$$

where $\mathbf{M}_{\mathrm{n}}$ is a unit out-of-plane vector. The related modified invariants are simply $\bar{I}_i = J^{-2/3}I_i$ and $\bar{I}_{\mathrm{n}} = J^{-2/3}I_{\mathrm{n}}$.

To include the fiber dispersion in the strain-energy function, say Ψ, the generalized structure tensors $\mathbf{H}_4$ and $\mathbf{H}_6$, describing the material behavior, are used, i.e.

$$\mathbf{H}_i = A\mathbf{I} + B\mathbf{M}_i \otimes \mathbf{M}_i + (1 - 3A - B)\mathbf{M}_{\mathrm{n}} \otimes \mathbf{M}_{\mathrm{n}}, \qquad i = 4,6, \tag{4.5}$$

with the constants

$$A = 2\kappa_{\mathrm{op}}\kappa_{\mathrm{ip}}, \qquad B = 2\kappa_{\mathrm{op}}(1 - 2\kappa_{\mathrm{ip}}). \tag{4.6}$$

According to [173] the strain-energy function Ψ (per unit reference volume) is now additively decomposed into Ψ_{vol}, describing the volumetric elastic response, and $\overline{\Psi}$ describing the isochoric elastic response. Thus,

$$\Psi = \Psi_{\text{vol}}(J) + \overline{\Psi}(\overline{\mathbf{C}}, \mathbf{H}_4, \mathbf{H}_6), \tag{4.7}$$

where $\Psi_{\text{vol}} = \bar{\kappa}(\ln J)^2/2$ serves here as a penalty function, and $\bar{\kappa}$ is a (positive) penalty parameter (for the subsequent analyses we used 10 000 kPa). The isochoric part $\overline{\Psi}$ of Ψ has now the form

$$\overline{\Psi} = \Psi_{\text{g}}(\overline{\mathbf{C}}) + \sum_{i=4,6} \Psi_{\text{f},i}(\overline{\mathbf{C}}, \mathbf{H}_i), \tag{4.8}$$

where

$$\Psi_{\text{g}}(\overline{\mathbf{C}}) = \frac{c}{2}(\bar{I}_1 - 3) \tag{4.9}$$

captures the energy stored in the ground matrix, with c representing the stiffness of the (non-collageneous) matrix, and the contribution $\Psi_{\text{f},i}$ of the two fiber families is captured by

$$\Psi_{\text{f},i}\left(\overline{\mathbf{C}}, \mathbf{H}_i\right) = \frac{k_1}{2k_2}[\exp(k_2 \overline{E}_i^2) - 1], \qquad i = 4, 6, \tag{4.10}$$

where $k_1 > 0$ is a stress-like parameter and $k_2 > 0$ is a dimensionless parameter, while $\overline{E}_i$ are quantities according to

$$\overline{E}_i = \text{tr}(\mathbf{H}_i \overline{\mathbf{C}}) - 1 = A\bar{I}_1 + B\bar{I}_i + (1 - 3A - B)\bar{I}_{\text{n}} - 1, \qquad i = 4, 6. \tag{4.11}$$

In (4.11) the mean fiber directions $\mathbf{M}_i$ are included in form of the invariants $\bar{I}_i$, while the dispersion parameters κ_{ip} and κ_{op} are considered in the constants A and B.

Stress Tensors

The second Piola-Kirchhoff stress tensor $\mathbf{S}$ describes the change of the strain energy with respect to $\mathbf{C}$ and is defined by $\mathbf{S} = 2\partial\Psi/\partial\mathbf{C}$. Using the introduced decoupled form of the strain-energy function (4.7) two stress contributions can be identified such that $\mathbf{S} = \mathbf{S}_{\text{vol}} + \overline{\mathbf{S}}$. The volumetric part is derived by means of the chain rule, which reads

$$\mathbf{S}_{\text{vol}} = 2\frac{\partial \Psi_{\text{vol}}(J)}{\partial J}\frac{\partial J}{\partial \mathbf{C}} = pJ\mathbf{C}^{-1}, \qquad p = \frac{\mathrm{d}\Psi_{\text{vol}}(J)}{\mathrm{d}J}, \tag{4.12}$$

where p denotes the hydrostatic pressure. The isochoric contribution to $\mathbf{S}$ is obtained by

$$\overline{\mathbf{S}} = 2\frac{\partial \overline{\Psi}}{\partial \mathbf{C}} = J^{-2/3}\mathbb{P} : \tilde{\mathbf{S}}, \qquad \tilde{\mathbf{S}} = 2\frac{\partial \overline{\Psi}}{\partial \overline{\mathbf{C}}}, \tag{4.13}$$

where $\mathbb{P} = \mathbb{I} - \frac{1}{3}\mathbf{C}^{-1} \otimes \mathbf{C}$ is the projection tensor in the Lagrangian setting, $\mathbb{I}$ is the fourth-order identity tensor and $\tilde{\mathbf{S}}$ is the fictitious second Piola-Kirchhoff stress tensor. According to the introduced structure of the strain-energy function (4.8) we may write $\tilde{\mathbf{S}}$ as

$$\tilde{\mathbf{S}} = \tilde{\mathbf{S}}_{\mathrm{g}} + \sum_{i=4,6} \tilde{\mathbf{S}}_{\mathrm{f},i}, \qquad \tilde{\mathbf{S}}_{\mathrm{g}} = 2\frac{\partial \Psi_{\mathrm{g}}}{\partial \overline{\mathbf{C}}} = c\mathbf{I}, \quad \tilde{\mathbf{S}}_{\mathrm{f},i} = 2\frac{\partial \Psi_{\mathrm{f},i}}{\partial \overline{\mathbf{C}}} = 2\psi_i' \mathbf{H}_i, \tag{4.14}$$

where (4.9)-(4.11) and the abbreviation

$$\psi_i' = \frac{\partial \Psi_{\mathrm{f},i}}{\partial \overline{E}_i} = k_1 \overline{E}_i \exp(k_2 \overline{E}_i^2) \tag{4.15}$$

have been used.

For the finite element implementation we use the Kirchhoff stress tensor τ, which is the push forward of $\mathbf{S}$ so that

$$\tau = \mathbf{F}\mathbf{S}\mathbf{F}^{\mathrm{T}} = \tau_{\mathrm{vol}} + \overline{\tau}, \tag{4.16}$$

where

$$\tau_{\mathrm{vol}} = pJ\mathbf{I}, \qquad \overline{\tau} = \mathbb{P} : \tilde{\tau}, \tag{4.17}$$

$\mathbb{P} = \mathbb{I} - \frac{1}{3}\mathbf{I} \otimes \mathbf{I}$ is the projection tensor (deviatoric operator) in the Eulerian description, and $\tilde{\tau}$ is the push forward of the fictitious second Piola-Kirchhoff tensor given in eq. $(4.13)_2$. The contributions of the ground matrix and the fibers to the fictitious stress can be split according to

$$\tilde{\tau} = \tilde{\tau}_{\mathrm{g}} + \sum_{i=4,6} \tilde{\tau}_{\mathrm{f},i}, \tag{4.18}$$

which is the analogue of eq. $(4.14)_1$. Hence, from $(4.14)_2$ and $(4.14)_3$ we get the fictitious Kirchhoff stress tensors by a push-forward operation according to

$$\tilde{\tau}_{\mathrm{g}} = \overline{\mathbf{F}}\tilde{\mathbf{S}}_{\mathrm{g}}\overline{\mathbf{F}}^{\mathrm{T}} = c\overline{\mathbf{b}}, \qquad \tilde{\tau}_{\mathrm{f},i} = \overline{\mathbf{F}}\tilde{\mathbf{S}}_{\mathrm{f},i}\overline{\mathbf{F}}^{\mathrm{T}} = 2\psi_i'\overline{\mathbf{h}}_i, \tag{4.19}$$

where the definition for the Eulerian structure tensors

$$\overline{\mathbf{h}}_i = \overline{\mathbf{F}}\mathbf{H}_i\overline{\mathbf{F}}^{\mathrm{T}}, \qquad i = 4,6, \tag{4.20}$$

has been introduced.

Elasticity Tensors

The decoupled form of the Eulerian elasticity tensor $\mathbb{c}$ can be obtained in an analogous manner as the decoupled stress tensor $(4.16)_2$, i.e.

$$\mathbb{c} = \mathbb{c}_{\mathrm{vol}} + \overline{\mathbb{c}}, \tag{4.21}$$

with $\mathbb{c}_{\text{vol}} = \tilde{p}\mathbf{I}\otimes\mathbf{I} - 2p\mathbb{I}$, where $\tilde{p} = p + J\mathrm{d}p/\mathrm{d}J$, and [173]

$$J\overline{\mathbb{C}} = \mathbb{P} : \tilde{\mathbb{C}} : \mathbb{P} + \frac{2}{3}\mathrm{tr}(\tilde{\boldsymbol{\tau}})\mathbb{P} - \frac{2}{3}(\mathbf{I}\otimes\overline{\boldsymbol{\tau}} + \overline{\boldsymbol{\tau}}\otimes\mathbf{I}), \tag{4.22}$$

where $\tilde{\mathbb{C}}$ is the fourth-order fictitious elasticity tensor in the Eulerian description, defined as the push-forward operation of $2J^{-4/3}\partial\tilde{\mathbf{S}}/\partial\overline{\mathbf{C}}$. By using the specific choice of the strain-energy function and the derived stress relation (4.14) for $\tilde{\mathbb{C}}$ we obtain the explicit form

$$\tilde{\mathbb{C}} = 4J^{-4/3}\psi_i''\overline{\mathbf{h}}_i\otimes\overline{\mathbf{h}}_i, \tag{4.23}$$

where the definition (4.20) and the abbreviation

$$\psi_i'' = \frac{\partial^2\Psi_{\mathrm{f},i}}{\partial\overline{E}_i^2} = k_1(1+2k_2\overline{E}_i^2)\exp(k_2\overline{E}_i^2) \tag{4.24}$$

have been used. Hence, with (4.23), (4.20) and the stress tensors (4.18) and $(4.17)_2$ the purely isochoric contribution $\overline{\mathbb{C}}$ to the Eulerian elasticity tensor can be calculated from relationship (4.22).

By considering minor and major symmetries of the elasticity tensors the Voigt notation was then used for the implementation in the finite element analysis program FEAP [135].

4.3 Methods

Here we describe three cases of fiber dispersions and the (material and structural) parameters used for the analysis of three examples, which are also outlined in detail.

4.3.1 Parameters Used for the Numerical Analyses

We are studying three different cases of fiber dispersions:

(i) Non-rotationally symmetric dispersion (i.e. the general case), as introduced in 2015, and reviewed in Section 4.2; for more details see Holzapfel et al. [149]. We refer to this case as NRSD (non rotationally-symmetric dispersion).

(ii) Transversely isotropic (rotationally symmetric) dispersion, as introduced in the GOH model in 2006, see Gasser et al. [134]. For this case the structure tensors (4.5) have the special form

$$\mathbf{H}_i = \kappa\mathbf{I} + (1-3\kappa)\mathbf{M}_i\otimes\mathbf{M}_i, \tag{4.25}$$

where $\kappa\in[0,1/3]$ is a single dispersion parameter. Equation (4.25) is obtained from (4.5) by taking $\kappa = 1-2\kappa_{\text{op}}$, which corresponds to $A=\kappa$, $B=1-3\kappa$. We refer to this special case as TID (transversely isotropic dispersion).

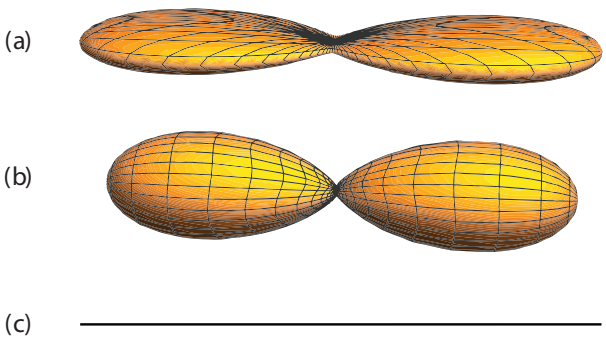

Figure 4.1: Visualization of three cases of fiber dispersions defined by $\rho(\mathbf{N})\mathbf{N}$, with $\rho = \rho_{\text{ip}}\rho_{\text{op}}$ according to (4.1), where the distance from the center to the surface represents the probability of finding a fiber in the direction $\mathbf{N}$: (a) non-rotationally symmetric dispersion (the general case); (b) transversely isotropic dispersion; (c) perfectly aligned fibers. The plots have been scaled differently.

(iii) Perfectly aligned fibers (no dispersion in either plane), as introduced in the HGO model in 2000, see Holzapfel et al. [39]. For this special case both concentration parameters (a, b) become infinite so that $\kappa_{\text{op}} \to 1/2$. The structure tensors (4.5) are then $\mathbf{H}_i = \mathbf{M}_i \otimes \mathbf{M}_i$. This corresponds to $A = 0$, $B = 1$ in (4.5). We refer to this special case as PA (perfect alignment).

Figure 4.1 depicts a visualization of $\rho(\mathbf{N})\mathbf{N}$ (for just one family of fibers), where the unit vector $\mathbf{N}$ is an arbitrary fiber direction in the reference configuration, for (a) the general case for which $\mathbf{H}_i$ is given by (4.5), (b) the transversely isotropic dispersion (TID) with $\mathbf{H}_i$ given by (4.25) and (c), the case of perfect alignment (PA) of collagen fibers.

As mentioned above the fiber dispersions described in (ii) and (iii) are special cases of the non-rotationally symmetric dispersion model, which is considered to be the reference model. Subsequently, we use material and structural parameters for the media and adventitia of healthy abdominal aortas (median values) according to Niestrawska et al. [211]. The material parameters (c, k_1, k_2) were determined from biaxial stretching tests and adopted from Table 4 in [211], while the structural parameters (κ_{ip}, κ_{op}, α) were determined from second harmonic generation images and adopted from Table 2 in [211]. In addition, we also use structural and material parameters from one AAA wall sample, and adopt the values from Tables 3 and 5 in [211], i.e. sample AAA-5. The parameters are summarized in Table 1. For the case of transversely isotropic dispersion we take $\kappa_{\text{op}} = 0.414, 0.406$ for the media and adventitia of the healthy abdominal aorta, respectively, and 0.397 for the AAA wall. These values are calculated using the relationship $\kappa_{\text{op}} = 1/2(1 + \kappa_{\text{ip}})$, where κ_{ip} is taken from Table 1. That relationship results from the symmetry of the structure tensor (in-pane and out-of-plane dispersions are symmetric). From these values it is straightforward to determine the individual dispersion parameter κ and the corresponding constants

	c (kPa)	k_1 (kPa)	k_2 (–)	κ_{ip} (–)	κ_{op} (–)	α ($^\circ$)
Media	16.08	11.68	7.18	0.208	0.487	6.91
Adventitia	3.77	0.36	45.88	0.232	0.466	77.53
AAA	3.72	2.73	123.52	0.261	0.438	9.05

Table 4.1: Material parameters (c, k_1, k_2) from biaxial stretching tests and structural parameters (κ_{ip}, κ_{op}, α) from second harmonic generation images, for healthy medias and adventitias of human abdominal aortas (median values), and for one AAA wall sample; taken from Tables 2-5 of Niestrawska et al. [211].

A and B. Finally, for the perfectly aligned fibers we set $A = 0$, $B = 1$ ($\kappa_{op} = 1/2$). These material and structural parameters are now taken for the subsequent three examples.

4.3.2 Planar Biaxial Extension

On the basis of a planar equibiaxial extension test we study the three different cases of fiber dispersions, as discussed in the previous section. In particular, we consider samples of a healthy media and a AAA wall with the dimension $20 \times 20 \times 1.5$ mm, which resembles the geometry used for the actually performed biaxial extension experiments documented in [211].

Four hexahedral mixed $Q1$-$P0$ elements (constant pressure and trilinear displacement interpolations) are used for the discretization of a cuboid, which is reinforced by two symmetric fiber families located in the ($\mathbf{e}_1$, $\mathbf{e}_2$) plane, see Fig. 4.2. The samples are subjected to equibiaxial extension within the ($\mathbf{e}_1$, $\mathbf{e}_2$) plane up to a stretch of $\lambda_{circ} = \lambda_{axial} = 1.25$, using a displacement-driven analysis. The analytical solutions are calculated according to [149] using MATLAB [219] and compared with the finite element solutions computed by means of FEAP [135].

4.3.3 Inflation of Residually Stressed and Pre-stretched Aortic Segments

Here we study the influence of the fiber dispersion on the mechanical response of residually stressed and pre-stretched (idealized) aortic segments. In particular, a healthy aorta consisting of media and adventitia, and an aneurysmatic abdominal aorta are analyzed.

Geometry

The wall thickness and axial length are chosen to be 1.5 mm, whereas the initial inner radius R_i is 10 mm. For the healthy aortic segment the thickness ratio of media/adventitia is chosen following experimental findings, see [19] and [211], i.e. 70% of the wall thickness

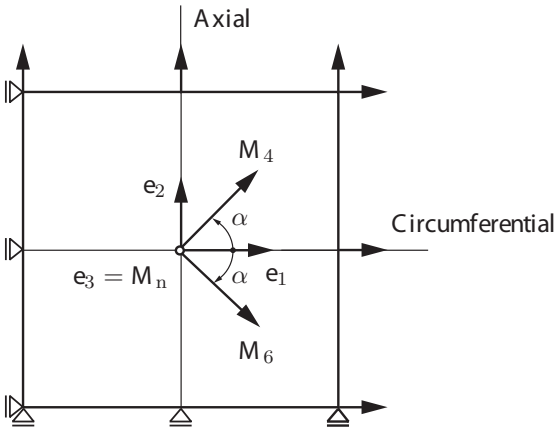

Figure 4.2: Cuboid-shaped sample of a healthy media (and a AAA wall) reinforced by two symmetric fiber families, denoted by $\mathbf{M}_4$ and $\mathbf{M}_6$, and subjected to equibiaxial extension within the ($\mathbf{e}_1$, $\mathbf{e}_2$) plane.

is occupied by the media, and 30% by the adventitia. The AAA segment is modeled as one single layer with 1.5 mm wall thickness. The initial (stress-free) geometry is a cylindrical segment cut open with an opening angle of 180° (defined according to Fig. 3 in [39]), which is slightly smaller than opening angles reported for healthy abdominal aortas [220, 221]. For a better comparison of the material responses between healthy and diseased segments, and as there are no experimental data available on opening angles for aneurysmatic aortas, the same opening angle is chosen for both cases.

Finite Element Model

The geometry is discretized by one element in the axial direction, 70 elements in the circumferential direction and 10 elements in the radial direction. For the healthy aortic segment 7 elements are used for the media in the radial direction, and 3 elements for the adventitia.

Figure 4.3 shows the steps performed during the simulation. Due to symmetry, only one eighth of the aortic segment is simulated, therefore, the opening angle is $180^\circ/2 = 90^\circ$. In step 1 the segment is closed to form a quarter of the segment by constraining surface A in the 2 direction and surface B in both the 1- and 2 directions, and by applying the SPIN command in FEAP to surface B. This command rotates the selected nodes around the center and respective to a defined axis of rotation. Simultaneously, the lower surface D is restricted in the 3 direction. Then, the upper and lower surfaces C and D are restricted in the 3 direction and A and B are constrained in the 2 direction only. In step 2 the aortic segment is stretched by an axial pre-stretch λ_z of 1.0675, achieved by a displacement-driven loading on surface C (the pre-stretch is calculated for the corresponding age following the approach

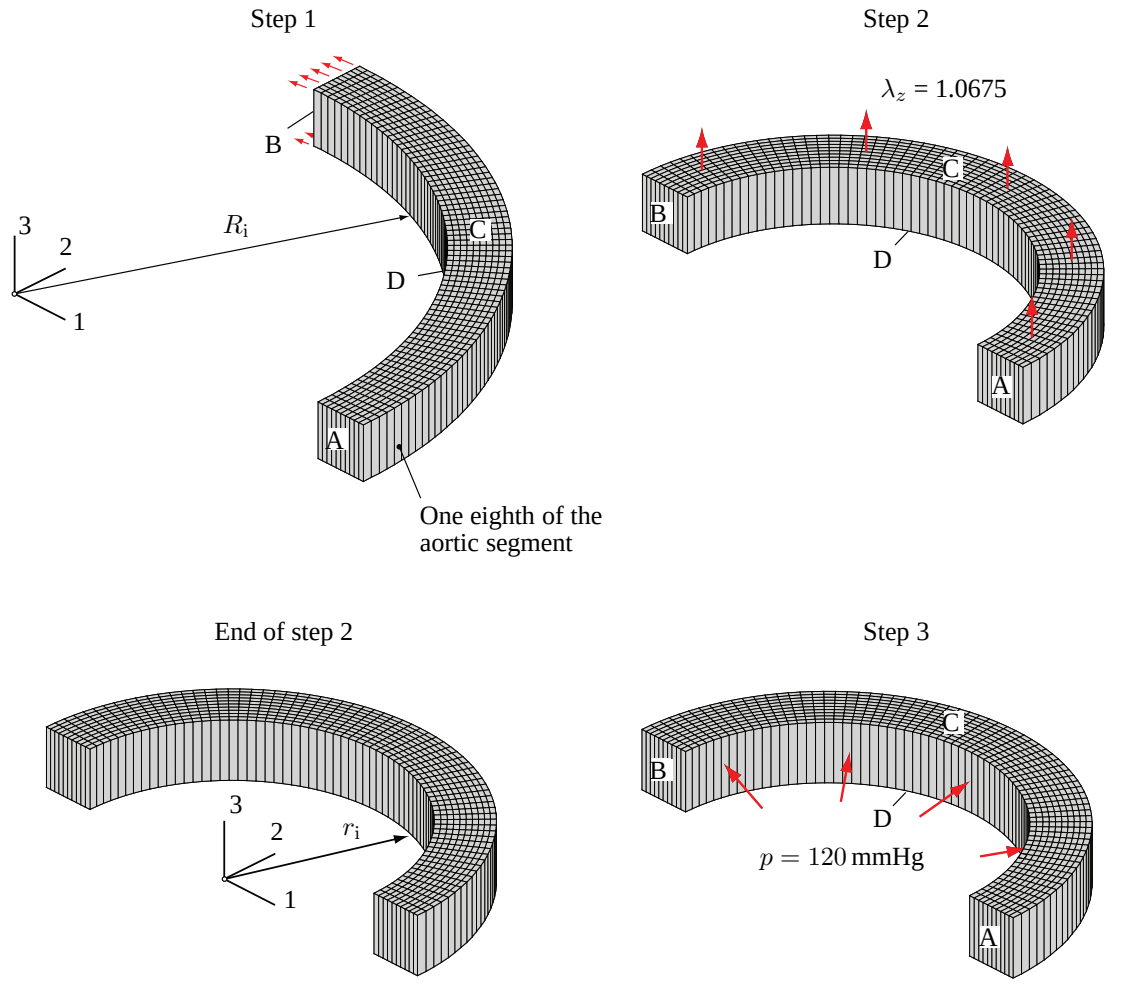

Figure 4.3: Three steps performed during the simulation of a residually stressed and pre-stressed (cylindrical) aortic segment. Due to symmetry one eighth of the segment is simulated. First, the opening angle of 180° (90° because of symmetry) of the segment with inner radius R_i is closed; second, an axial pre-stretch of $\lambda_z = 1.0675$ is applied to obtain the inner radius r_i; third, the aortic segment is pressurized with an inner pressure p up to 120 mmHg.

proposed by Horn et al. [222]). At the end of step 2 the inner radius r_i is taken for the normalization of subsequent plots. In step 3 (the last step) the boundary conditions are left unchanged with respect to step 2, and the aortic segment is inflated with an inner pressure p of 120 mmHg using a pressure boundary loading (pressure loads depend on the deformation).

4.3.4 Inflation of an Idealized AAA Geometry

The final example underlines the importance of using accurate fiber dispersions in AAA simulations. We are utilizing an idealized AAA geometry to study the effects of fiber dispersions on the mechanical AAA response in a repeatable way using a mathematical function for the AAA shape; therefore, a patient-specific geometry is deliberately not used. In this example we use again the material and structural parameters from Section 4.3.1, and, in addition, we analyze a fourth case, namely isotropic fiber dispersion which is represented by a uniform dispersion in each plane so that $\rho_{\text{ip}} = \rho_{\text{op}} = 1$, where the structure tensor is simply $(1/3)\mathbf{I}$. Hence, we have no preferred direction so that $\kappa = 1/3$ in (4.25), with $A = 1/3$ and $B = 0$ in (3.5).

Geometry

The idealized geometry of the AAA segment is generated using the toolkit CUBIT [223] and MATLAB [219]. The initial AAA thickness is chosen to be the same as in the example of Section 4.3.3, i.e. 1.5 mm. The (total) length L of the AAA model is 160 mm, while the AAA shape, i.e. the change in the radius R, is defined by a 'parabolic-exponential shape' function proposed by Elger et al. [52], and utilized in, e.g., [14]. Thus,

$$R(Z) = R_{\text{a}} + \left(R_{\text{an}} - R_{\text{a}} - c_3 \frac{Z^2}{R_{\text{a}}} \right) \exp\left(-c_2 \left| \frac{Z}{R_{\text{a}}} \right|^{c_1} \right), \tag{4.26}$$

where Z denotes the axial coordinate, R_{a} is the radius of the healthy aorta (for the analyses we use $R_{\text{a}} = 15$ mm), R_{an} is the maximum radius of the aneurysm (at $Z = 0$), $c_1 = 0.5$ is a constant and c_2 and c_3 are defined as

$$c_2 = \frac{4.605}{(0.5 L_{\text{an}}/R_{\text{a}})^{c_1}}, \qquad c_3 = \frac{R_{\text{an}} - R_{\text{a}}}{R_{\text{a}} (0.8 L_{\text{an}}/R_{\text{a}})^2}, \tag{4.27}$$

where L_{an} is the length of the aneurysm (Rodríguez et al. [14]). For a sketch of one eighth of the AAA geometry see Fig. 4.4. Following [14] we us the dimensionless geometrical parameters

$$F_{\text{R}} = \frac{R_{\text{an}}}{R_{\text{a}}}, \qquad F_{\text{L}} = \frac{L_{\text{an}}}{R_{\text{an}}}, \tag{4.28}$$

where F_{R} is the ratio between the AAA radius and the radius of the healthy aorta, and F_{L} is the ratio between the length of the aneurysm L_{an}, and the maximum AAA radius; we use $F_{\text{R}} = 2.5$ and $F_{\text{L}} = 2.8$.

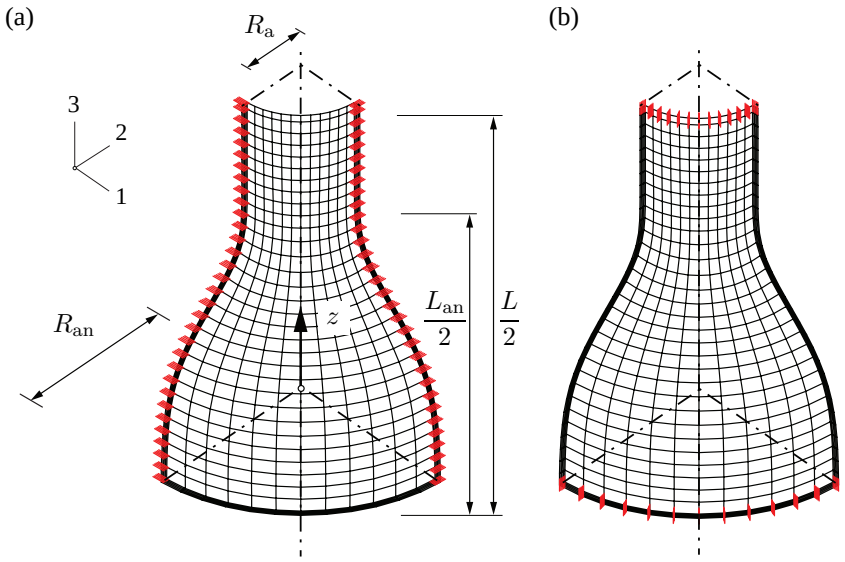

Figure 4.4: One eighth of the AAA geometry and applied boundary conditions in (a) along the directions 1 and 2, and (b) along the direction 3; L is the (total) length of the AAA model, L_{an} is the length of the aneurysmatic part, R_a is the radius of the healthy aorta (at $Z = 0$), R_{an} is the maximum radius of the aneurysm (at $Z = L/2$), while Z denotes the local axial coordinate, see Elger et al. (4.27).

Finite Element Model

The 3D geometry is discretized with CUBIT, and the analysis is performed with FEAP using 1 488 hexahedral mixed $Q1$-$P0$ elements. An inner pressure of 16 kPa ($\sim$ 120 mmHg) is applied to simulate the mean blood pressure. Symmetric boundary conditions are employed allowing the simulation of only one eighth of the geometry, which reduces the computational time significantly. The axial direction is restricted on both outlets, see Fig. 4.4.

Definition of Fiber Orientation

In order to include the fiber orientation, the local circumferential, axial and radial vectors of a finite element, say $\mathbf{e}_1^{\text{local}}$, $\mathbf{e}_2^{\text{local}}$, $\mathbf{e}_3^{\text{local}}$, need to be identified. This task is straightforward for a cylindrical geometry but it is more elaborate for a AAA geometry, where the local axial direction varies as well. We include the fiber dispersion by using a local coordinate system for each individual finite element. Three nodes on the upper (top) surface and three nodes on the lower (bottom) surface of an individual element are used to define two planes. Hence, two orthogonal vectors to these planes can be identified, i.e. $\mathbf{e}_3^{\text{top}}$ and $\mathbf{e}_3^{\text{bottom}}$, see Fig. 4.5. Consequently, we define the local radial (unit) vector as

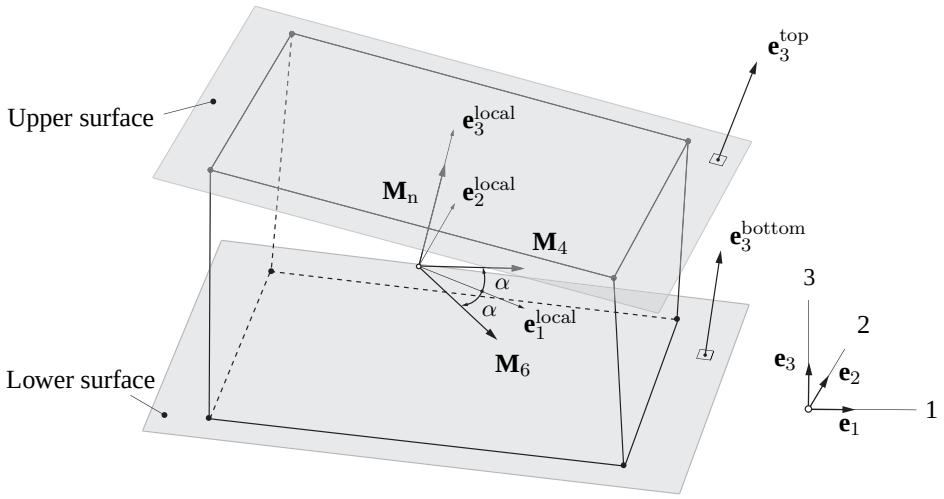

Figure 4.5: Local vectors $\mathbf{e}_1^{\text{local}}$, $\mathbf{e}_2^{\text{local}}$, $\mathbf{e}_3^{\text{local}}$ required for the definition of the local fiber orientations within an individual finite element.

$$\mathbf{e}_3^{\text{local}} = \frac{\mathbf{e}_3^{\text{top}} + \mathbf{e}_3^{\text{bottom}}}{|| \, \mathbf{e}_3^{\text{top}} + \mathbf{e}_3^{\text{bottom}} \, ||}. \tag{4.29}$$

Subsequently, the local circumferential vector $\mathbf{e}_1^{\text{local}}$ is calculated by using the cross product of the global axial vector $\mathbf{e}_2$ and the calculated local radial vector $\mathbf{e}_3^{\text{local}}$, i.e.

$$\mathbf{e}_1^{\text{local}} = \mathbf{e}_2 \times \mathbf{e}_3^{\text{local}}. \tag{4.30}$$

Finally, the local axial vector $\mathbf{e}_2^{\text{local}}$ is calculated as

$$\mathbf{e}_2^{\text{local}} = \mathbf{e}_3^{\text{local}} \times \mathbf{e}_1^{\text{local}}. \tag{4.31}$$

By utilizing the local coordinate system the mean fiber directions, as introduced in Section 4.2.2, are then determined as

$$\mathbf{M}_4 = \cos\alpha \mathbf{e}_1^{\text{local}} + \sin\alpha \mathbf{e}_2^{\text{local}}, \qquad \mathbf{M}_6 = \cos\alpha \mathbf{e}_1^{\text{local}} - \sin\alpha \mathbf{e}_2^{\text{local}}, \tag{4.32}$$

and $\mathbf{M}_{\text{n}} = \mathbf{e}_3^{\text{local}}$.

4.4 Simulation Results and Discussion

This section documents the numerical results of the systematically performed simulations of the three representative examples according to Section 4.3, and it provides short discussions.

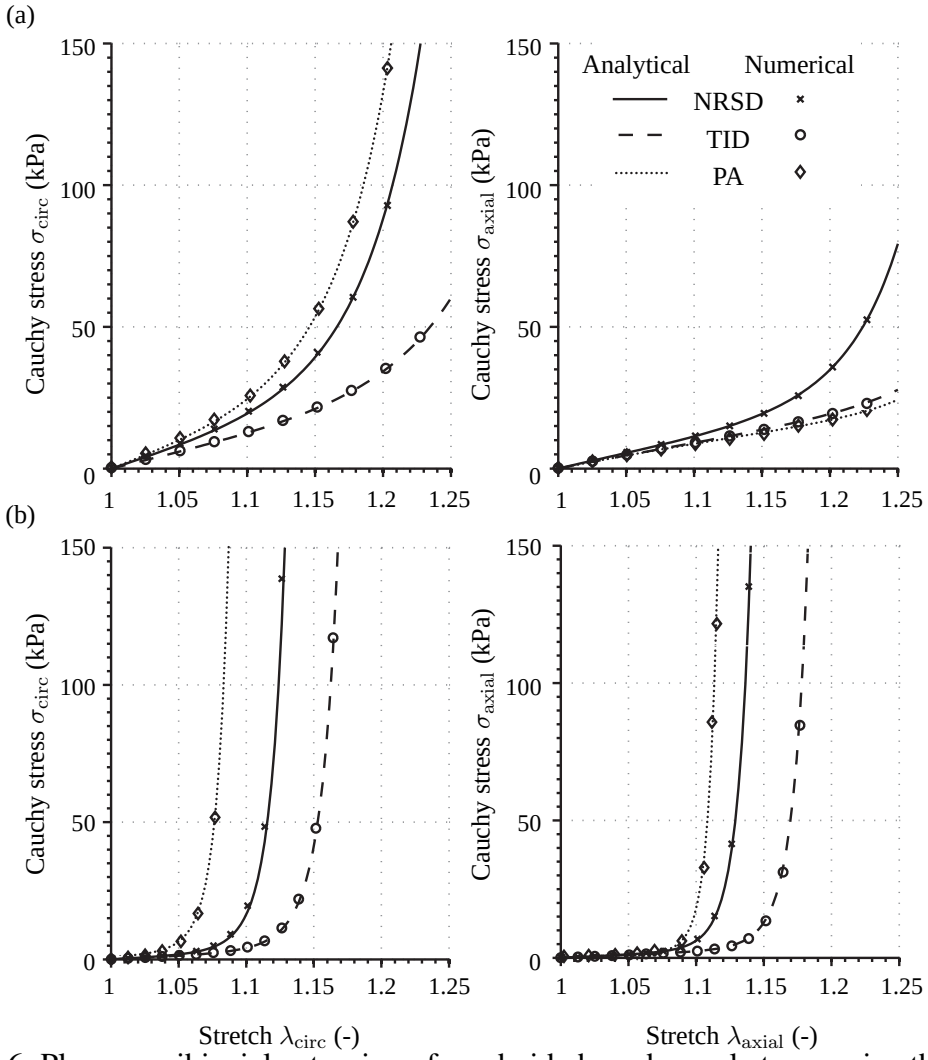

Figure 4.6: Planar equibiaxial extension of a cuboid-shaped sample to examine the difference in the mechanical behavior due to non-symmetric dispersion (NRSD), transversely isotropic dispersion (TID) and perfect alignment (PA) of fibers. Analytical and numerical (FE) solutions are compared: (a) healthy media, (b) AAA wall.

4.4.1 Planar Biaxial Extension

Figure 4.6 displays plots for the Cauchy stress (σ_{circ}, σ_{axial}) versus the related stretch (λ_{circ}, λ_{axial}) for a sample of the healthy media and one for the AAA wall considering the fiber dispersions NRSD, TID and PA. The numerical (FE) and the analytical results coincide very well, which indicates the correct implementation of the material model into FEAP [135]. As can be seen, the fiber dispersion has a significant influence on the mechanical behavior of the samples.

Images indicate that collagen fibers exhibit a very small out-of-plane dispersion for the

	HEALTHY MEDIA				
	Circumferential		Axial		
Stretch λ	1.15	1.20	1.15	1.20	
Stress σ	41.06	92.92	19.50	35.23	NRSD
	21.68	35.39	13.84	19.37	TID
	56.36	141.10	12.25	15.57	PA
	AAA WALL				
	Circumferential		Axial		
Stretch λ	1.15	1.20	1.15	1.20	
Stress σ	1.99	19.54	1.31	6.84	NRSD
	1.42	4.47	1.13	2.49	TID
	6.51	879.9	1.14	10.87	PA

Table 4.2: Stresses σ (in kPa) at two stretches λ (in the circumferential and axial directions) of the equibiaxially loaded cuboid-shaped sample for NRSD, TID and PA of fibers, for the healthy media and the AAA wall.

healthy media but a significant in-plane dispersion [139, 211]. TID assumes too little in-plane fibers leading to a weaker material response in both circumferential and axial direction compared with NRSD, see Fig. 4.6(a). If PA is used (with $\alpha = 6.91^{\circ}$) then too many fibers reinforce the circumferential direction, therefore, a PA of fibers overestimates the stiffness in the circumferential direction and underestimates it in the axial direction when compared with NRSD. The nonlinear stiffening in the axial direction can only be captured with the use of NRSD. Table 4.2 summarizes the Cauchy stresses (in kPa) at 1.15 and 1.20 stretch. Stresses in the circumferential direction at 1.20 stretch for PA of fibers are overestimated by 52% compared with NRSD, whereas the axial Cauchy stress is underestimated by 56%. The TID underestimates both circumferential and axial stresses by 62% and 45%, respectively.

A similar tendency can be seen for the AAA sample, although the out-of-plane dispersion of fibers is (much) higher for AAAs compared with healthy tissues.Especially when stresses are compared at stretches of 1.05 and 1.10 the differences become clear, see Table 4.2. The analysis based on PA of fibers shows a faster stiffness when compared with TID and NRSD. At $\lambda_{\text{circ}} = 1.05$ the related stress is already 327% higher compared with NRSD, and at $\lambda_{\text{circ}} = 1.10$ the circumferential Cauchy stress is about 45 times higher for PA with respect to NRSD.

4.4.2 Inflation of Residually Stressed and Pre-stretched Aortic Segments

Figure 4.7 illustrates the thickness change of the aortic wall with respect to the inner pressure p for the healthy aortic and AAA segments. Initial thickness, at $p = 0$, is with respect to the configuration 'end of step 2', as marked in Fig. 4.3. The closing of the open segments results in different wall thicknesses before inflation. For the AAA segment the wall thicknesses at $p = 0$ are quite dependent on the used fiber-reinforcement (see Fig. 4.7(b)), because the AAA segment is much stiffer than the healthy aortic segment. As can be seen, the choice of the fiber dispersion is strongly influencing the results. For both investigated segments the analyses with PA of fibers provide (by far) the stiffest response, resulting in a 5.6% smaller wall thickness at 120 mmHg when compared with NRSD for the AAA segment. On the other hand the segments with TID show the most compliant responses, while the mechanical responses with NRSD are in between. The difference of the material behavior between the two segments (healthy aorta versus AAA) is as pronounced as already shown in Section 4.4.1.

Figure 4.8 depicts 3D plots of the circumferential and axial stresses versus the inner pressure and the normalized radius for the AAA segment, and compares the influence of the three different dispersion assumptions. The current radius is here normalized with the inner radius r_{i}, as depicted in the configuration 'end of step 2' of Fig. 4.3. Especially, the circumferential and axial stresses analyzed on the basis of PA of fibers are significantly different with respect to the other two fiber dispersions, with a peak circumferential (Cauchy) stress of over 300 kPa.

Figure 4.9 depicts the distributions of the circumferential Cauchy stresses with respect to the geometry at 120 mmHg. Clearly, wall thicknesses and radii differ between the healthy and aneurysmatic segments, and also between the different fiber dispersions.

4.4.3 Inflation of an Idealized AAA Geometry

Figure 4.10 shows circumferential and axial (Cauchy) stresses versus the (current) inner radius for different fiber dispersions up to 120 mmHg for (a) the cylindrical segment (healthy aorta) at the smallest radius (at $Z = L/2$), and (b) at the maximum radius of the bulged AAA segment (at $Z = 0$). All simulations except for the one which considers isotropic dispersion show compressive axial stresses in the cylindrical (healthy) part of the aorta, which occur due to the boundary conditions. In addition, the circumferential stresses are higher with isotropic dispersion (ISO) as they are with NRSD and TID. The cylindrical segment with the smallest radius and the maximum radius of the bulged AAA segment (with ISO) exhibit the largest radial extension (with a value of 53.54 mm at 120 mmHg), not having enough fibers located in the circumferential direction to prevent excessive extension due to the applied pressure. TID exhibits a more compliant behavior in the diseased region (with respect to NRSD) with a maximal circumferential stress of 760.7 kPa, whereas

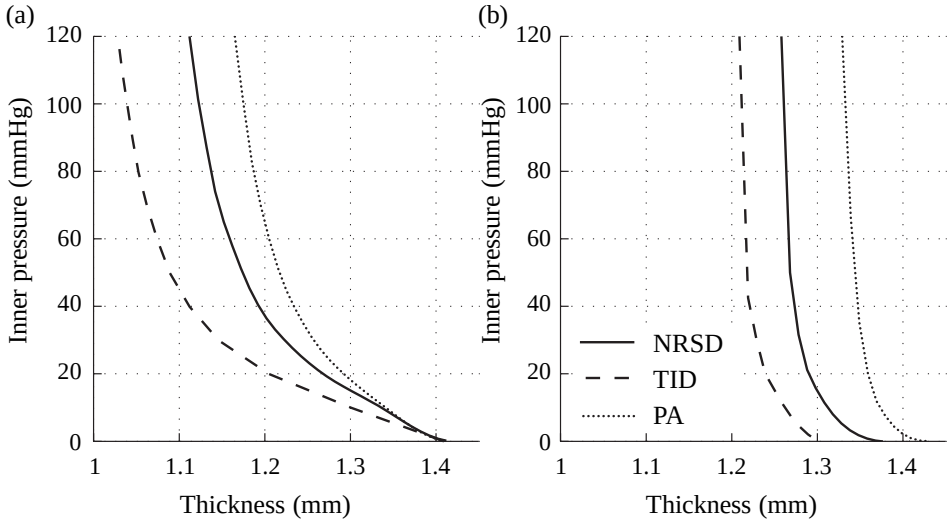

Figure 4.7: FE results of wall thickness versus inner pressure for (a) the healthy aortic segment and (b) the AAA wall using three different fiber dispersions: non rotationally-symmetric dispersion (NRSD), transversely isotropic dispersion (TID), perfect alignment (PA) of fibers.

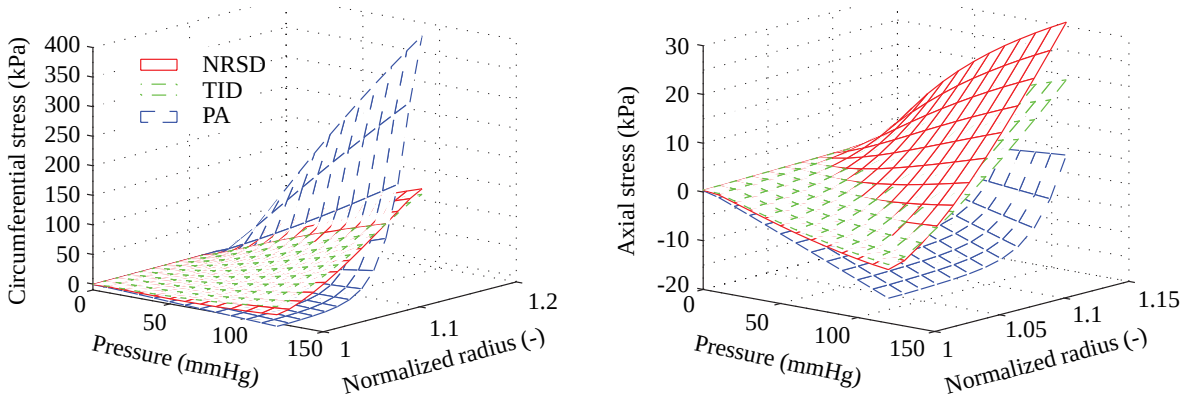

Figure 4.8: FE results of circumferential and axial (Cauchy) stresses versus normalized radius and inner pressure for the AAA segment with three different fiber dispersions: non-symmetric dispersion (NRSD), transversely isotropic dispersion (TID), perfect alignment (PA) of fibers.

NRSD reaches 674.2 kPa at a maximal inner radius of 42.9 mm. Note that no solutions for the AAA with PA of fibers can be displayed, as this case showed numerical instabilities at higher pressure levels in the neck region. This is most likely due to the significant differences in stiffness between the compliant ground matrix and the (relatively) stiff fibers. As there is no fiber dispersion and the fibers are located close to the circumferential direction

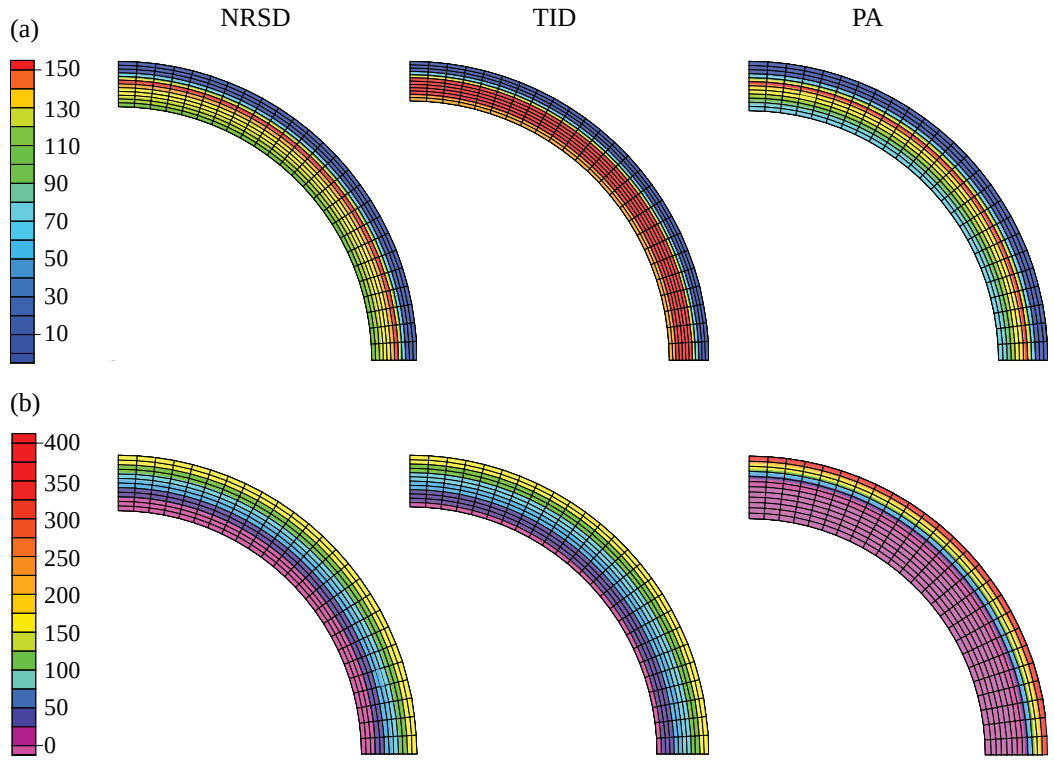

Figure 4.9: FE results of the circumferential stress distributions (in kPa) at 120 mmHg for (a) the healthy aortic segment and (b) the AAA segment using three different fiber dispersions: non-symmetric dispersion (NRSD), transversely isotropic dispersion (TID), perfect alignment (PA) of fibers. Note the different scales for the stress in (a) and (b).

numerical instabilities occur, which may arise due to the used isochoric-volumetric split of the strain-energy function (see, e.g., [224]).

Figure 4.11 shows circumferential and axial (Cauchy) stresses as a function of the radius r normalized with R_{an} for different assumptions of fiber dispersions. The analysis on the basis of an isotropic dispersion predicts axial stresses almost twice as high as for TID and NRSD. The prediction of circumferential stresses obtained on the basis of TID is higher than those using NRSD throughout the wall thickness.

Figure 4.12(a) shows contour plots of the circumferential Cauchy stress for the three simulations at 120 mmHg. The scale of the stress is the same for all simulations. In Fig. 4.12(b) the stress scale is changed so that the location of the maximal stress is visible in the ISO stress plot. All three analyses reveal that the peak wall stress is located at the luminal side of the AAA. The peak circumferential stress (which was almost identical with the maximal principal stresses) occurs at the maximum diameter except for ISO, where the maximum stress is located at the transition zone, compare with Fig. 4.12, hence an isotropic model

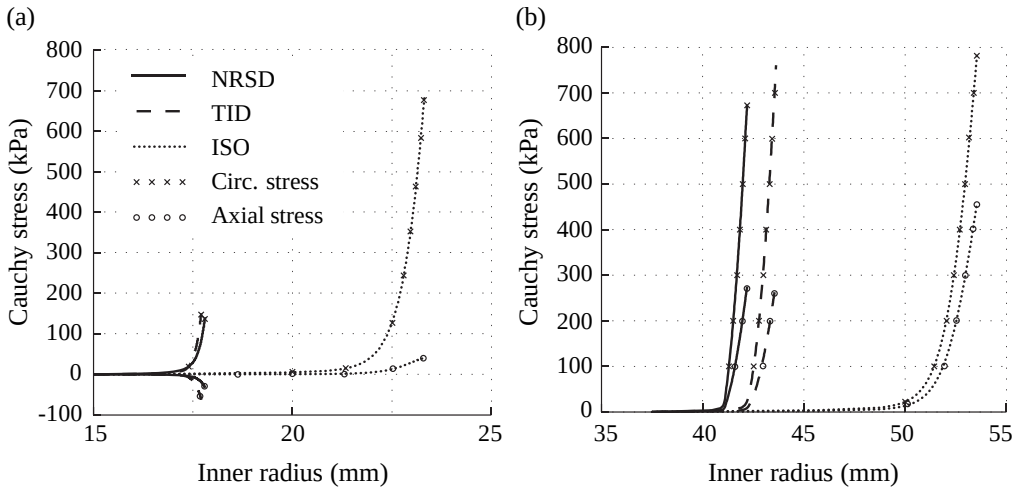

Figure 4.10: Circumferential and axial stresses versus (current) inner radius up to 120 mmHg for (a) the cylindrical segment (healthy aorta) at the smallest radius (at $Z = L/2$) and (b) at the maximum radius of the bulged AAA segment (at $Z = 0$). Three different fiber dispersions are investigated: non-symmetric dispersion (NRSD), transversely isotropic dispersion (TID), isotropic (ISO).

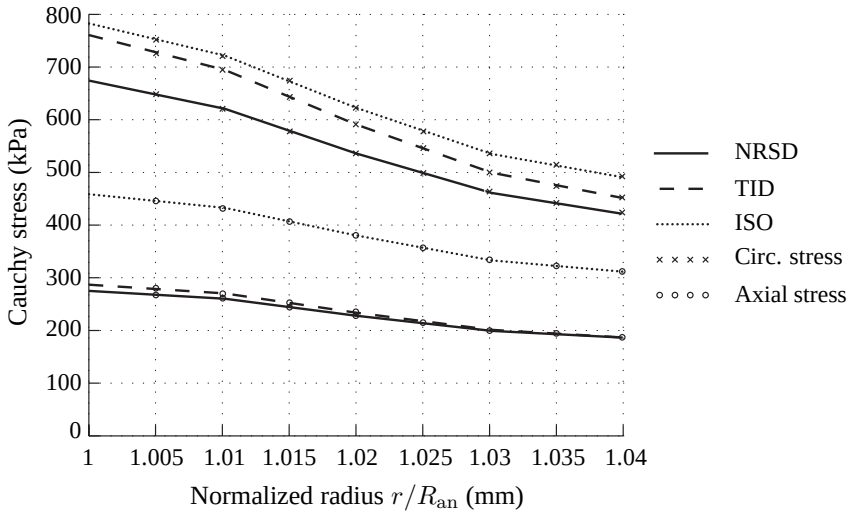

Figure 4.11: Circumferential and axial stresses versus normalized radius r/R_{an} for three different assumptions of fiber dispersions: non-symmetric dispersion (NRSD), transversely isotropic dispersion (TID), isotropic (ISO).

is inappropriate for this type of analysis. The stress distributions between the cases NRSD and TID are not as pronounced as with respect to ISO, because AAA tissues exhibit a rather large out-of-plane dispersion, closer to a rotationally symmetric dispersion, than it is the case for healthy aortas.

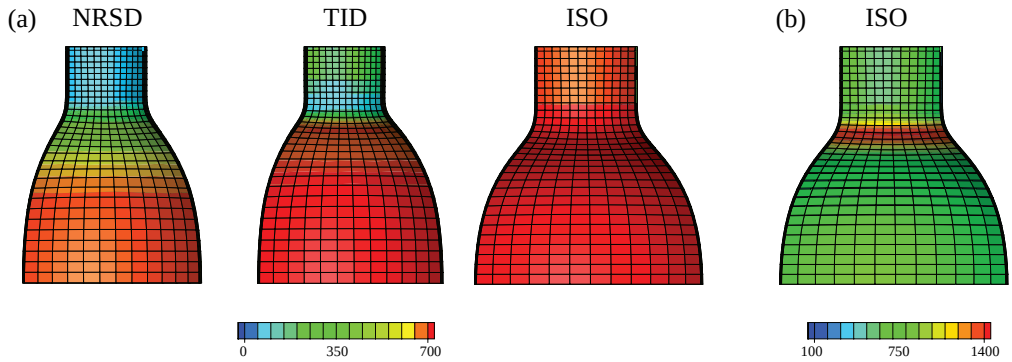

Figure 4.12: Contour plots of the circumferential stress (in kPa) on the luminal side at 120 mmHg: (a) three different assumptions of fiber dispersions (using the same scale), i.e. non-symmetric dispersion (NRSD), transversely isotropic dispersion (TID), isotropic (ISO); (b) stress plot for the case ISO with a stress scale which makes the location of the peak wall stress in the transitional zone visible.

Previous studies detected peak wall stresses at inflection points and a pronounced influence of asymmetry on the location of the peak wall stress [14, 129, 190, 192]. Interestingly, in the present example only the isotropic model exhibits peak wall stresses at the inflection point. Rodríguez et al. [218] demonstrated that an anisotropic model yields much higher wall stresses when compared with an isotropic model; the authors also discussed the influence of fiber dispersion. However, the models the authors used are not comparable, as they fitted their models to different data sets, using different fitting procedures. The present simulation of an idealized AAA geometry shows twice as high maximal stresses for the isotropic case compared to the anisotropic cases. As the used structural and material parameters are not comparable with the ones used by Rodríguez et al. [218] the differences in the findings highlight the influence of parameters and model assumptions on stress magnitudes and locations.

4.5 Conclusion

The influence of different fiber dispersions on the mechanical response of aortic tissues in health and disease has not yet been studied on the basis of the recent constitutive model of Holzapfel et al. [149]. In the present study we have performed a systematic analysis using three representative numerical examples. Magnitudes and distributions of stresses and deformations were presented and discussed. We have used structural and mechanical data from human aortic samples (healthy media/adventitia and AAA), recently documented by Niestrawska et al. [211].

Simulations performed with data from healthy aortas show a (more) gradual stiffening, whereas the simulations with AAA data predict a very compliant response at low stretches, then a kind of ‘stiffening point’ at which a rapid stiffening of the material response occurs.

For that stiffening the collagen micro-structure is mainly responsible. Therefore, for AAA tissues it is even more important to consider the corresponding fiber dispersion. In all three examples it is visible that structural and material data from healthy aortic tissues yield a (completely) different material response when compared with AAA tissue. Consequently, data from healthy tissues should not be used for the prediction of peak wall stresses in AAAs, or *vice versa*.

All simulations show a rather remarkable influence of the fiber dispersion on the magnitudes and distributions of stresses and deformations. The most severe difference can be appreciated in the example analyzing the inflation of an idealized AAA geometry. For example, the peak circumferential stress is more than twice as high with isotropic dispersion compared with non-symmetric dispersion, and even the related location of the peak stress is different. The computational study indicates that small changes in the fiber dispersion result in a rather different tissue behavior. Hence, as long as structural parameters are available they should be considered in the analysis, especially as the computational time is about the same for different arterial micro-structures. Clearly, it is not sufficient to use phenomenological models to understand disease progression.

Future studies should focus on the inclusion of new imaging data of the micro-structure. Intermediate stages of AAA formation should also be studied on, e.g., mouse models to provide data for more detailed micro-structural modeling and analyses. Another key research topic is certainly the collection of structural data *in vivo*, which would help to establish more realistic rupture criteria, and to better understand collagen reorientation during disease progression.

Acknowledgements. The authors would like to thank Jakob Eckmann for the constructive discussion on the computational analysis.

5 THE ROLE OF TISSUE RE-MODELING IN MECHANICS AND PATHOGENESIS OF ABDOMINAL AORTIC ANEURYSMS

Abstract. Arterial walls can be seen as composite materials consisting of collagen fibers embedded in an elastic matrix and smooth muscle cells. The remodeling of the structural proteins has been shown to play a significant role in the mechanical behavior of arteries during pathogenesis of abdominal aortic aneurysms (AAA).

In this study, we systematically studied the changes in microstructure, histology and mechanics to link them to AAA disease progression. We performed biaxial extension tests, second harmonic generation imaging and histology on 15 samples from the anterior part of AAA walls harvested during open aneurysm surgery.

Structural data was gained by fitting to a bivariate von-Mises distribution and yielded the mean fiber direction and in- and out-of-plane fiber dispersion. Mechanical and structural data was fitted to a recently proposed constitutive model. Additionally, the mechanical data was used to derive collagen recruitment points in the obtained strain-stress-curves. 14 parameters were derived from histology such as smooth muscle cell-, elastin-, and abluminal adipocyte content. In total, 21 parameters were obtained and statistically evaluated.

We were able to define stages of disease progression based on the collagen recruitment points. Significant differences in elastin content, collagen orientation and adipocyte content were found. Nerves entrapped inside AAA walls pointed towards a significant deposition of newly formed collagen abluminally, which we propose as neo-adventitia formation. We were able to discriminate two kinds of remodeled walls with a high collagen content - potentially safely and possibly vulnerable walls with a high adipocyte content inside the wall as well as significant amounts of inflammation.

The study yielded a novel hypothesis for disease progression, derived from the systematic comparison of histology, structure and mechanical changes in AAAs.

5.1 Introduction

Abdominal aortic aneurysms (AAAs) are local dilatations of the abdominal aorta. The bulge is weakening the blood vessel wall and appears predominantly in the elderly male population [4, 180]. AAAs are usually clinically silent and may rupture eventually if not treated [11]. The mortality rate in these cases lies around 85% [5]. Especially in older patients the treatment of AAAs with elective surgical repair does not necessarily improve survival [7]. Hence, a reliable, patient specific prediction of rupture risk is needed to assess whether the risk of rupture justifies repair [179]. The current criterion for surgery is the 'maximum diameter criterion', which is more a rule-of thumb than a scientific criterion

[11, 124]. Other criteria have been proposed, such as the expansion rate [126], aneurysm asymmetry [129] or peak wall stresses [225, 226]. However, no criterion has been proven to be reliable up until now. Malkawi et al. [9] suggested that a biomechanical patient specific screening should be employed as finite element simulations (FEM) are becoming more promising.

From a mechanical point of view, AAA rupture is a mechanical failure of the material once the peak wall stress exceeds the local strength [181]. As material properties depend significantly on the network of the extra cellular matrix (ECM) including elastin and collagen, which are the primary load bearing proteins in the arterial wall [182]), changes in these components play a substantial role in pathogenesis. Therefore, a deeper understanding on the structure and ongoing reorganization during disease progression is essential. Studies which investigated wall stresses computationally were performed e.g. by [11, 191]. Studies like this have a pressing need for physiological data on the material and structural level. Over the past decade AAAs were studied widely especially mechanically. Biaxial extension tests in AAA were performed by, e.g., [110, 112, 211, 227]. Studies, which performed uniaxial extension tests and reported a stiffer behavior in circumferential direction were, e.g. [107–109], whereas, e.g. [53, 57, 185–188] reported an increase in isotropy in uniaxial extension tests. Additionally, the pressure modulus was investigated as a mechanical parameter by [98, 103]. The microstructure was linked to mechanics to improve the outcome of FEM simulations by, e.g. [198], studying porcine aortic tissue. Robertson et al. [197] studied the reorganization of collagen fibers during loading in cerebral aneurysms. In our recent study [211] we investigated the differences in microstructure and mechanics between healthy and AAA. Last but not least, the pathogenesis linked to material properties was investigated in several studies, such as [110, 116, 194–196]. Monteiro et al. [188] correlated the AAA diameter with collagen, smooth muscle cell (SMC), elastin content, the infiltration of inflammatory cells and the (uniaxial) rupture strength of 90 patients. Specimen with higher diameters showed higher values of failure properties. However, there was no difference in strain when looking at the diameter and no other correlations were found, either. However, the specific mechanical events leading to AAA development and eventually to rupture still remain unclear.

Elastin degradation seems to be accepted as the main reason for the development of an aneurysmal dilatation [228]. Wilson et al. [229] investigated markers for elastin degradation linked to a pressure strain elastic modulus and found that elastin degradation correlates with increased wall distensibility and aneurysm formation. Data on changes in collagen however is conflicting. Some authors report an increase in collagen fraction [230, 231], while others report a reduction [194, 232] or no change [58, 233]. The exact order of pathological events leading to AAA initiation is not yet completely understood [234]. However, a consensus exists on the most important processes during the development of AAA, which are chronic inflammation, production of matrix degrading proteinases and their inhibitors [207]. Additionally, immunity seems to play a key role in aneurysm development [235]. After the dilatation caused by the loss of elastin the adventitia is accepted to be the main

load bearing part in the aortic wall. Eventually, collagen disruption seems to be the cause of rupture [207].

In our recent study [211] we observed significant amounts of adipocytes abluminally, covered by collagen within the wall, not adjacent to the outer side of the adventitia as usually observed in healthy abdominal aortas [15]. Only two groups seem to have mentioned these entrapped adipocytes, e.g., [236–239] in AAA and [240] in transcranial aneurysms, but none investigated their influence on the mechanical behavior of the wall. However, the mentioned studies all hypothesized that adipocyte accumulations within the wall might be key factors that cause wall degeneration and eventually rupture. In transcranial aneurysms, adipocyte accumulations were associated with SMCs and were hypothesized to originate from the thrombus or neo-vessels. In AAA Tanaka et al. [238, 239] and Kugo et al. [236, 237] performed studies on mouse models and human samples and found that adipocyte like cells mostly accumulate in the abluminal side of the aneurysmal sack, but not in the neck. They noted that inflammation is associated with these adipocytes, but did not provide a hypothesis where the adipocytes may originate from. The adipose tissue surrounding healthy vessels was mentioned in several studies, such as [21, 241], hypothesizing that this tissue could influence the pathogenesis within the adventitia of the adjacent vascular wall.

Adipocyte accumulations seem to be an important factor in the mechanical behavior of AAAs and therefore motivated this study. It is the first study to our knowledge to investigate systematically the correlations between mechanics, utilizing biaxial extension tests, microstructure gained by second harmonic generation imaging (SHG) and multiple histological parameters to define three stages of disease progression and therefore a new hypothesis on pathogenesis.

5.2 Materials and Methods

5.2.1 Tissue Preparation

Fifteen wall samples from (true) AAAs (with a median (interquartile range (iqr) of 69 (65 to 77) years, 2 women, 13 men) were harvested from open aneurysm repair at the anterior side of the aneurysm at the Department of Vascular Surgery, Medical University Graz, Austria. The AAA samples were small pieces with the longitudinal direction marked by a surgical clip or suture and stored in Dulbecco's modified Eagle's medium at 4°C until testing.

As a representative control sample for histology one sample from an abdominal aorta with non-atherosclerotic intimal thickening was collected within 24 h of death and fixed in 4% formaldehyde solution (pH 7.4) during autopsy. All other data on healthy abdominal aortas relevant to this study was already collected and reported in our previous study [211].

The AAA tissue was cut into three separate samples as indicated in Figure 5.1. First, a rectangular sample with a size approximately 15×5 mm with the long side marking the circumferential direction was prepared and fixed in 4% formaldehyde solution (pH 7.4) for further histological analysis as explained in section 5.2.2.

Subsequently a second rectangular sample, similar to the first one, was prepared for optical clearing, following the protocol in [177]. The specimens were dehydrated by means of a graded ethanol series consisting of 50%, 70%, 95% and $2 \times 100\%$ ethanol solutions for each 30 minutes. The tissue was then cleared by submerging it first into a benzyl alcohol benzyl benzoat (BABB) solution [177] mixed with ethanol in the ratio 1 : 1 for 4 hours. Finally the specimens were placed in 100% BABB for at least 12 hours before imaging as explained in section 5.2.3.

Finally a square sample with dimensions of 20×20 mm was prepared for mechanical testing as explained in section 5.2.4 and the circumferential direction was marked with a surgical marker.

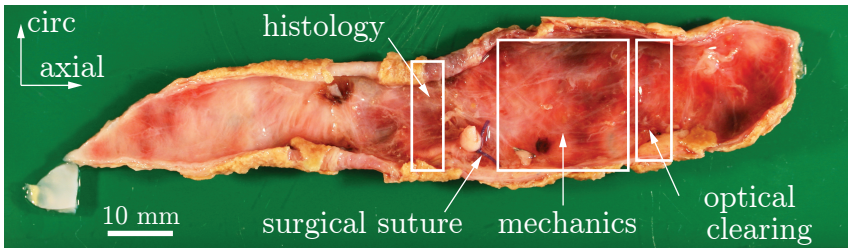

Figure 5.1: Abluminal side of a representative AAA specimen showing the contours of the samples prepared for further testing.

5.2.2 Histology

Arterial segments as indicated in Figure 5.1 were fixed in 4% formaldehyde solution (pH 7.4), embedded in paraffin, sectioned at 3 - 5 μm and stained. To visualize cells hematoxylin and eosin (H&E) staining was used to evaluate the general cell content and architecture of the specimen, as well as for estimation of inflammatory cell content and calcification. Elastica van Gieson (EvG) staining was applied to visualize elastin, collagen and smooth muscle cells.

Additionally, small sections of two unfixed arteries were stained on cry-cut sections with Sudan Red G to confirm lipids inside voids seen within the wall.

5.2.3 Second-harmonic Generation Imaging

The 3-dimensional collagen structure was determined by means of second harmonic generation (SHG) imaging, which was performed on an imaging set-up consisting of a picosecond laser source and an optical parametric oscillator (OPO; picoEmerald; APE, Germany; HighQ Laser, Austria). These were integrated into a Leica SP5 confocal micorscope (Leica Microsystems Inc., Austria). The excitation wavelength was tuned to 880 nm and the detection of the signal was achieved using a BP 465/170 emission filter. 3-dimensional image stacks (z-stacks, 3 μm steps and cross-section images in $(x,y$-plane) were acquired using a Leica HCX IRAPO L 25×0.95 water immersion objective (working distance 2.5 mm for deep tissue imaging).

5.2.4 Mechanical Testing

The samples were mounted into a biaxial testing device using hooks on surgical sutures. Subsequently the samples were submerged in a 0.9% saline solution and heated to $37 \pm 1^{\circ}$. A stretch-driven protocol was used for testing, starting at a deformation of 2.5% and being increased by increments of 0.01 stretch until failure. As AAA tissue is very sensitive to initial preloads, zero strain was defined at a configuration of 0.05 N load. To cover a physiological range of deformations each sample was tested using five different stretch-ratios as follows: $\lambda_{\text{axial}} : \lambda_{\text{circ}} = 1:1$, $1:0.75$, $0.75:1$, $1:0.5$ and $0.5:1$, where λ_{circ} and λ_{axial} denote the stretch in circumferential and axial direction, respectively. The samples were loaded quasi-statically with a rate of $3\,\text{mm}\,\text{min}^{-1}$. Normal and shear deformations were quantified following [203] and shear deformation was found to be negligible.

5.2.5 Material Model

We assume that the aorta can be modeled as a purely elastic, incompressible and fiber-reinforced material. Therefore we introduce the deformation gradient $\mathbf{F}$ and the right Cauchy-Green tensor $\mathbf{C} = \mathbf{F}^{\mathrm{T}}\mathbf{F}$ [173] and define the decoupled strain-energy function Ψ according to [199]

$$\Psi = \Psi_{\text{g}}(\mathbf{C}) + \sum_{i=4,6} \Psi_{\text{f}i}(\mathbf{C}, \mathbf{H}_i) + p\mathbf{I}, \tag{5.1}$$

where Ψ_{g} represents the contribution of the ground matrix, i.e.

$$\Psi_{\text{g}}(\mathbf{C}) = \frac{c}{2}(I_1 - 3). \tag{5.2}$$

Here, I_1 is the first invariant, defined as $I_1 = \text{tr}\mathbf{C}$ and c is a material parameter, describing the stiffness of the ground matrix.

$\Psi_{\mathrm{f}i}$ represents the contribution of the two fiber families, which is defined by the two in-plane mean fiber directions, i.e.

$$\mathbf{M}_4 = \cos\alpha\mathbf{e}_1 + \sin\alpha\mathbf{e}_2, \qquad \mathbf{M}_6 = \cos\alpha\mathbf{e}_1 - \sin\alpha\mathbf{e}_2, \tag{5.3}$$

where the fiber directions $\mathbf{M}_4$ and $\mathbf{M}_6$ make an angle α with the circumferential direction $\mathbf{e}_1$. Additionally, the contribution of the fibers depends on the dispersion parameters κ_{ip} and κ_{op}, which are incorporated into the generalized structure tensors $\mathbf{H}_4$ and $\mathbf{H}_6$ as follows:

$$\mathbf{H}_i = A\mathbf{I} + B\mathbf{M}_i \otimes \mathbf{M}_i + (1-3A-B)\mathbf{M}_{\mathrm{n}} \otimes \mathbf{M}_{\mathrm{n}}, \qquad i = 4,6, \tag{5.4}$$

where the constants A and B are

$$A = 2\kappa_{\mathrm{op}}\kappa_{\mathrm{ip}}, \qquad B = 2\kappa_{\mathrm{op}}(1-2\kappa_{\mathrm{ip}}). \tag{5.5}$$

This results in the definition of $\Psi_{\mathrm{f}i}$ as

$$\Psi_{\mathrm{f}i}(\mathbf{C},\mathbf{H}_i) = \frac{k_1}{2k_2}\left\{\exp\left[k_2(I_i^\star - 1)^2\right] - 1\right\}, \qquad i = 4,6, \tag{5.6}$$

with the stress-like parameter $k_1 > 0$, the dimensionless parameter $k_2 > 0$ and the generalized invariants $I_i^\star$, defined as

$$I_i^\star = \mathrm{tr}(\mathbf{H}_i\mathbf{C}) = AI_1 + BI_i + (1-3A-B)I_{\mathrm{n}}, \qquad i = 4,6. \tag{5.7}$$

Here, the invariants I_4, I_6 and I_{n} are defined according to

$$I_i = \mathbf{C} : \mathbf{M}_i \otimes \mathbf{M}_i, \quad i = 4,6, \qquad I_{\mathrm{n}} = \mathbf{C} : \mathbf{M}_{\mathrm{n}} \otimes \mathbf{M}_{\mathrm{n}}, \tag{5.8}$$

It is worth noting that the material model incorporates three material parameters (c, k_1, k_2), which can be determined by fitting the model to mechanical data (in this study from biaxial tensile tests) and three structural parameters (κ_{ip}, κ_{op}, α), which can be determined by imaging (in this study by SHG imaging).

5.2.6 Data Analsyis

Histological Data

Histological investigation was performed on all samples to measure the wall thickness and the relative thickness of the individual layers in % of the whole wall. All length measurements were done on scanned slides using Aperio ImageScope (Leica Biosystems, Germany). The relative amount of lipids on the luminal and abluminal side in % and the relative amount of calcification in % of all constituents were quantified semiquantitatively by two experienced pathologist. Additionally the relative elastin, smooth muscle cell (SMC) and inflammatory cell contents were quantified.

Microstructural Parameters

Images acquired by SHG imaging were analyzed by extracting data from $z-$stacks (three-dimensional images). Fourier power spectrum analysis and wedge filtering as described in [177] were utilized to gain discrete angular distributions of relative amplitudes, resembling the fiber orientation. The fiber orientation was defined in the same manner as introduced in [199, 211], see e.g. Fig. 2 in [211]. The underlying coordinate system was defined by the unit vectors $\mathbf{e}_1$, $\mathbf{e}_2$ and $\mathbf{e}_3$, representing the circumferential, axial and radial direction, respectively. The general fiber direction in the (unloaded) reference configuration $\mathbf{N}$ was defined by the two angles $\Theta \in [0, 2\pi]$ (resembling the in-plane angle) and $\Phi \in [-\pi/2, \pi/2]$ (corresponding to the out-of-plane angle). Following [211] the in-plane and out-of-plane dispersions were fitted assuming their independence [19] with a bivariate von Mises distribution $\rho(\Theta, \Phi) = \rho_{\text{ip}}(\Phi)\rho_{\text{op}}(\Theta)$ defined as follows [199]:

$$\rho_{\text{ip}}(\Phi) = \frac{\exp[a\cos 2(\Phi \pm \alpha)]}{I_0(a)}, \qquad \rho_{\text{op}}(\Theta) = 2\sqrt{\frac{2b}{\pi}}\frac{\exp[b(\cos 2\Theta - 1)]}{\text{erf}(\sqrt{2b})}, \tag{5.9}$$

where a and b are fitting parameters defining the shape of the distributions, α is the angle between the circumferential direction $\mathbf{e}_1$ and $I_0(a)$ is the modified Bessel function of the first kind of order 0.

Following [199] two scalar quantities were introduced to measure the in-plane (κ_{ip}) and out-of-plane (κ_{op}) dispersions by

$$\kappa_{\text{ip}} = \frac{1}{2} - \frac{I_1(a)}{2I_0(a)}, \qquad \kappa_{\text{op}} = \frac{1}{2} - \frac{1}{8b} + \frac{1}{4}\sqrt{\frac{2}{\pi b}}\frac{\exp(-2b)}{\text{erf}(\sqrt{2b})}, \tag{5.10}$$

where $0 \leq \kappa_{\text{ip}} \leq 1$ and $0 \leq \kappa_{\text{op}} \leq 1/2$. A value of $\kappa_{\text{ip}} = 0.5$ corresponds to an isotropic fiber dispersion in-plane, whereas $\kappa_{\text{ip}} = 0$ resembles perfect alignment. For $\kappa_{\text{op}} = 0.5$ all fibers lie in-plane, whereas $\kappa_{\text{ip}} = 1/3$ corresponds to all fibers being dispersed out-of-plane.

Mechanical Parameters

The model was fitted to all five testing ratios (1:1, 1:0.75, 1:0.5, 0.75:1, 0.5:1) in both axial and circumferential direction simultaneously, utilizing the optimization toolbox `lsqnonlin` in Matlab (The MathWorks, Inc., MA, USA). The structural parameters κ_{ip}, κ_{op} and α were determined as described in section 5.2.6 and used for fitting the material model to the biaxial experimental data. Hence, the only three fitting parameters were c, k_1 and k_2. The goodness of fit was evaluated by the coefficient of determination R^2.

Inflection Points

To compare the points of all stress-strain curves where the collagen takes over the mechanical response and hence the material stiffens rapidly, an 'inflection point' was defined. As mostly the circumferential direction behaved slightly stiffer, the inflection point was defined as the maximal change of slope of the circumferential 1:1 curve and calculated in Matlab.

For further analysis three distinct stages were defined: Stage 1 exhibiting an inflection stretch in circumferential direction in a range of a healthy aortic wall, i.e. $1.10 \leq \lambda < 1.15$, stage 2 to having a circumferential inflection stretch in the range of $\lambda \geq 1.15$ and stage 3 exhibiting an inflection stretch $\lambda < 1.10$. The sample size of the groups was 6 for stage 1, 4 for stage 2 and 5 for stage 3.

Statistics

All values are reported in medians and interquartile ranges (iqr), as a normal distribution could not be assumed due to the small sample cohort and outliers would affect the mean and standard deviation.

As we could not assume a normal distribution we used the Spearman's rank correlation to test for possible correlations between two independent data sets. Additionally, the Mann-Whitney U-test was utilized to test for significant differences between data sets. Differences were considered statistically significant if the p-values for both tests were less than 0.05. All statistical analysis was performed using Matlab.

5.3 Results

5.3.1 Study Population

All 15 samples were successfully analyzed for structural, mechanical and histological data. Table 5.1 gives a summary over all (potentially) relevant patient information. All aneurysms exhibited a maximum diameter of more than 55 mm, which is the size where a surgery is commonly advocated for men (50 mm for women, or if the growth exceeds $5-10$ mm per year) [85, 180, 204]. Also, all AAA walls were covered by thrombus and did not come from a ruptured aneurysm. As statin intake might have an impact on adipocytes, we included the information about it as well.

Figure 5.2 shows mechanical responses at a stretch ratio of $1:1$ for all AAA and one healthy control sample.

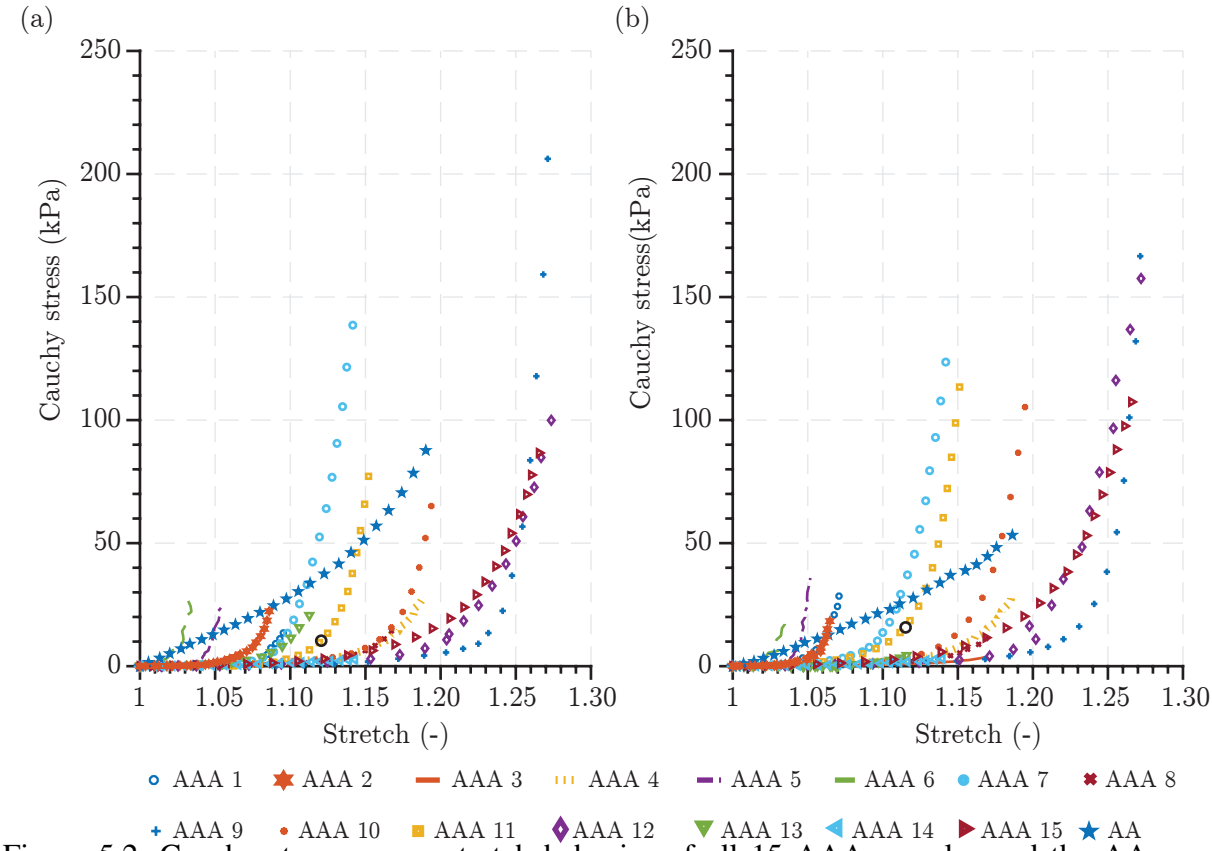

Figure 5.2: Cauchy stress versus stretch behavior of all 15 AAA samples and the AA control obtained by equibiaxial mechanical tests: (a) circumferential, (b) axial direction. The black circle indicates the exemplary inflection point of sample AAA 11.

5.3.2 Healthy Control

The healthy sample exhibited a circumferential inflection stretch of $\lambda = 1.12$, which is consistent with the study cohort in [211]. In healthy abdominal aortas three layers are present with a mean ratio of 20 : 49 : 31 (intima:media:adventitia) [177, 211]. The SMC of the control sample was 35%, whereas the elastin content was 20%, both lying in the range of reported contents [15]. The mean fiber direction of healthy abdominal has a median (iqr) of $\alpha = 24.46^{\circ}$(22.45 to 30.18), showing very little dispersion out-of-plane (median (iqr) $\kappa_{op} = 0.479\,(0.473$ to $0.482)$), as reported in [211].

Figure 5.3 shows micrographs of the same sample location of a healthy abdominal aorta, stained with (a) EvG and (b) H&E. The internal and external elastic lamina, thick elastin bundles and SMC are clearly distinguishable. Outside the adventitia loose connective tissue with a few adhering adipocytes can be seen.

The mechanical parameters as reported in [211] were the following (reported in median

Table 5.1: Patient information of all tested AAA specimen: the ID, age, gender (f: female, m: male), maximum diameter D, smoker, pack years, hypertension, diameters, statin intake, body mass index (BMI), - no information available

#	Age (years)	Gender	D (mm)	Smoker y/n	Pack Years	Hyper-tension	Diabetes y/n	Statin y/n	BMI
1	78	m	56	n	-	y	n	y	24.91
2	62	m	105	n	-	y	n	n	24.97
3	76	m	60	n	-	y	y	y	25.51
4	78	m	72	n	-	y	n	n	27.76
5	68	m	90	y	20	y	n	y	28.67
6	68	m	58	y	20	y	n	y	25.93
7	66	f	65	y	62.5	y	y	y	30.12
8	62	m	72	y	90	-	y	-	-
9	69	m	57	y	55	y	n	n	28.41
10	75	m	77	y	50	y	y	y	23.62
11	84	m	66	n	-	y	y	y	25.4
12	63	m	60	y	35	y	y	n	31.01
13	73	m	64	y	-	y	y	n	21.78
14	63	m	87	y	-	n	n	n	25.26
15	80	f	55	n	-	y	y	n	25.39

(iqr)): $c = 11.59$ kPa (4.13 kPa to 19.93 kPa), $k_1 = 2.66$ kPa (1.15 kPa to 11.64 kPa) and $k_2 = 19.25$ (9.93 to 26.06). The c-value indicates a pronounced initial stiffening, see the star-shaped curve in Figure 5.2.

5.3.3 Inflection Point Related Groups

Levels of disease progression were defined in three stages, depending on their 'inflection' points as described in Chapter 5.2.6, as follows:

$$\text{Stage1} : 1.10 \leq \lambda < 1.15, \;\; \text{Stage2} : \lambda \geq 1.15, \;\; \text{Stage3} : \lambda < 1.10.$$

The choice of groups was confirmed by significant differences in both circumferential and axial strains and stretches between all three groups ($p \leq 0.01$ for all cases).

Table 5.2: 21 parameters obtained by mechanical, structural and histological analysis of all AAA samples. Adv.: Adventitia, Throm: thrombotic material, LL: luminal lipid deposits, Calc: calcification, Inflam.: inflammatory cells, BMI: body mass index, inflection points in circumferential direction.

		Mechanical Parameters			Structural Parameters		
		c (kPa)	$k1$ (kPa)	$k2$ (-)	κ_{ip}(-)	κ_{op} (-)	α ($^\circ$)
Stage 1	median	0.59	1.30	47.51	0.242	0.433	6,55
n = 6	[Q1;Q3]	[0.38; 3.96]	[0.48;2.21]	[24.92;60.41]	[0.234;0.260]	[0.425; 0.441]	[5.19; 11.62]
Stage 2	median	1.83	0.46	17.79	0.224	0.455	33.11
n = 3	[Q1;Q3]	[1,55; 2.54]	[0.40;1.88]	[15.67; 30.83]	[0.219; 0.232]	[0.433; 0.463]	[23.63; 33.62]
Stage 3	median	3.78	8.96	636.29	0.224	0.402	22.90
n = 6	[Q1;Q3]	[0.78; 6.77]	[2.61; 18.27]	[161.29; 2142.10]	[0.191; 0.236]	[0.379; 0.421]	[18.41; 47.02]

		Histological Parameters					
		Intima (%)	Media (%)	Adv. (%)	Neo-Adv. (%)	Layers (-)	Throm. (%)
Stage 1	median	46.37	17.09	30.78	0.00	3	2.5
n = 6	[Q1;Q3]	[32.31; 50.39]	[9.03; 24.25]	[19.04; 37.86]	[0.00; 11.86]	[3; 3]	[0; 8.75]
Stage 2	median	48.00	18.03	18.81	17.57	3	0
n = 3	[Q1;Q3]	[24.00; 48.67]	[9.01; 21.81]	[16.94; 22.60]	[8.78; 49.38]	[2;3]	[0.00; 7.50]
Stage 3	median	0.00	0.00	33.78	66.22	1,00	0
n = 6	[Q1;Q3]	[0.00;0.00]	[0.00;0.00]	[26.10; 40.96]	[57.05; 73.29]	[1;1]	[0.00; 1.50]

		Histological Parameters					
		LL (%)	Calc. (%)	Elastin (%)	SMC (%)	Collagen (%)	Inflam (%)
Stage 1	median	0	0	3.00	3.5	60	2.5
n = 6	[Q1;Q3]	[0.00; 7.50]	[0; 1.50]	[0.25; 5.00]	[1.25; 5.00]	[57.00; 61.50]	[0.00; 12.50]
Stage 2	median	2	15	1	1	60	2
n = 3	[Q1;Q3]	[1.00; 11.00]	[7.50; 17.50]	[0.50; 3.00]	[0.50; 3.00]	[54.50; 63.00]	[2.00;6.00]
Stage 3	median	0	0	0.05	0	45	5
n = 6	[Q1;Q3]	[0.00;0.00]	[0.00; 7.50]	[0.00; 0.78]	[0;0]	[41.25; 75.00]	[1.25; 8.75]

		Inflection Points			
		Diameter (mm)	BMI (-)	λ_{IP} (-)	σ_{IP} (kPa)
Stage 1	median	72	25.26	1.12	2.89
n = 6	[Q1;Q3]	[67.50; 75.75]	[23.62; 25.40]	[1.11; 1.14]	[2.38; 7.52]
Stage 2	median	57.00	28.41	1.2	17.38
n = 3	[Q1;Q3]	[56.00;58.50]	[26.90; 29.71]	[1.20; 1.22]	[14.06; 19.93]
Stage 3	median	62.5	25.72	1.05	1.4
n = 6	[Q1;Q3]	[58.5; 83.75]	[25.11; 27.99]	[1.03; 1.06]	[1.19; 5.78]

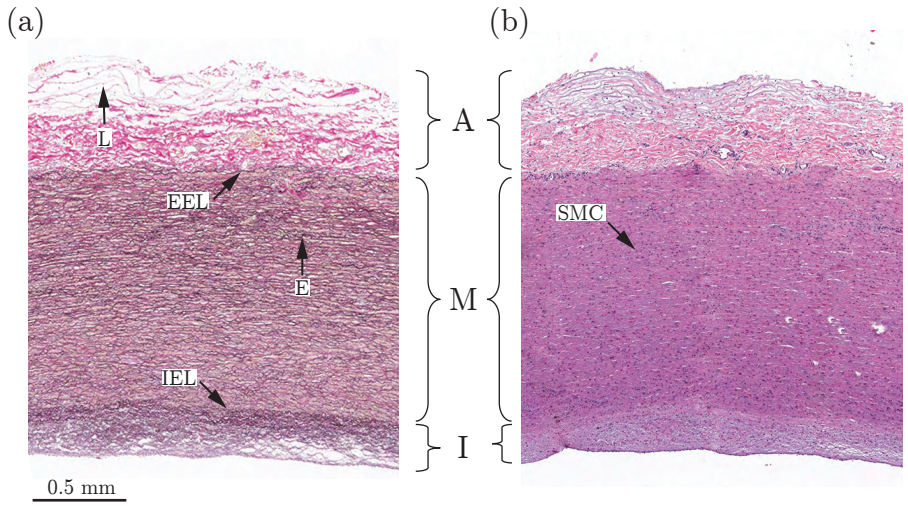

Figure 5.3: Micrographs of the same location of the healthy control sample stained with (a) EvG and (b) H&E. The three characteristic layers of the abdominal aortic wall (I: intima, M: media, A: adventitia) can be seen clearly. The EvG stain reveals the internal elastic lamina (IEL), external elastic lamina (EEL), thick elastin bundles in brown (E) and collagen fibers in pink. Aidpocytes (L) are visible on the outer side of the adventitia. In the H&E stain cells such as smooth muscle cells (SMC) can clearly be seen in dark violet. In the outer part of the adventitia adipocytes from the surrounding fat tissue can be seen.

Stage 1

The circumferential inflection stretch for stage 1 samples exhibited a median (iqr) or 1.12 (1.10 to 1.14). In all samples, three layers were present. However, the intima was thickened, resulting in a ratio between the layers of 40 : 30 : 30. The elastin content decreased drastically to a median (iqr) of 3% (0.25 to 5)% as did the SMC content to a median of 3.5 (1.25 to 5)%.

A micrograph showing a AAA wall in stage 1 is shown in Figure 5.4. The intima is notably thickened and neither IEL nor EEL are distinguishable anymore. Only a few elastic fibers (E) are visible in the middle of the wall, as well as SMCs. A small area with inflammatory cells (IF) is present in the surrounding adipose tissue. Worth of note a the following normal structures: a nerve (N) is visible inside the transition from the adventitia towards the loose connective tissue surrounding the vessel. Inside this loose tissue adipocytes (L) are also visible.

Figure 5.7 shows representative intensity plots for each of the three stages. The left side shows the plot for stage 1, showing fibers being closely dispersed around the circumferential direction throughout the thickness. Indeed, the mean fiber angle for stage

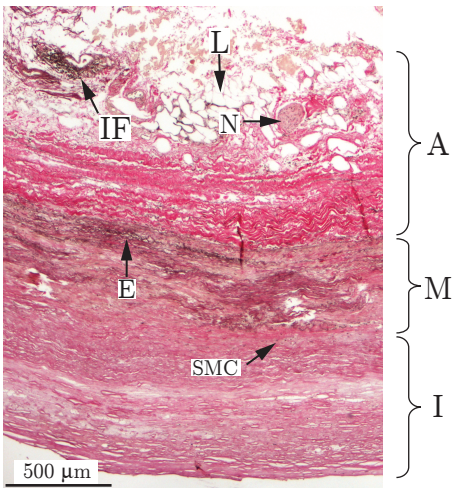

Figure 5.4: EvG stained micrograph showing a AAA wall in stage 1. All three layers are visible. However, the intima (I) is significantly thickened in comparison to the healthy sample. Also the IEL and EEL are not clearly distinguishable anymore. A nerve (N) is visible on the outer part of the wall, as well as adipocytes (L) in the outer part of the adventitia (A). The media (M) contains notably less elastin fibers (E) and smooth muscle cells (SMC) in comparison to the healthy sample. Also inflammatory cells (IF) are visible in the adventitia.

1 is significantly smaller compared to healthy samples ($p < 0.001$) with a median (iqr) of 6.55° (5.19° to 11.62°). The out-of-plane dispersion increased to a value of $\kappa_{op} = 0.43$ (0.42 to 0.44), and the stiffness parameter k_2 increased with a factor 2 compared to the healthy aorta to a median (iqr) of 47.51 (24.92 to 60.41). Especially the initial stiffness decreased significantly compared to the healthy aorta to $c = 0.59$ kPa (0.38 to 3.96 kPa), see also Figure 5.2.

Stage 2

The inflection stretch in circumferential direction showed a median (iqr) of 1.20 (1.20 to1.22). In two samples only the adventitia was the only remaining wall part, whereas one exhibited two layers and one still all three. The elastin and SMC contents decreased to 1%, and the adipocytes lying inside the wall (see Figure 5.5) increased to 8.87% (4.39% to 13.17%) in comparison to no adipocytes present inside the wall in stage 1 or the healthy sample. Inflammation was visible on the abluminal side of the wall (IF), co-localizing with disrupted adipocytes (DL). Above the abluminal lipids, especially at places showing inflammation, see Figure 5.5, new collagen started to build up, forming a neo-adventitia (NA)

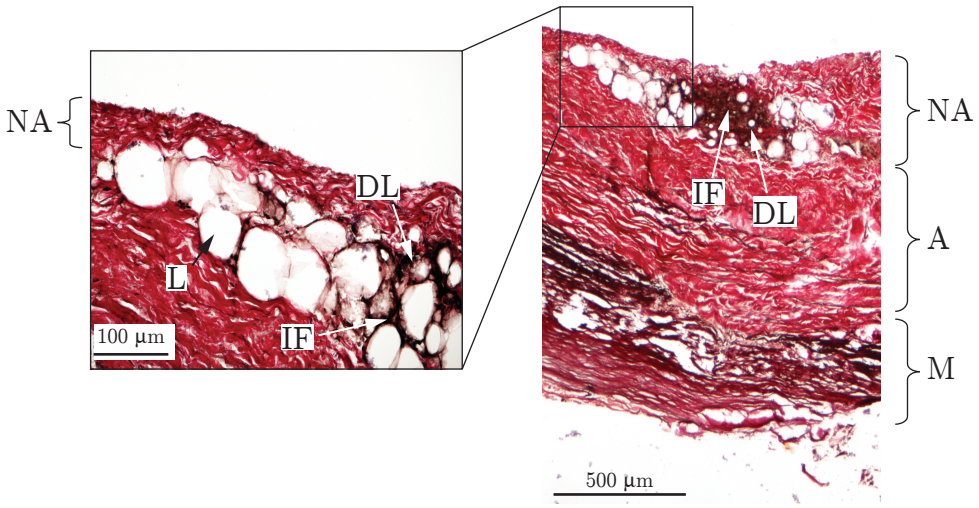

Figure 5.5: EvG stained micrograph showing a AAA wall in stage 2. No intima, elastin or SMC are visible. The transition between media and adventitia is not clear. Inflammation (IF) is visible, located around disrupted adipocytes (DL). Non-disrupted adipocytes (L) are covered by apparently newly deposited collagen, the neo-adventitia (NA).

(17.57% (8.78% to 49.38%) of the whole wall thickness). No such layer was seen in neither stage 1 nor the healthy sample.

The middle image in Figure 5.7 shows a representative plot for stage 2. Similar to stage 1, the fibers for the first 600 μm are aligned closely around the circumferential direction. However, the collagen fibers are isotropically dispersed further on, resulting in a median (iqr) angle of 33.11° (23.63° to 33.62°), being significantly bigger compared to stage 1 ($p = 0.02$).

Stage 3

The circumferential inflection stretch for samples in stage 3 had a median (iqr) of 1.05 (1.03 to1.06). In all samples of stage 3 only one layer could be seen except of one sample where media and adventitia were present. Hence, the amount of intima and media in stage 3 was significantly lower compared to stages 1 and 2. SMC and elastin content were once more significantly decreased in comparison to stage 2 to 0% for all samples ($p = 0.01$). A significantly thickened neo-adventitia was present in the third stage with a median (iqr) of 66.22% (57.05% to 73.29%) of the wall ($p = 0.02$ to stage 1 but only $p = 0.08$ to stage 2).

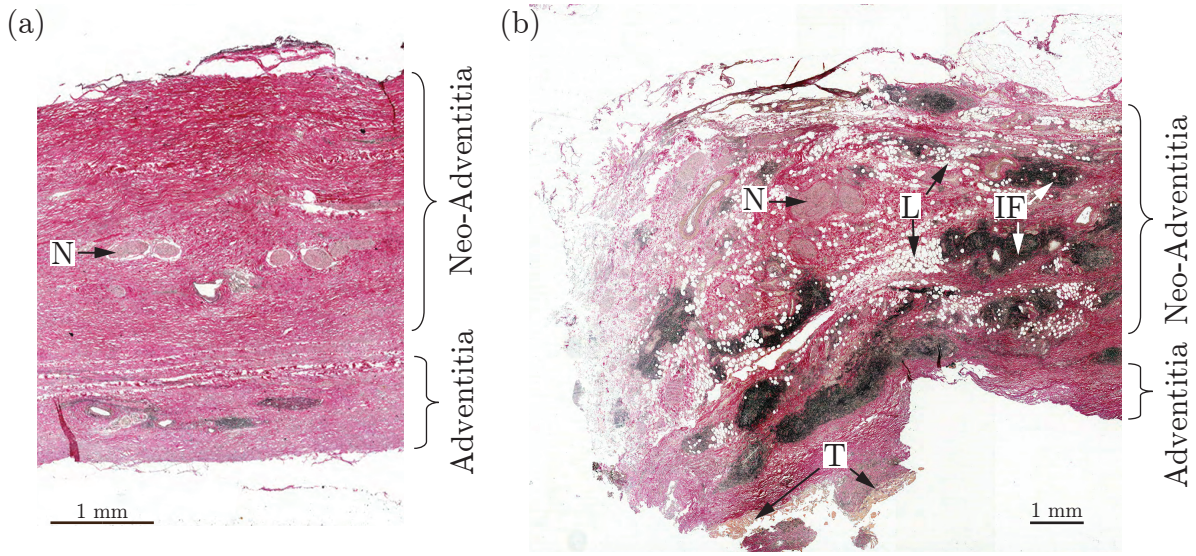

Figure 5.6: EvG stained micrographs showing (a) a "safely" remodeled AAA wall and (b) a potentially vulnerable AAA wall in stage 3. Both samples show a significant neo-adventita and neither media nor intima, the bottom denotes the luminal side. Nerves (N) appear entrapped within the wall in both samples, significant amounts of inflammation (IF), remnants of thrombotic material on the luminal side (T) and adipocyte cells (L) can be seen in (b).

Looking at the mechanical response, the third stage exhibited the stiffest behavior with a k_2 parameter of 636.29 (161.29 to 2142.10) ($p = 0.01$ compared to both stage 1 and 2). Also k_1 was significantly higher in comparison to stage 1 ($p = 0.05$) and slightly higher compared to stage 2 ($p = 0.09$) $k_1 = 8.96$ kPa (2.61 to 18.27 kPa).

The right image in Figure 5.7 shows a representative intensity plot for stage 3. Similar to stage 2, the luminal side shows fibers dispersed towards the circumferential direction, followed by an isotropic fiber dispersion which is more pronounced compared to stage 2. The out-of-plane dispersion was slightly higher compared to stage 1 ($p = 0.08$) with $\kappa_{op} = 0.402$ (0.379 to 0.412)

Figure 5.6 shows two kinds of stage 3 walls. The left wall in (a) shows the remains of adventitia, followed by a dense collagen layer forming a neo-adventitia. The nerves (N) lie now inside the wall, emphasizing the thickness of the newly formed collagen. No inflammation can be seen on the abluminal side anymore, and no adipocytes can be seen anymore. The right micrograph shows another kind of stage 3 wall: significant amounts of inflammation (IF) are visible throughout the wall, co-localizing with significant amounts

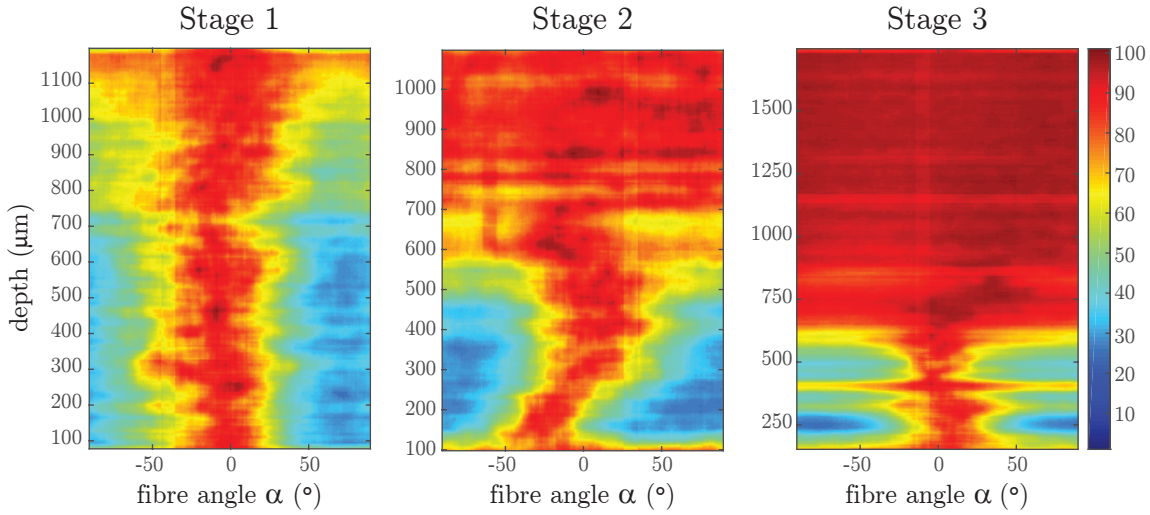

Figure 5.7: Representative intensity plots for all three stages, showing the collagen fiber orientation and distribution through the depth of the aortic wall. A depth of 0 denotes the luminal side. Stage 1 shows fibers oriented closely towards the circumferential direction throughout the thickness of the wall. Stage 2 exhibits a similar fiber dispersion until a depth of around 600 μm, followed by an isotropic fiber dispersion. Stage 3 shows the same tendency. However, the isotropic fiber distribution starts earlier and continues for over 1000 μm.

of adipocytes (L). Again, a nerve (N) is entrapped in the middle of the wall, underlining the newly formed tissue on the abluminal side.

It is worth noting, that all patients except one took statins in stage 3, whereas no patient in stage 2 took these drugs. Two out of 6 patients in stage 1 took statins.

5.3.4 Statistical Analysis Regardless of Inflection Points

In total, 22 parameters were gained by histological, microstructural and mechanical analysis. All these parameters were examined for correlations where reasonable. A correlation was assumed significant when $p-$values were below 0.05. In total, 13 significant correlations could be found, as shown in Table 5.3. Additionally, 6 pairs were found to show a tendency towards correlation (defined by a $p-$value > 0.05 and < 0.09), and were chosen to be shown here since correlation might motivate subsequent studies with a larger study cohort, see Table 5.4.

Figure 5.9 shows two exemplary correlations: SMC content and the percentage of newly built neo-adventitia correlate significantly, showing less SMC content in arteries with a

Table 5.3: All significant correlations with corresponding $p-$ and $r-$values found in this study. IP: 'inflection' point, LL: luminal lipid deposits, BMI: body mass index, intima %, media %, adventitia % and neo-adventitia % correspond to the percentage of the individual layer relative to the whole wall thickness.

Correlated variables	$p-$value	$r-$value
κ_{op} and k_2	0.000	0.79
IP λ_{circ} and k_2	0.022	-0.59
IP λ_{circ} and intima %	0.042	0.53
α and neo-adventitia %	0.050	0.51
Intima % and elastin	0.049	0.52
Intima % and SMC	0.000	0.88
Media % and LL	0.030	0.56
Media % and elastin	0.001	0.77
Media % and SMC	0.000	0.92
Adventitia % and diameter	0.043	-0.53
Neo-adventitia % and SMC	0.003	-0.72
Neo-adventitia % and # layers	0.006	-0.68
Diameter and inflammation	0.018	0.60
BMI and LL	0.009	0.64

Table 5.4: Pairs of parameters showing a tendency towards correlation. IP: 'inflection point', media %, adventitia % and neo-adventitia % correspond to the percentage of the individual layer relative to the whole wall thickness.

	$p-$value	$r-$value
κ_{op} and IP λ_{ax}	0.080	0.47
IP λ_{circ} and media %	0.085	0.46
IP λ_{circ} and SMC	0.077	0.47
IP λ_{circ} and # layers	0.065	0.49
Intima % and Calcification	0.066	-0.65
Diameter and Calcification	0.086	-0.46

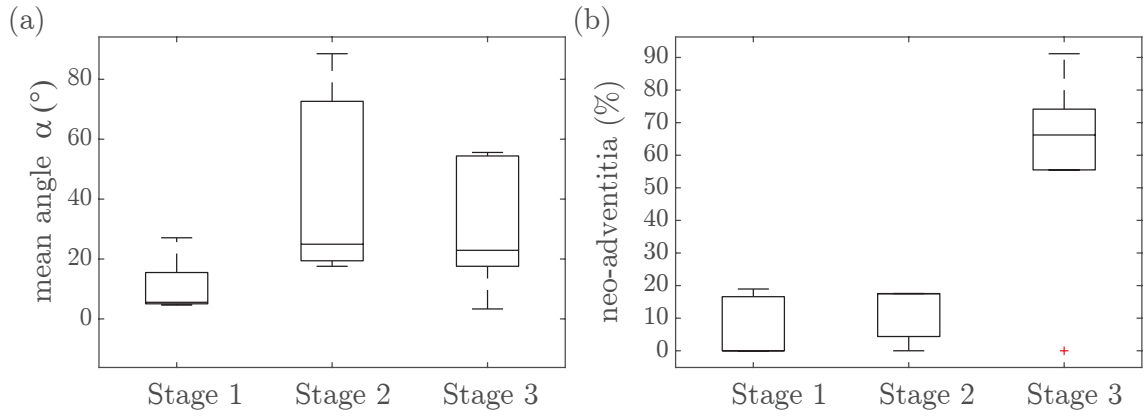

Figure 5.8: Box-and-whisker plots of (a) the mean angle α and (b) the percentage of neo-adventitia of the whole wall for all three stages.

thicker neo-adventitia. The dimensionless stiffness parameter k_2 is very high for low 'inflection'points and falls rapidly for higher 'inflection'points. Figure 5.10 shows an exemplary box-and-whisker plot of the amount of neo-adventitia in % of the whole wall in samples which exhibited one, two or all three layers. It is clearly visible that the amount of neo-adventitia significantly increases with decreasing layers in the AAA wall.

Additionally to the grouping in inflection point groups, the samples were also grouped (yes/no) to examine the possible effects of diabetes and statin intake on the examined parameters. Patients with diabetes exhibited a significantly lower initial stiffness ($c = 1.16\,\text{kPa}\ (0.34\,\text{to}\,1.82)$ kPa) compared to patients without diabetes ($c = 6.56$ kPa $(2.11$ to $6.83)$ kPa, $p = 0.04$). Interestingly, the stiffness parameter k_2 was significantly higher in patients without diabetes ($k_2 = 636.29\ (210.00$ to $2142.10)$) than in patients with diabetes ($k_2 = 43.86\ (17.79$ to $48.75)$, $p = 0.007$).

5.4 Discussion

Several correlations were found, which in the end enabled a definition of three stages of disease progression. For instance, the 'inflection point' strain was significantly correlated with the stiffness parameter k_2, showing a significantly stiffer behavior with earlier collagen fiber recruitment. The parameter k_2 was also significantly correlated with the out-of-plane dispersion parameter κ_{op}, indicating a higher out-of-plane orientation with increased stiffness and hence with disease progression. As the integrity of the AAA wall is lost when the ECM is degraded, collagen fibers are less aligned in-plane, consistent with our earlier study [211].

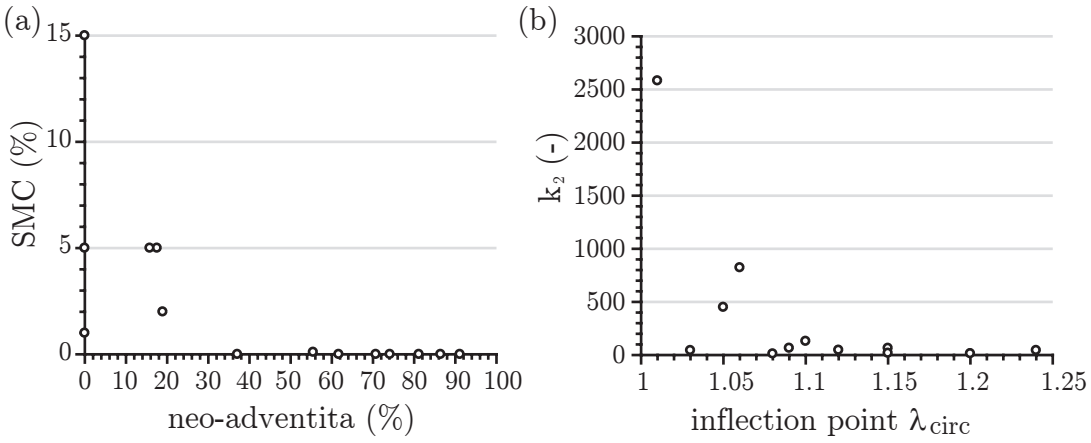

Figure 5.9: Exemplary plots of significant correlation of (a) SMC content and % of neo-adventitia of the wall and (b) the mechanical parameter k_2 and the strain of the circumferential 'inflection' point. SMC content decreases significantly with a growing percentage of neo-adventitia. The stiffness parameter k_2 increases significantly with a decreasing 'inflection' point strain in circumferential direction. The highest value of $k_2 = 7403.3$ at an 'inflection' point strain of $\lambda_{\text{circ}} = 1.04$ was not plotted here for clarity of lower values of k_2.

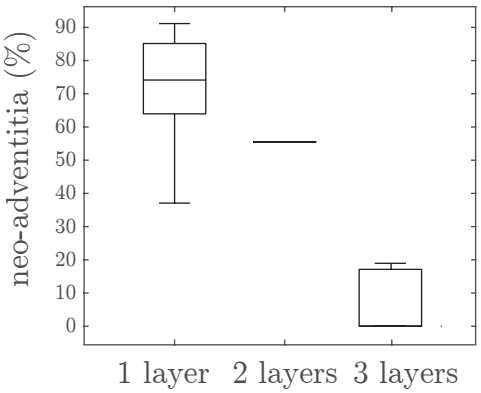

Figure 5.10: Box-and-whisker plot of the percentage of neo-adventitia of the whole wall for samples with 1, 2 or all three layers present.

The mean collagen angle α, and the amount of SMC and elastin correlated positively with the relative thickness of neo-adventitia, indicating the neo-adventitia as a marker of disease progression, as did the relative thicknesses of intima and media, which correlated significantly with elastin and SMC contents.

The only significant correlation with the diameter was found with the amount of inflammation, confirming findings by [242].

5.4.1 Hypothesis of a Mechano-pathogenic Model in Three Stages

Figure 5.11 shows a flowchart depicting our hypothesis of disease progression, derived from observed changes in mechanics, histology and structure (collagen architecture).

The chart starts with the behavior of a healthy aorta. Mechanically, the artery shows a significant initial stiffness (see also Fig. 5.2, sample AA) (median (iqr) $c_{\mathrm{AA}} = 33.86$ (6.88 to 98.76) kPa), and once it stiffens, the slope is moderate ($k_{2\mathrm{AA}} = 19.25$ (9.93 to 26.06)) [211].

Looking at the histology, we can see a thin intima, a clear membrana elastica interna, and a clear membrana elastica externa, seperating intima from media and media from adventitia, respectively. The media incorporates collagen and elastin fibers, and has a significant amount of SMCs. The adventitia exhibits a thicker, wavier type of collagen than the media, and nerves and adipocytes are visible on the outer side of the wall.

The collagen structure is depicted in the intensity plot, taken from [211], showing an isotropic intima (starting from the bottom), followed by two counter-rotating fiber families throughout the media and finally two fiber families pointing towards the axial direction in the adventitia.

Stage 1

It has been shown in several studies [79, 243–245] that a degradation of the extracellular matrix occurs, accompanied by a degradation of elastin and SMCs [246] (see Table 5.2). (For a theory of the initiation of aneurysm formation, see, e.g. [234, 243]). As the elasticity of elastin is lost, an aneurysm starts to form [243]. Following the bulging, and due to lack of cells which might deposit new collagen, collagen fibers reorient passively towards the circumferential direction ($\alpha_{\mathrm{Stage1}} = 6.55^{\circ}$ (5.19 to 11.62)$^{\circ}$).

This is clearly visible in the intensity plot of stage 1 - all fibers are oriented closely towards the circumferential direction throughout the wall thickness. The point where collagen fibers get recruited is around the same stretch as in healthy samples. However, the initial stiffness decreases rapidly ($c_{\mathrm{Stage1}} = 0.59$ (0.38 to 3.96) kPa), see, e.g. Figure 5.2, sample AAA11. The slope, once collagen gets recruited, is more pronounced, increasing to a value of ($k_{2\mathrm{Stage1}} = 47.51$ (24.92 to 60.41)).

The intima starts to thicken, but most severely a significant loss in elastin and SMC content can be noted. As this leads to a loss of the membrana elastica interna and externa, a clear distinction between layers becomes difficult (see also Figure 5.4). Adipocytes and nerves are still located on the outer side of the wall, embedded in loose connective tissue.

We hypothesize that the growing aneurysm presses against the surrounding tissue, and hence compresses the perivascular adipose tissue, or ‘tunica adiposa’ [241]. Due to the

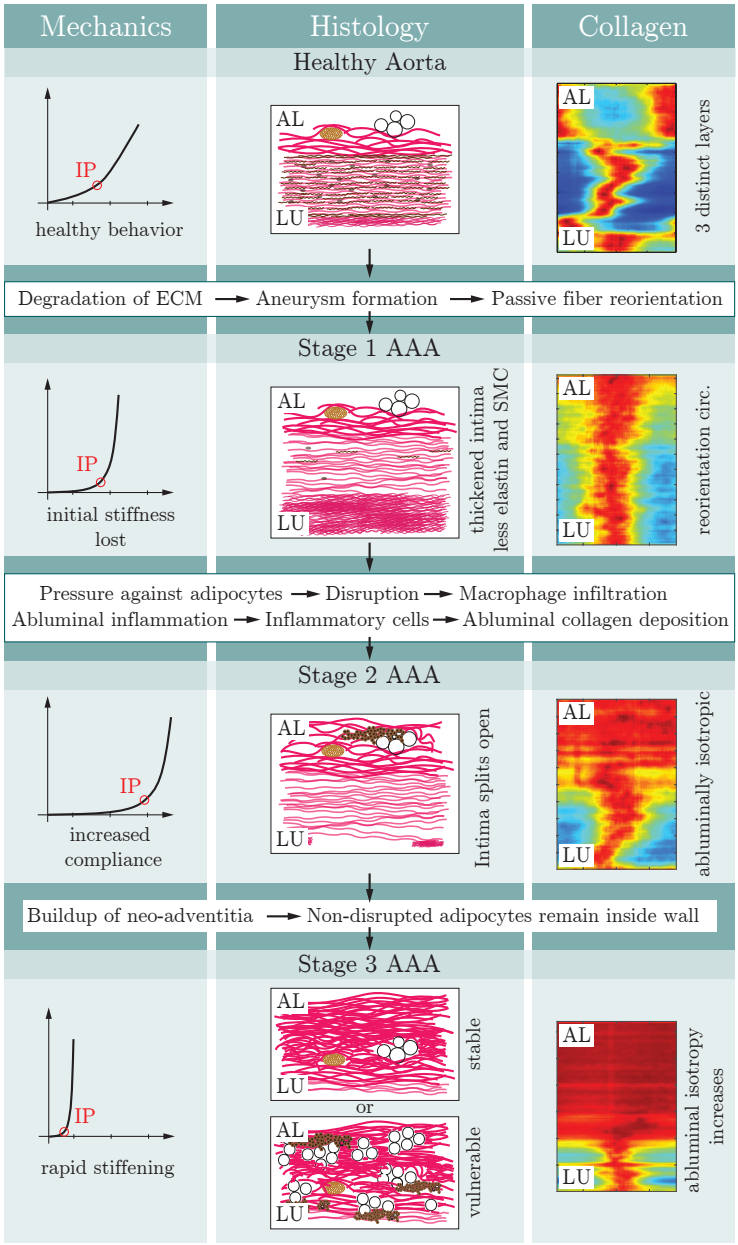

Figure 5.11: Flow chart summarizing the disease progression steps. It is divided into mechanics, histology and collagen, where changes are illustrated between the healthy aorta and three disease stages of AAAs. The mechanics are illustrated as a stress-strain curve, showing an idealized mechanical behavior for the respective case and the inflection point IP as a red circle. Changes in histology are depicted schematically and color coded as follows: light pink depicts collagen fibers,brown wavy structures symbolize elastin and brown circles SMCs, black and white circles are adipocytes, brown circles filled with black are inflammatory cells, and yellow ovals are nerves. The third part of the flow chart, labelled 'Collagen' shows exemplary intensity plots as explained in Figure 5.7.

pressure force, adipocytes undergo in part necrosis or apoptosis and the evading lipids are taken over by macrophages. This is a starting point for inflammation which accumulates inflammatory cells and fibroblasts, which further leads to the production of collagen fibers comparable to scar formation.

Briton and Fox [21] state that perivascular adipose tissue might be linked to vascular disease, as adipocytes might contribute with a local toxic effect by migration of immune cells into the vascular wall. This might promote inflammation there, as obesity is associated with changes in adipokine secretion. Hence, the local pathogenic effect of a 'tunica adiposa'may be either direct by compression of the vessels or indirect by changes in fat tissue itself with diseases such as obesity [247, 248]. Although the effect of perivascular fat remains incompletely understood, the mechanisms seem to include a direct effect on the vasculature such as the stimulation of immune cell migration into the vascular lumen [21].

Stage 2

We observed inflammation co-localizing with adipocytes in stage 2, which was not observed in healthy arteries or stage 1 AAAs. These inflammatory cells together with fibroblasts have the ability to deposit collagen [249]. As these cells are the only vital appearing cells we could localize in the AAA walls, we hypothesize that all collagen deposition is due to this inflammatory process on the abluminal side of the aorta. This theory is supported by the fact that a significant isotropically distributed layer is visible in the intensity plots of collagen orientation, which follows fibers closely oriented towards the circumferential direction. As the aneurysms grows, stresses in the axial direction increase and hence an isotropic fiber orientation of collagen appears, as also hypothesized in [188, 250]. Also, adipocytes and nerve cells covered by dense collagen fibers are already visible in micrographs of stage 2 AAA walls, see Figure 5.5. We call this new deposition of collagen at the outer side of the AAA 'neo-adventitia', (NA). Statistically significant differences in the mean fiber angle α and the thickness of the neo-adventitia further support this hypothesis. Studies such as [251] have briefly stated that collagen deposition seems only to happen on the abluminal side, but did not give any explanation for this finding.

In stage 2, the intima seems to burst open, as we could observe in some micrographs. Hence, only the media and adventitia are left, which are not clearly distinguishable anymore. The mechanical behavior becomes very compliant, probably because the stiff intima [184, 211] opens. Newly deposited fibers seem to be quite wavy, although we did not quantify the waviness in this study. This might additionally explain the increased distensibility of the wall: as the integrity of the wall decreases, the collagen fibers can straighten and re-orientate without much resistance and get recruited at a later stage with higher stretches compared to healthy arteries or stage 1 AAA walls (see Table 5.2 and, e.g. Figure 5.2, sample AAA15).

Stage 3

The transition towards stage 3 is associated with a built up of a significant neo-adventitia. Smaller, disrupted adipocytes are cleaned off by macrophages and only non-disrupted adipocytes remain inside the wall. All walls are common in their stiffness (see, e.g., Figure 5.2, sample AAA2) and a significant amount of neo-adventitia. This neo-adventitia is visible in the intensity plot, exhibiting an increased percentage of the wall having an isotropic fiber orientation with a decreasing percentage of the wall showing fibers oriented towards the circumferential direction. Indeed, in most micrographs no media could be seen anymore and only the adventitia with the newly deposited neo-adventitia remained. This also explains why no significant difference in wall thickness could be seen between the samples, despite of new collagen deposition. Apparently, both intima and media split open, as could be observed on some micrographs. However, to further support this latter theory, a study of whole aneurysms is necessary to confirm the circumferential distribution of the three aortic layers, as unfortunately we only had access to a small piece of the AAA walls on the anterior side.

Despite of the common features such as a significant neo-adventitia and no intima nor media present, we could observe two kinds of remodeled stage 3 walls. The first kind seemed to have remodeled 'safely', see Figure 5.6, (a). Almost no adipocytes were present inside the wall, only a thick collagen layer was entrapping nerves, which indicated the new collagen deposition. These samples had a higher relative collagen content compared to the other stages (89% and 85%). The second kind of walls seemed to have remodeled to a 'vulnerable' state, see Figure 5.6 (b). Here, significant amounts of inflammation and adipocytes were visible inside the wall.

Interestingly, we did not see any significant differences in diameter between the groups as this measure seems to be unfit as dependent on too many premises. Monteiro et al. [188] examined failure strains and stresses by uniaxial tensile testing and could not find any correlation between failure strains and diameters either.

5.4.2 Connection with Literature

The potentially important role of adipocytes located inside or adjacent to aneurysm walls has been studied by two groups to the authors knowledge:

Tanaka et al. [239] applied imaging mass spectrometry to analyze the localization of lipid molecules in human aneurysm walls. They found that the size of adipocytes was markedly larger compared to those located in the neck and that the integrity of collagen became disrupted by the infiltration of adipocytes. The group also stated, that high plasma TG levels may be potential risk factors for AAA rupture, however, serum TG levels were not elevated for most of the patients. Their hypothesis was that adipocyte accumulations in

AAA walls may be indicators for an increased rupture risk. However, no hypothesis for the origin of the adipocytes was given.

Kugo et al. [236] performed an animal study with a hyperfusion-induced animal model (developed by the same group and described in [238]) for AAAs and additionally collected 30 human samples from AAA surgeries. They found increased amounts of adipocytes in ruptured vessels compared to non-ruptured walls, but did not state whether the adipocytes were included inside the wall or adjacent to the wall. The adipocyte like cells were located in the adventitial side of the AAA sac, but not in the neck in both ruptured and unruptured groups. Additionally they stated that local inflammation was associated with the observed adipocytes. They concluded that the appropriate control of adipocytes may treat or even prevent AAA rupture.

Ollikainen et al. [240] examined 20 ruptured and 16 unruptured saccular intracranial aneurysms with respect to lipid accumulations. They found that intracellular lipid accumulation was associated with wall remodeling and rupture and that macrophages correlated with these lipid accumulations. Extracellularly accumulated adipophilin was present in higher amounts in ruptured than unruptured walls, which reflected the death of lipid-laden cells, macrophages and SMCs and the release of their intracellular, adipophilin covered lipids droplets into the ECM. The group hypothesized that the lipids may originate from the thrombus or from neo-vessels. However, intracranial aneurysms are not surrounded by perivascular fat and hence the mechanism of lipid accumulation is most likely different to the one in AAAs.

Several studies reported remodeling in the adventitia, such as Maiellaro et al. [252]. They observed significant thickening of the adventitia, accompanied by a recruitment of macrophages. This may highlight an inward progression of inflammation from adventitia towards the luminal side of the AAA wall. However, they also stated that this is most probably not the first trigger for aneurysm dilatation as no inflammation in adventitia was seen in small aneurysms.

The ‘tunica adiposa’ was described by several groups as a potential source of inflammation. For example, Cinti et al. [253] andPolice et al. [242] connected adipocyte death to macrophages inside the adventitia and hence to enhanced AAA formation. Also Chaldakov [241] stated that adipocyte tissue, surrounding vessels, might be connected to cellular infiltration of inflammatory cells and hence play an important factor in an ‘outside-in’ signaling in development of diseases such as atherosclerosis and cardiomyopathy. However, the effects of a ‘tunica adiposa’ around vessels remains incompletely understood and should be examined further [21].

5.4.3 Conclusion

To the authors' knowledge this is the first study systematically comparing and connecting mechanical data from biaxial tensile tests, histological and structural data to define disease stages.

The proposed pathogenesis provides an explanation for contradicting studies stating increased anisotropy, e.g. [103, 107, 109, 110, 112, 227], or isotropy, e.g. [106]. According to our hypothesis, collagen in AAA walls realigns passively towards the circumferential direction in the first disease stage, which results in an anisotropic behavior. Subsequently, triggered by inflammation on the abluminal side of the wall, new collagen is deposited isotropically and hence contributes to a more isotopic behavior. Due to the small sample size no significant differences were found regarding isotropy or anisotropy, but a trend towards a more isotropic behavior with disease progression could be seen and should be investigated in future studies.

Another key observation was that collagen deposition only occurs in conjunction to infiltration of inflammatory cells. Hence our theory is that no fibers are synthesized without inflammation in the wall and therefore no safe remodeling is possible to counteract the lost elasticity due to ECM degeneration. The application of anti-inflammatory drugs might actually be counterproductive and more studies should be employed in this direction, as also stated by [234], referring to a study by Lindemann et al. [254], who reported a rapid AAA development and rupture in a patient on immunosuppressive drugs. Also Monteiro et al. [188] suggested that inflammation is not a marker for rupture, but rather for remodeling.

Finally, the significant occurrence of adipocytes in potentially 'vulnerable' stage 3 AAA walls might point towards the possibility to image adipocytes inside the wall even by conventional *ex vivo* imaging techniques such as ultrasound or MRT.

Unfortunately, our biaxial tensile tests could not determine the final rupture strength of the tested specimen. Future studies should aim at the determination of biaxial failure properties to understand the difference in the wall composition of stage 3 AAAs and whether 'safely' remodeled walls are indeed stronger that 'vulnerable' walls.

As AAAs seem to become first more compliant and then stiffer, monitoring changes in aneurysm distensibility could be a better predictor for rupture that monitoring the change in diameter, as proposed by Wilson et al. [255]. They deduced that a reduction in distensibility of AAA walls over time was associated with a significantly reduced time until rupture, independent of other risk factors.

To fully understand this progression, AAA walls should be examined on the nano-scale as well as closely analyzed for collagen undulation and thickness. The impact of diabetes on mechanics and disease progression should be examined closely in future studies, as we found significant differences in mechanical behavior in diabetes and non-diabetes patients.

Additionally we found differences in statin intake between disease stages, hence the intake of statin should be closely examined in the future, as it may influence the growth of AAA, as suggested by, e.g., [256–258]. However, no significant correlation between statin intake and adipocytes inside the wall or neo-adventitia growth could be found in this study.

Another drawback of our study is of course the small sample size and the limited location from which we gain our samples. Due to patient safety it is not possible for us to gain samples including both sac and neck region or even whole aneurysms. A future study should aim at gaining whole AAAs from autopsies to confirm the hypothesis that intima and media burst open at a certain point in the disease progression.

Ethics.

The use of AAA materials from human subjects was approved by the Ethics Committee of the Medical University of Graz (27-250 ex 14/15).

Acknowledgements.

The authors would like to thank T. Weitlaner and M. Habenbacher for their support in the experimental study. Additionally we would like to thank the Institute of Science and Technology, Klosterneuburg, Austria, for its support in SHG imaging.

REFERENCES

[1] European Cardiovascular Disease Statistics 2017. *European Heart Network,* `http://www.ehnheart.org/cvd-statistics/cvd-statistics-2017.html`.

[2] E. J. Benjamin, M. J. Blaha, S. E. Chiuve, M. Cushman, S. R. Das, R. Deo, Sa. D. de Ferranti, Ja. Floyd, M. Fornage, Ca. Gillespie, C. R. Isasi, M. C. Jiménez, L. C. Jordan, S. E. Judd, D. Lackland, J. H. Lichtman, L. Lisabeth, S. Liu, C. T. Longenecker, R. H. Mackey, K. Matsushita, D. Mozaffarian, M. E. Mussolino, K. Nasir, R. W. Neumar, L. Palaniappan, Di. K. Pandey, R. R. Thiagarajan, M. J. Reeves, M. Ritchey, C. J. Rodriguez, G. A. Roth, W. D. Rosamond, C. Sasson, Am. Towfighi, C. W. Tsao, M. B. Turner, S. S. Virani, J. H. Voeks, J. Z. Willey, J. T. Wilkins, J. HY. Wu, H. M. Alger, S. S. Wong, and P. Muntner. Heart disease and stroke statistics—2017 update: A report from the american heart association. *Circulation*, 2017.

[3] L. Wang, L. Kong, F. Wu, Y. Bai, and R. Burton. Preventing chronic diseases in china. *The Lancet*, 366:1821–1824, 2005.

[4] J. T. Powell and L. C. Brown. The natural history of abdominal aortic aneurysms and their risk of rupture. *Acta Chir. Belg.*, 101:11–16, 2001.

[5] C. Fleming, E. P. Whitlock, T. L. Beil, and F. A. Lederle. Screening for abdominal aortic aneurysm: a best-evidence systematic review for the U.S. Preventive Services Task Force. *Ann. Intern. Med.*, 142:203–211, 2005.

[6] J. D. Humphrey and C. A. Taylor. Intracranial and abdominal aortic aneurysms: similarities, differences, and need for a new class of computational models. *Annu. Rev. Biomed. Eng.*, 10:221–246, 2008.

[7] N. Sakalihasan, R. Limet, and O. D. Defawe. Abdominal aortic aneurysm. *Lancet*, 365:1577–1589, 2005.

[8] A Karthikesalingam, S. S. Bahia, B. O. Patterson, G. Peach, A. Vidal-Diez, K. K. Ray, R. Sharma, R. J. Hinchliffe, P. J. Holt, and M. M. Thompson. The shortfall in long-term survival of patients with repaired thoracic or abdominal aortic aneurysms: retrospective case–control analysis of hospital episode statistics. *Eur. J. Vasc. Endovasc.*, 46:533–541, 2013.

[9] A. H. Malkawi, R. J. Hinchliffe, Y. Xu, P. J. Holt, I. M. Loftus, and M. M. Thompson. Patient-specific biomechanical profiling in abdominal aortic aneurysm development and rupture. *J. Vasc. Surg.*, 52:480–488, 2010.

[10] M. L. Raghavan and D. A. Vorp. Toward a biomechanical tool to evaluate rupture potential of abdominal aortic aneurysm: identification of a finite strain constitutive model and evaluation of its applicability. *J. Biomech.*, 33:475–482, 2000.

[11] M. F. Fillinger, M. L. Raghavan, S. P. Marra, J. L. Cronenwett, and F. E. Kennedy. In vivo analysis of mechanical wall stress and abdominal aortic aneurysm rupture risk. *J. Vasc. Surg.*, 36:589–597, 2002.

[12] M. F. Fillinger, S. P. Marra, M. L. Raghavan, and F. E. Kennedy. Prediction of rupture risk in abdominal aortic aneurysm during observation: wall stress versus diameter. *J. Vasc. Surg.*, 37:724–732, 2003.

[13] S. Polzer, C. T. Gasser, J. Bursa, R. Staffa, R. Vlachovskyand V. Man, and P. Skacel. Importance of material model in wall stress prediction in abdominal aortic aneurysms. *Med. Eng. Phys.*, 35:1282–1289, 2013.

[14] J. F. Rodríguez, C. Ruiz, M. Doblaré, and G. A. Holzapfel. Mechanical stresses in abdominal aortic aneurysms: influence of diameter, asymmetry and material anisotropy. *J. Biomech. Eng.*, 130:021023–1–10, 2008.

[15] M. H. Ross and W. Pawlina. *Histology : a text and atlas : with correlated cell and molecular biology*. Baltimore, MD: Lippincott Williams & Wilkins, 2006.

[16] M. H. Ross, W., and Pawlina. *Histology: A Text and Atlas: with Correlated Cell and Molecular Biology*. Lippincott Williams & Wilkins, 6th edition, 2011.

[17] M. R. Labrosse. Structure and mechanics of the artery. In M. J. Thubrikar, editor, *Vascular Mechanics and Pathology*, pages 45–81. Springer: New York, 2007.

[18] G. A. Holzapfel, G. Sommer, C. T. Gasser, and P. Regitnig. Determination of layer-specific mechanical properties of human coronary arteries with non-atherosclerotic intimal thickening, and related constitutive modeling. *Am. J. Physiol. Heart Circ. Physiol.*, 289:H2048–2058, 2005.

[19] A. J. Schriefl, G. Zeindlinger, D. M. Pierce, P. Regitnig, and G. A. Holzapfel. Determination of the layer-specific distributed collagen fiber orientations in human thoracic and abdominal aortas and common iliac arteries. *J. R. Soc. Interface*, 9: 1275–1286, 2012.

[20] D. Vela, L. M. Buja, M. Madjid, A. Burke, M. Naghavi, J. T. Willerson, S. W. Casscells, and S. Litovsky. The role of periadventitial fat in atherosclerosis: an adipose subset with potential diagnostic and therapeutic implications. *Arch. Pathol. Lab. Med.*, 131:481–487, 2007.

[21] K. A. Britton and C. S. Fox. Perivascular adipose tissue and vascular disease. *Clin. Lipidol.*, 6:79–91, 2011.

[22] V. R. Sherman, W. Yang, and M. A. Meyers. The material science of collagen. *J. Mech. Behav. Mater.*, 52:22–50, 2015.

[23] J. Díez. Arterial stiffness and extracellular matrix. *Adv. Cardiol.*, 44:76–95, 2007.

[24] D. J. S. Hulmes. Collagen diversity, synthesis and assembly. In P. Fratzl, editor, *Collagen: Structure and Mechanics*, pages 15–47. Springer, 2008.

[25] C. M. Fitzsimmons and C. M. Shanahan. Vascular extracellular matrix. In P. Lanzer and E. J. Topol, editors, *Pan Vascular Medicine*, pages 217–231. Springer, 2002.

[26] V. Ottani, M. Raspanti, and A. Ruggeri. Collagen structure and functional implications. *Micron*, 32:251–260, 2001.

[27] Y. C. Fung. *Biomechanics. Mechanical Properties of Living Tissues*. Springer-Verlag, New York, 2nd edition, 1993.

[28] M. Wolman and F. H. Kasten. Polarized light microscopy in the study of the molecular structure of collagen and reticulin. *Histochemistry*, 85:41–49, 1986.

[29] L. C. Junqueira, W. Cossermelli, and R. Brentani. Differential staining of collagens type I, II and III by Sirius Red and polarization microscopy. *Arch. Histol. Jpn.*, 41: 267–274, 1978.

[30] L. C. Junqueira, G. Bignolas, and R. R. Brentani. Picrosirius staining plus polarization microscopy, a specific method for collagen detection in tissue sections. *Histochem. J.*, 11:447–455, 1979.

[31] B. R. Masters and P. T. C. So. Multiphoton excitation microscopy and confocal microscopy imaging of in vivo human skin: a comparison. *Microsc. Microanal.*, 5: 282–289, 1999.

[32] S. Roth and I. Freund. Second harmonic generation in collagen. *J. Chem. Phys.*, 70: 1637–1643, 1979.

[33] W. Denk, J. H. Strickler, and W. W. Webb. Two-photon laser scanning fluorescence microscopy. *Science*, 248:73–76, 1990.

[34] S. M. Mithieux and A. S. Weiss. Elastin. *Adv. Protein Chem.*, 70:437–461, 2005.

[35] R. B. Rucker and D. Tinker. Structure and metabolism of arterial elastin. *Int. Rev. Exp. Pathol.*, 17:1–41, 1977.

[36] D. D. Stromberg and C. A. Wiederhielm. Viscoelastic description of a collagenous tissue in simple elongation. *J. Appl. Physiol.*, 26:857–862, 1969.

[37] E. U. Azeloglu, M. B. Albro, V. A. Thimmappa, G. A. Ateshian, and K. D. Costa. Heterogeneous transmural proteoglycan distribution provides a mechanism for regulating residual stresses in the aorta. *Am. J. Physiol.-Heart C.*, 294:H1197–H1205, 2008.

[38] V. Lesauskaite, L. Ivanoviene, and A. Valanciute. Programmed cellular death and atherogenesis: from molecular mechanisms to clinical aspects. *Medicina (Kaunas)*, 39:529–34, 2003.

[39] G. A. Holzapfel, T. C. Gasser, and R. W. Ogden. A new constitutive framework for arterial wall mechanics and a comparative study of material models. *J. Elasticity*, 61:1–48, 2000.

[40] M. R. Roach and A. C. Burton. The reason for the shape of the distensibility curves of arteries. *Canad. J. Biochem. Physiol.*, 35:681–690, 1957.

[41] D. H. Bergel. *The visco-elastic properties of the arterial wall*. PhD thesis, University of London, 1960.

[42] Y. C. Fung. On the foundations of biomechanics. *J. Appl. Mech.*, 50:1003–1009, 1983.

[43] R. N. Vaishnav and J. Vossoughi. Estimation of residual strains in aortic segments. In C. W. Hall, editor, *Biomedical Engineering II: Recent Developments*, pages 330–333. Pergamon Press, New York, 1983.

[44] C. J. Chuong and Y. C. Fung. On residual stress in arteries. *J. Biomech. Eng.*, 108: 189–192, 1986.

[45] K. Takamizawa and K. Hayashi. Strain energy density function and uniform strain hypothesis for arterial mechanics. *J. Biomech.*, 20:7–17, 1987.

[46] R. Skalak, G. Dasgupta, M. Moss, E. Otten, P. Dullemeijer, and H. Vilmann. Analytical description of growth. *J. Theor. Biol.*, 94:555–577, 1982.

[47] A. Sani, C. Berry, and S. Greenwald. Effect of age and sex on residual stress in the aorta. *J. Vasc. Res.*, 32:398–405, 1995.

[48] R. W. Lawton. The thermoelastic behavior of isolated aortic strips of the dog. *Circ. Res.*, 2:344–353, 1954.

[49] P. B. Dobrin and A. A. Rovick. Influence of vascular smooth muscle on contractile mechanics and elasticity of arteries. *Am. J. Physiol.*, 217:1644–1651, 1969.

[50] T. E. Carew, R. N. Vaishnav, and D. J. Patel. Compressibility of the arterial wall. *Circ. Res.*, 23:61–68, 1968.

[51] Y. C. Fung. *Biomechanics: Mechanical Properties of Living Tissue*. Springer-Verlag, New York, 1981.

[52] D. F. Elger, R. S. Blackketter, R. S. Budwig, and K. H. Johansen. The influence of shape on the stresses in model abdominal aortic aneurysms. *J. Biomed. Eng.*, 118: 326–332, 1996.

[53] M. L. Raghavan, J. Kratzberg, E. M. Castro de Tolosa, M. M. Hanaoka, P. Walker, and E. S. da Silva. Regional distribution of wall thickness and failure properties of human abdominal aortic aneurysm. *J. Biomech.*, 39:3010–3016, 2006.

[54] L. P. Harter, B. H. Gross, R. A. Callen, and R. A. Barth. Ultrasonic evalution of abdominal aortic thrombus. *J. Ultrasound. Med.*, 1:315–318, 1982.

[55] Y. G. Wolf, W. S. Thomas, F. J. Brennan, W. G. Goff, M. J. Sise, and E. F. Bernstein. Computed tomography scanning findings associated with rapid expansion of abdominal aortic aneurysms. *J. Vasc. Surg.*, 20:529–535, 1994.

[56] J. S. Campa, R. M. Greenhalgh, and J. T. Powell. Elastin degradation in abdominal aortic aneurysms. *Atherosclerosis*, 65:13–21, 1987.

[57] C. M. He and M. R. Roach. The composition and mechanical properties of abdominal aortic aneurysms. *J. Vasc. Surg.*, 20:6–13, 1994.

[58] B. T. Baxter, G. S. McGee, V. P. Shively, I. A. Drummond, S. N. Dixit, M. Yamauchi, and W. H. Pearce. Elastin content, cross-links, and mRNA in normal and aneurysmal human aorta. *J. Vasc. Surg.*, 16:192–200, 1992.

[59] J. J. Alexander. The pathobiology of aortic aneurysms. *J. Surg. Res.*, 117:163–175, 2004.

[60] N. Diehm, F. Dick, T. Schaffner, J. Schmidli, C. Kalka, S. Di Santo, J. Voelzmann, and I. Baumgartner. Novel insight into the pathobiology of abdominal aortic aneurysm and potential future treatment concepts. *Prog. Cardiovasc. Dis.*, 50:209–217, 2007.

[61] M. Wassef, B. T. Baxter, R. L. Chisholm, R. L. Dalman, M. F. Fillinger, J. Heinecke, J. D. Humphrey, H. Kuivaniemi, W. C. Parks, W. H. Pearce, C.D. Platsoucas, G. K. Sukhova, R.W. Thompson, M.D. Tilson, and C.K. Zarins. Pathogenesis of abdominal aortic aneurysms: a multidisciplinary research program supported by the national heart, lung, and blood institute. *J. Vasc. Surg.*, 34:730–738, 2001.

[62] I. M. Nordon, R. J. Hinchliffe, I. M. Loftus, and M. M. Thompson. Pathophysiology and epidemiology of abdominal aortic aneurysms. *Nat. Rev. Cardiol.*, 8:92–102, 2011.

[63] C. W. Kotze and I. G. Ahmed. Etiology and pathogenisis of aortic aneurysm. In *Etiology, pathogenesis and pathophysiology of aortic aneurysms and aneurysm rupture*. InTech, 2011.

[64] F. Hellenthal, W. A. Buurman, W. Wodzig, and G. W. H. Schurink. Biomarkers of abdominal aortic aneurysm progression. part 2: inflammation. *Nat. Rev. Cardiol.*, 6:543–552, 2009.

[65] P. B. Dobrin and T. R. Canfield. Elastase, collagenase, and the biaxial elastic properties of dog carotid artery. *Am. J. Physiol.*, 247:H124–H131, 1984.

[66] J. R Cohen, C. Mandell, J. B. Chang, and L. Wise. Elastin metabolism of the infrarenal aorta. *J. Vasc. Surg.*, 7:210–214, 1988.

[67] M. J. Davies. Aortic aneurysm formation: lessons from human studies and experimental models. *Circulation*, 98:193–195, 1998.

[68] J. E. Rundhaug. Matrix metalloproteinases, angiogenesis, and cancer. *Cli. Cancer Res.*, 9:551–554, 2003.

[69] E. Petersen, F. Wågberg, and K. A. Ängquist. Proteolysis of the abdominal aortic aneurysm wall and the association with rupture. *Eur. J. Vasc. Endovasc.*, 23:153–157, 2002.

[70] T. Freestone, R. J. Turner, A. Coady, D. J. Higman, R. M. Greenhalgh, and J. T. Powell. Inflammation and matrix metalloproteinases in the enlarging abdominal aortic aneurysm. *Arterioscl. Throm. Vas.*, 15:1145–1151, 1995.

[71] P. K. Shah. Inflammation, metalloproteinases, and increased proteolysis: an emerging pathophysiologic paradigm in aortic aneurysm. *Circulation*, 96:2228–2232, 1997.

[72] J. S. Lindholt and G. P. Shi. Chronic inflammation, immune response, and infection in abdominal aortic aneurysms. *Eur. J. Vasc. Endovasc.*, 31:453–463, 2006.

[73] V. Třeška, O. Topolčan, and L. Pecen. Cytokines as plasma markers of abdominal aortic aneurysm. *Clin. Chem. Lab. Med.*, 38:1161–1164, 2000.

[74] J. Juvonen, H.-M. Surcel, J. Satta, A.-M. Teppo, A. Bloigu, H. Syrjälä, J. Airaksinen, M. Leinonen, P. Saikku, and T. Juvonen. Elevated circulating levels of inflammatory cytokines in patients with abdominal aortic aneurysm. *Arterioscl. Throm. Vas.*, 17:2843–2847, 1997.

[75] U. Schönbeck, G. K. Sukhova, N. Gerdes, and P. Libby. T(h)2 predominant immune responses prevail in human abdominal aortic aneurysm. *Am. J. Pathol.*, 161:499–506, 2002.

[76] J. A. Phillippi, S. Pasta, and D. A. Vorp. Biomechanics and pathobiology of aortic aneurysms. In T. McGloughlin, editor, *Biomechanics and Mechanobiology of Aneurysms*, pages 67–118. Springer, Heidelberg, 2011.

[77] N. P. Kadoglou and C. D. Liapis. Matrix metalloproteinases: contribution to pathogenesis, diagnosis, surveillance and treatment of abdominal aortic aneurysms. *Curr. Med. Res. Opin.*, 20:419–432, 2004.

[78] D. A. Vorp, P. C. Lee, D. H. Wang, M. S. Makaroun, E. M. Nemoto, S. Ogawa, and M. W. Webster. Association of intraluminal thrombus in abdominal aortic aneurysm with local hypoxia and wall weakening. *J. Vasc. Surg.*, 34:291–299, 2001.

[79] E. L. Henderson, Y. Geng, G. K. Sukhova, A. D. Whittemore, J. Knox, and P. Libby. Death of smooth muscle cells and expression of mediators of apoptosis by T lymphocytes in human abdominal aortic aneurysms. *Circulation*, 99:96–104, 1999.

[80] J. Swedenborg and P. Eriksson. The intraluminal thrombus as a source of proteolytic activity. *Ann. N.Y. Acad. Sci.*, 1085:133–138, 2006.

[81] M. Kazi, J. Thyberg, P. Religa, J. Roy, P. Eriksson, U. Hedin, and J. Swedenborg. Influence of intraluminal thrombus on structural and cellular composition of abdominal aortic aneurysm wall. *J. Vasc. Surg.*, 38:1283–1292, 2003.

[82] F. A. Lederle, G. R. Johnson, S. E. Wilson, E. P. Chute, F. N. Littooy, D. Bandyk, W. C. Krupski, G. W. Barone, C. W. Acher, and D. J. Ballard. Prevalence and associations of abdominal aortic aneurysm detected through screening. *Ann. Intern. Med.*, 126:441–449, 1997.

[83] K. Singh, K. H. Bønaa, B. K. Jacobsen, L. Bjørk, and S. Solberg. Prevalence of and risk factors for abdominal aortic aneurysms in a population-based study: The Tromsø Study. *Am. J. Epidemiol.*, 154:236–244, 2001.

[84] J. D. Humphrey and G. A. Holzapfel. Mechanics, mechanobiology, and modeling of human abdominal aorta and aneurysms. *J. Biomech.*, 45:805–814, 2012.

[85] N. Grootenboer, J. L. Bosch, J. M. Hendriks, and M. R. van Sambeek. Epidemiology, aetiology, risk of rupture and treatment of abdominal aortic aneurysms: does sex matter? *Eur. J. Vasc. Endovasc. Surg.*, 38:278–284, 2009.

[86] R. Mofidi, V. J. Goldie, J. Kelman, A. R. Dawson, J. A. Murie, and R. T. Chalmers. Influence of sex on expansion rate of abdominal aortic aneurysms. *Br. J. Surg.*, 94: 310–314, 2007.

[87] E. G. Lakatta, M. Wang, and S. S. Najjar. Arterial aging and subclinical arterial disease are fundamentally intertwined at macroscopic and molecular levels. *Med. Clin. N. Am.*, 93:583–604, 2009.

[88] M. Sagiv and U. Goldbourt. Influence of physical work on high density lipoprotein cholesterol: implications for the risk of coronary heart disease. *Int. J. Sports Med.*, 15:261–266, 1994.

[89] H. J. C. M. Pleumeekers, A. W. Hoes, E. Van Der Does, H. Van Urk, A. Hofman, P. T. V. M. De Jong, and D. E. Grobbee. Aneurysms of the abdominal aorta in older adults: the rotterdam study. *Am. J. Epidemiol.*, 142:1291–1299, 1995.

[90] C. Iribarren, J. A. Darbinian, A. S. Go, B. H. Fireman, C. D. Lee, and D. P. Grey. Traditional and novel risk factors for clinically diagnosed abdominal aortic aneurysm: the kaiser multiphasic health checkup cohort study. *Ann. Epidemiol.*, 17:669–678, 2007.

[91] O. Schouten, J. H. H. van Laanen, E. Boersma, R. Vidakovic, H. H. H. Feringa, M. Dunkelgrün, J. J. Bax, J. Koning, H. van Urk, and D. Poldermans. Statins are associated with a reduced infrarenal abdominal aortic aneurysm growth. *Eur. J. Vasc. Endovasc.*, 32:21–26, 2006.

[92] H. Bengtsson, B. Sonesson, and D. Bergqvist. Incidence and prevalence of abdominal aortic aneurysms, estimated by necropsy studies and population screening by ultrasound. *Ann. NY Acad. Sci.*, 800:1–24, 1996.

[93] A. R. Brady, S. G. Thompson, F. G. R. Fowkes, R. M. Greenhalgh, and J. T. Powell. Abdominal aortic aneurysm expansion: Risk factors and time intervals for surveillance. *Circulation*, 110:16–21, 2004.

[94] J. Golledge, J. Muller, A. Daugherty, and P. Norman. Abdominal aortic aneurysm: pathogenesis and implications for management. *Arterioscl. Throm. Vas.*, 26:2605–2613, 2006.

[95] J. S. Weiss and B. E. Sumpio. Review of prevalence and outcome of vascular disease in patients with diabetes mellitus. *Eur. J. Vasc. Endovasc.*, 31:143–150, 2006.

[96] M. L. Raghavan and E. S. da Silva. Mechanical properties of AAA tissue. In T. McGloughlin, editor, *Biomechanics and Mechanobiology of Aneurysms*, pages 139–162. Springer, 2011.

[97] T. Länne, B. Sonesson, D. Bergqvist, H. Bengtsson, and D. Gustafsson. Diameter and compliance in the male human abdominal aorta: influence of age and aortic aneurysm. *Eur. J. Vasc. Surg.*, 6:178–184, 1992.

[98] S. T. MacSweeney, G. Young, R. M. Greenhalgh, and J. T. Powell. Mechanical properties of the aneurysmal aorta. *Br. J. Surg.*, 79:1281–1284, 1992.

[99] A. Wittek, C. Blase, W. Derwich, T. Schmitz-Rixen, and C.-P. Fritzen. Characterization of the mechanical behavior and pathophysiological state of abdominal aortic aneurysms based on 4D ultrasound strain imaging. In *Proc. SPIE*, volume 10333, page 1033303. International Society for Optics and Photonics, 2017.

[100] A. Wittek, K. Karatolios, P. Bihari, T. Schmitz-Rixen, R. Moosdorf, S. Vogt, and C. Blase. In vivo determination of elastic properties of the human aorta based on 4d ultrasound data. *J. Mech. Behav. Biomed.*, 27:167–183, 2013.

[101] A. Long, L. Rouet, A. Bissery, P. Rossignol, D. Mouradian, and M. Sapoval. Compliance of abdominal aortic aneurysms evaluated by tissue doppler imaging: correlation with aneurysm size. *J. Vasc. Surg.*, 42:18–26, 2005.

[102] M.-K. Ganten, U. Krautter, H. von Tengg-Kobligk, D. Böckler, H. Schumacher, W. Stiller, S. Delorme, H.-U. Kauczor, G. W. Kauffmann, and M. Bock. Quantification of aortic distensibility in abdominal aortic aneurysm using ecg-gated multidetector computed tomography. *Eur. Radiol.*, 18:966–973, 2008.

[103] D. S. Sumner, D. E. Hokanson, and D. E. Strandness Jr. Stress-strain characteristics and collagen-elastin content of abdominal aortic aneurysms. *Surg. Gynecol. Obstet.*, 130:459–466, 1970.

[104] M. Drangova, D. W. Holdsworth, C. J. Boyd, P. J. Dunmore, M. R. Roach, and A. Fenster. Elasticity and geometry measurements of vascular specimens using a high resolution laboratory CT scanner. *Physiol. Meas.*, 14:277–290, 1993.

[105] D. A. Vorp, M. L. Raghavan, S. C. Muluk, M. S. Makaroun, D. L. Steed, R. Shapiro, and M. W. Webster. Wall strength and stiffness of aneurysmal and nonaneurysmal abdominal aorta. *Ann. N.Y. Acad. Sci.*, 800:274–276, 1996.

[106] M. L. Raghavan, M. W. Webster, and D. A. Vorp. Ex vivo biomechanical behavior of abdominal aortic aneurysm: assesment using a new mathematical model. *Ann. Biomed. Eng.*, 24:573–582, 1996.

[107] M. J. Thubrikar, M. Labrosse, F. Robicsek, J. Al-Soudi, and B. Fowler. Mechanical properties of abdominal aortic aneurysm wall. *J. Med. Eng. Technol.*, 25:133–142, 2001.

[108] D. M. Pierce, T. E. Fastl, B. Rodriguez-Vila, P. Verbrugghe, I. Fourneau, G. Maleux, P. Herijgers, E. J. Gomez, and G. A. Holzapfel. A method for incorporating three-dimensional residual stretches/stresses into patient-specific finite element simulations of arteries. *J. Mech. Behav. Biomed. Mater.*, 47:147–164, 2015.

[109] S. G. Sassani, J. Kakisis, S. Tsangaris, and D. P. Sokolis. Layer-dependent wall properties of abdominal aortic aneurysms: Experimental study and material characterization. *J. Mech. Behav. Biomed. Mater.*, 49:141–161, 2015.

[110] J. P. Vande Geest, M. S. Sacks, and D. A. Vorp. The effects of aneurysm on the biaxial mechanical behavior of human abdominal aorta. *J. Biomech.*, 39:1324–1334, 2006.

[111] J. P. Vande Geest, M. S. Sacks, and D. A. Vorp. A planar biaxial constitutive relation for the luminal layer of intra-luminal thrombus in abdominal aortic aneurysms. *J. Biomech.*, 39:2347–2354, 2006.

[112] J. Tong, T. Cohnert, P. Regitnig, and G. A. Holzapfel. Effects of age on the elastic properties of the intraluminal thrombus and the thrombus-covered wall in abdominal aortic aneurysms: biaxial extension behavior and material modeling. *Eur. J. Vasc. Endovasc. Surg.*, 42:207–219, 2011.

[113] S. A. O'Leary, D. A. Healey, E. G. Kavanagh, M. T. Walsh, T. M. McGloughlin, and B. J. Doyle. The biaxial biomechanical behavior of abdominal aortic aneurysm tissue. *Ann. Biomed. Eng.*, 42:2440–2450, 2014.

[114] P. N. Watton, N. A. Hill, and M. Heil. A mathematical model for the growth of the abdominal aortic aneurysm. *Biomech. Model. Mechanobiol.*, 3:98–113, 2004.

[115] K. Y. Volokh and D. A. Vorp. A model of growth and rupture of abdominal aortic aneurysm. *J. Biomech.*, 41:1015–1021, 2008.

[116] T. C. Gasser, S. Gallinetti, X. Xing, C. Forsell, J. Swedenborg, and J. Roy. Spatial orientation of collagen fibers in the abdominal aortic aneurysm's wall and its relation to wall mechanics. *Acta Biomater.*, 8:3091–3103, 2012.

[117] R. Søgaard, J. Laustsen, and J. S. Lindholt. Cost effectiveness of abdominal aortic aneurysm screening and rescreening in men in a modern context: evaluation of a hypothetical cohort using a decision analytical model. *BMJ*, 345:e4276, 2012.

[118] United Kingdom EVAR Trial Investigators et al. Endovascular versus open repair of abdominal aortic aneurysm. *N. Engl. J. Med.*, 2010:1863–1871, 2010.

[119] R. C. Darling, C. R. Messina, D. C. Brewster, and L. W. Ottinger. Autopsy study of unoperated abdominal aortic aneurysms. *Circulation*, 56 (II suppl):161–164, 1977.

[120] A.J. Hall, E. F. G. Busse, McCarville D. J., and J. J. Burgess. Aortic wall tension as a predictive factor for abdominal aortic aneurysm rupture: Improving the selection of patients for abdominal aortic aneurysm repair. *Ann. Vasc. Surg.*, 14:152 – 157, 2000.

[121] J. T. Powell. Final 12-year follow-up of surgery versus surveillance in the UK small aneurysm trial. *Brit. J. Surg.*, 94:702–708, 2007.

[122] G. Martufi and T. C. Gasser. the role of biomechanical modeling in the rupture risk assessment for abdominal aortic aneurysms. *J. Biomed Eng.*, 135:021010, 2013.

[123] R. Limet, N. Sakalihassan, and A. Albert. Determination of the expansion rate and incidence of ruptur of abdominal aortic aneurysms. *J. Vasc. Surg.*, 14:540 – 548, 1991.

[124] D. C. Brewester, J. L. Cronenwett, J. W. Hallett Jr., K. W. Johnston, W. C. Krupski, and J. S. Matsumura. Guidelines for the treatment of abdominal aortic aneurysms. report of a subcommittee of joint council of the american association of vascular surgery and society of vascular surgery. *J. Vasc. Surg.*, 37:1106–1117, 2003.

[125] G. Martufi, M. Auer, J. Roy, J. Swedenborg, N. Sakalihasan, G. Panuccio, and T. Ch. Gasser. Multidimensional growth measurements of abdominal aortic aneurysms. *J. Vasc. Surg.*, 58:748 – 755, 2013.

[126] J. Stenbaek, B. Kalin, and J. Swedenborg. Growth of thrombus may be a better predictor of rupture than diameter in patients with abdominal aortic aneurysms. *Eur. J. Vasc. Endovasc. Surg.*, 20:466–499, 2000.

[127] A. Parr, M. McCann, B. Bradshaw, A. Shahzad, P. Buttner, and J. Golledge. Thrombus volume is associated with cardiovascular events and aneurysm growth in patients who have abdominal aortic aneurysms. *J. Vasc. Surg.*, 53:28–35, 2011.

[128] M. F. Fillinger, J. Racusin, R. K. Baker, J. L. Cronenwett, A. Teutelink, M. L. Schermerhorn, R. M. Zwolak, R. J. Powell, D. B. Walsh, and E. M. Rzucidlo. Anatomic characteristics of ruptured abdominal aortic aneurysm on conventional CT scans: implications for rupture risk. *J. Vasc. Surg.*, 39:1243–1252, 2004.

[129] B. J. Doyle, A. Callanan, P. E. Burke, P. A. Grace, M. T. Walsh, D. A. Vorp, and T. M. McGloughlin. Vessel asymmetry as an additional diagnostic tool in the assessment of abdominal aortic aneurysms. *J. Vasc. Surg.*, 49:443–454, 2009.

[130] C. Reeps, A. Maier, J. Pelisek, F. Härtl, V. Grabher-Meier, W. A. Wall, M. Essler, H. H. Eckstein, and M. W. Gee. Measuring and modeling patient-specific distributions of material properties in abdominal aortic aneurysm wall. *Biomech. Model. Mechanobiol.*, 12:717–733, 2013.

[131] E. S. Di Martino and D. A. Vorp. Effect of variation in intraluminal thrombus constitutive properties on abdominal aortic aneurysm wall stress. *Ann. Biomed. Eng.*, 31:804–809, 2003.

[132] J. A. Niestrawska, D. Haspinger, and G. A. Holzapfel. The influence of fiber dispersion on the mechanical response of aortic tissues in health and disease: A computational study. *Comput. Methods Biomech. Biomed. Engin.*, in press.

[133] T. C. Gasser, M. Auer, F. Labruto, J. Swedenborg, and J. Roy. Biomechanical rupture risk assessment of abdominal aortic aneurysms: model complexity versus predictability of finite element simulations. *Eur. J. Vasc. Endovasc. Surg.*, 40:176–185, 2010.

[134] T. C. Gasser, R. W. Ogden, and G. A. Holzapfel. Hyperelastic modelling of arterial layers with distributed collagen fibre orientations. *J. R. Soc. Interface*, 3:15–35, 2006.

[135] FEAP. – A Finite Element Analysis Program,Version 8.4, User Manual. University of California at Berkeley, California, 2013.

[136] P. B. Canham, H. M. Finlay, J. G. Dixon, D. R. Boughner, and A. Chen. Measurements from light and polarised light microscopy of human coronary arteries fixed at distending pressure. *Cardiovasc. Res.*, 23:973–982, 1989.

[137] H. M. Finlay, L. McCullough, and P. B. Canham. Three-dimensional collagen organization of human brain arteries at different transmural pressures. *J. Vasc. Res.*, 32:301–312, 1995.

[138] H. M. Finlay, P. Whittaker, and P. B. Canham. Collagen organization in the branching region of human brain arteries. *Stroke*, 29:1595–1601, 1998.

[139] A. J. Schriefl, A. J. Reinisch, S. Sankaran, D. M. Pierce, and G. A. Holzapfel. Quantitative assessment of collagen fiber orientations from 2D images of soft biological tissues. *J. R. Soc. Interface*, 9:3081–3093, 2012.

[140] G. A. Holzapfel. Collagen in arterial walls: Biomechanical aspects. In P. Fratzl, editor, *Collagen. Structure and Mechanics*, pages 285–324, Heidelberg, 2008. Springer-Verlag.

[141] C. J. Cyron and J. D. Humphrey. Preferred fiber orientations in healthy arteries and veins understood from netting analysis. *Math. Mech. Solids*, 20:680–696, 2015.

[142] W. J. Karlon, J. W. Covell, A. D. McCulloch, J. J. Hunter, and J. H. Omens. Automated measurement of myofiber disarray in transgenic mice with ventricular expression of ras. *Anat. Rec.*, 252:612–625, 1998.

[143] J. W. Covell. Tissue structure and ventricular wall mechanics. *Circulation*, 118: 699–701, 2008.

[144] C. Boote, S. Dennis, and K. Meek. Spatial mapping of collagen fibril organisation in primate cornea-an X-ray diffraction investigation. *J. Struct. Biol.*, 146:359–367, 2004.

[145] C. Boote, S. Dennis, Y. Huang, A. J. Quantock, and K. M. Meek. Lamellar orientation in human cornea in relation to mechanical properties. *J. Struct. Biol.*, 149:1–6, 2005.

[146] M. B. Lilledahl, D. M. Pierce, T. Ricken, G. A. Holzapfel, and C. de Lange Davies. Structural analysis of articular cartilage using multiphoton microscopy: input for biomechanical modeling. *IEEE Trans. Med. Imaging*, 30:1635–1648, 2011.

[147] D. H. Cortes, S. P. Lake, J. A. Kadlowec, L. J. Soslowsky, and D. M. Elliot. Characterizing the mechanical contribution of fiber angular distribution in connective tissue: comparison of two modeling approaches. *Biomech. Model. Mechanobiol.*, 9:651–658, 2010.

[148] G. A. Holzapfel, M. J. Unterberger, and R. W. Ogden. An affine continuum mechanical model for cross-linked F-actin networks with compliant linker proteins. *J. Mech. Behav. Biomed. Mater.*, 38:78–90, 2014.

[149] G. A. Holzapfel and R. W. Ogden. On the tension–compression switch in soft fibrous solids. *Eur. J. Mech. A/Solids*, 49:561–569, 2015.

[150] A. V. Melnik, H. Borja Da Rocha, and A. Goriely. On the modeling of fiber dispersion in fiber-reinforced elastic materials. *Int. J. Non-Linear Mech.*, 75:92–106, 2015.

[151] Y. Lanir. Constitutive equations for fibrous connective tissues. *J. Biomech.*, 16: 1–12, 1983.

[152] M. S. Sacks. Incorporation of experimentally-derived fiber orientation into a structural constitutive model for planar collagenous tissues. *J. Biomech. Eng.*, 125:280–287, 2003.

[153] N. J. B. Driessen, C. V. C. Bouten, and F. P. T. Baaijens. A structural constitutive model for collagenous cardiovascular tissue incorporating the angular fiber distribution. *J. Biomech. Eng.*, 127:494–503, 2005.

[154] A. D. Freed, D. R. Einstein, and I. Vesely. Invariant formulation for dispersed transverse isotropy in aortic heart valves: An efficient means for modeling fiber splay. *Biomech. Model. Mechanobiol.*, 4:100–117, 2005.

[155] Y. C. Fung. Elasticity of soft tissues in simple elongation. *Am. J. Physiol.*, 213: 1532–1544, 1967.

[156] A. Pandolfi and G. A. Holzapfel. Three-dimensional modeling and computational analysis of the human cornea considering distributed collagen fibril orientations. *J. Biomech. Eng.*, 130:061006 (12 pages), 2008.

[157] D. M. Pierce, W. Trobin, J. G. Raya, S. Trattnig, H. Bischof, Ch. Glaser, and G. A. Holzapfel. DT-MRI based computation of collagen fiber deformation in human articular cartilage: a feasibility study. *Ann. Biomed. Eng.*, 38:2447–2463, 2010.

[158] M. Kroon and G. A. Holzapfel. A new constitutive model for multi-layered collagenous tissues. *J. Biomech.*, 41:2766–2771, 2008.

[159] R. W. Ogden. Anisotropy and nonlinear elasticity in arterial wall mechanics. In G. A. Holzapfel and R. W. Ogden, editors, *Biomechanical Modelling at the Molecular, Cellular and Tissue Levels. CISM Courses and Lectures no. 508*, pages 179–258, Wien, New York, 2009. Springer-Verlag. CISM Courses and Lectures no. 508.

[160] G. A. Holzapfel and R. W. Ogden. Modelling the layer-specific 3D residual stresses in arteries, with an application to the human aorta. *J. R. Soc. Interface*, 7:787–799, 2010.

[161] Y. Wang, S. Son, S. M. Swartz, and N. C. Goulbourne. A mixed von Mises distribution for modeling soft biological tissues with two distributed fiber properties. *Int. J. Solids Structures*, 49:2914–2923, 2012.

[162] V. Alastrué, M. A. Martínez, A. Menzel, and M. Doblaré. On the use of non-linear transformations for the evaluation of anisotropic rotationally symmetric directional integrals. application to the stress analysis in fibred soft tissues. *Int. J. Numer. Meth. Engng*, 79:474–504, 2009.

[163] G. A. Ateshian, V. Rajan, N. O. Chahine, C. E. Canal, and C. T. Hung. Modeling the matrix of articular cartilage using a continuous fiber angular distribution predicts many observed phenomena. *J. Biomech. Eng.*, 131:61003, 2009.

[164] R. Raghupathy and V. H. Barocas. A closed-form structural model of planar fibrous tissue mechanics. *J. Biomech.*, 42:1424–1428, 2009.

[165] S. Federico and T. C. Gasser. Nonlinear elasticity of biological tissues with statistical fibre orientation. *J. R. Soc. Interface*, 7:955–966, 2010.

[166] A. Agianniotis, R. Rezakhaniha, and N. Stergiopulos. A structural constitutive model considering angular dispersion and waviness of collagen fibres of rabbit facial veins. *Biomed. Eng. Online*, 10:18, 2011.

[167] A. Pandolfi and M. Vasta. Fiber distributed hyperelastic modeling of biological tissues. *Mech. Mat.*, 44:151–162, 2012.

[168] A. D. Freed and T. C. Doehring. Elastic model for crimped collagen fibrils. *J. Biomech. Eng.*, 127:587–593, 2005.

[169] G. A. Holzapfel and R. W. Ogden. Constitutive modelling of arteries. *Proc. R. Soc. Lond. A*, 466:1551–1597, 2010.

[170] N. I. Fisher, T. L. Lewis, and B. J. J. Embleton. *Statistical Analysis of Spherical Data*. Cambridge University Press, Cambridge, 1987.

[171] P. J. Flory. Thermodynamic relations for highly elastic materials. *Trans. Faraday Soc.*, 57:829–838, 1961.

[172] R. W. Ogden. Nearly isochoric elastic deformations: Application to rubberlike solids. *J. Mech. Phys. Solids*, 26:37–57, 1978.

[173] G. A. Holzapfel. *Nonlinear Solid Mechanics. A Continuum Approach for Engineering*. John Wiley & Sons, Chichester, 2000.

[174] J. C. Simo and R. L. Taylor. Quasi-incompressible finite elasticity in principal stretches. Continuum basis and numerical algorithms. *Comput. Meth. Appl. Mech. Eng.*, 85:273–310, 1991.

[175] G. A. Holzapfel and H. W. Weizsäcker. Biomechanical behavior of the arterial wall and its numerical characterization. *Comp. Biol. Med.*, 28:377–392, 1998.

[176] D. C. Montgomery and G. C. Runger. *Applied Statistics and Probability for Engineers*. John Wiley & Sons, Ltd, 2010.

[177] A. J. Schriefl, H. Wolinski, P. Regitnig, S. D. Kohlwein, and G. A. Holzapfel. An automated approach for 3D quantification of fibrillar structures in optically cleared soft biological tissues. *J. R. Soc. Interface*, 10:2012–0760, 2013.

[178] E. Choke, G. Cockerill, W. R. W. Wilson, S. Sayed, J. Dawson, I. Loftus, and M. M. Thompson. A review of biological factors implicated in abdominal aortic aneurysm rupture. *Eur. J. Vasc. Endovasc. Surg.*, 30:227–244, 2005.

[179] D. A. Vorp and J. P. Vande Geest. Biomechanical determinants of abdominal aortic aneurysm rupture. *Arterioscler. Thromb. Vasc. Biol.*, 25:1558–1566, 2005.

[180] F. A. Lederle, S. E. Wilson, G. R. Johnson, D. B. Reinke, F. N. Littooy, C. W. Acher, D. J. Ballard, L. M. Messina, I. L. Gordon, E. P. Chute, W. C. Krupski, S. J. Busuttil, G. W. Barone, S. Sparks, L. M. Graham, J. H. Rapp, M. S. Makaroun, G. L. Moneta, R. A. Cambria, R. G. Makhoul, D. Eton, H. J. Ansel, J. A. Freischlag, D. Bandyk, and Aneurysm Detection and Management Veterans Affairs Cooperative Study Group. Immediate repair compared with surveillance of small abdominal aortic aneurysms. *N. Engl. J. Med.*, 346:1437–1444, 2002.

[181] G. A. Holzapfel, J. Tong, T. Cohnert, and P. Regitnig. Recent advances in the biomechanics of abdominal aortic aneurysms. In N. Chakfé, B. Durand, and W. Meichelboeck, editors, *ESVB 2011 New Endovascular Technologies. From Bench Test to Clinical Practice*, pages 23–40, Strasbourg, France, 2011. Europrot.

[182] J. D. Humphrey. *Cardiovascular Solid Mechanics. Cells, Tissues, and Organs*. Springer-Verlag, New York, 2002.

[183] J. P. Vande Geest, M. S. Sacks, and D. A. Vorp. Age dependency of the biaxial biomechanical behavior of human abdominal aorta. *J. Biomech. Eng.*, 126:815–822, 2004.

[184] H. Weisbecker, D. M. Pierce, P. Regitnig, and G. A. Holzapfel. Layer-specific damage experiments and modeling of human thoracic and abdominal aortas with non-atherosclerotic intimal thickening. *J. Mech. Behav. Biomed. uMater.*, 12:93–106, 2012.

[185] E. S. Di Martino, A. Bohra, J. P. Vande Geest, N. Y. Gupta, M. S. Makaroun, and D. A. Vorp. Biomechanical properties of ruptured versus electively repaired abdominal aortic aneurysm wall tissue. *J. Vasc. Surg.*, 43:570–576, 2006.

[186] M. L. Raghavan, M. M. Hanaoka, J. A. Kratzberg, M. de Lourdes Higuchi, and E. S. da Silva. Biomechanical failure properties and microstructural content of ruptured and unruptured abdominal aortic aneurysms. *J. Biomech.*, 44:2501–2507, 2011.

[187] C. Forsell, J. Swedenborg, J. Roy, and T. C. Gasser. The quasi-static failure properties of the abdominal aortic aneurysm wall estimated by a mixed experimental-numerical approach. *Ann. Biomed. Eng.*, 41:1554–1566, 2013.

[188] J. A. Tavares Monteiro, E. S. da Silva, M. L. Raghavan, P. Puech-Leão, M. de Lourdes Higuchi, and J. P. Otoch. Histologic, histochemical, and biomechanical properties of fragments isolated from the anterior wall of abdominal aortic aneurysms. *J. Vasc. Surg.*, 59:1393–1401, 2014.

[189] F. Tanios, M. W. Gee, J. Pelisek, S. Kehl, J. Biehler, V. Grabher-Meier, W. A. Wall, H. H. Eckstein, and C. Reeps. Interaction of biomechanics with extracellular matrix components in abdominal aortic aneurysm wall. *Eur. J. Vasc. Endovasc. Surg.*, 50: 167–174, 2015.

[190] D. A. Vorp, M. L. Raghavan, and M. W. Webster. Mechanical wall stress in abdominal aortic aneurysm: Influence of diameter and asymmetry. *J. Vasc. Surg.*, 27: 632–639, 1998.

[191] M. L. Raghavan, D. A. Vorp, M. P. Federle, M. S. Makaroun, and M. W. Webster. Wall stress distribution on three-dimensionally reconstructed models of human abdominal aortic aneurysm. *J. Vasc. Surg.*, 31:760–769, 2000.

[192] B. J. Doyle, A. Callanan, and T. M. McGloughlin. A comparison of modelling techniques for computing wall stress in abdominal aortic aneurysms. *Biomed. Eng. Online*, 6:137–161, 2007.

[193] S. S. Raut, A. Jana, V. De Oliveira, S. C. Muluk, and E. A. Finol. The effect of uncertainty in vascular wall material properties on abdominal aortic aneurysm wall mechanics. In B. Doyle, K. Miller, A. Wittek, and P. M. F. Nielsen, editors, *Computational Biomechanics for Medicine. Fundamental Science and Patient-specific Applications*, pages 69–86. Springer, New York, 2014.

[194] M. Carmo, L. Colombo, A. Bruno, F. R. Corsi, L. Roncoroni, M. S. Cuttin, F. Radice, E. Mussini, and P. G. Settembrini. Alteration of elastin, collagen and their cross-links in abdominal aortic aneurysms. *Eur. J. Vasc. Endovasc. Surg.*, 23: 543–549, 2002.

[195] D. A. Vorp. Biomechanics of abdominal aortic aneurysm. *J. Biomech.*, 40:1887–1902, 2007.

[196] J. H. Lindeman, B. A. Ashcroft, J. W. Beenakker, M. van Es, N. B. Koekkoek, F. A. Prins, J. F. Tielemans, H. Abdul-Hussien, R. A. Bank, and T. H. Oosterkamp. Distinct defects in collagen microarchitecture underlie vessel-wall failure in advanced abdominal aneurysms and aneurysms in Marfan syndrome. *Proc. Natl. Acad. Sci. USA*, 107:862–865, 2010.

[197] A. M. Robertson, X. Duan, K. M. Aziz, M. R. Hill, S. C. Watkins, and J. R. Cebral. Diversity in the strength and structure of unruptured cerebral aneurysms. *Ann. Biomed. Eng.*, 43:1502–1515, 2015.

[198] S. Polzer, T. C. Gasser, K. Novak, V. Man, M. Tichy, and P. Skacel J. Bursa. Structure-based constitutive model can accurately predict planar biaxial properties of aortic wall tissue. *Acta Biomater.*, 14:133–145, 2015.

[199] G. A. Holzapfel, J. A. Niestrawska, R. W. Ogden, A. J. Reinisch, and A. J. Schriefl. Modelling non-symmetric collagen fibre dispersion in arterial walls. *J. R. Soc. Interface*, 12:2015–0188, 2015.

[200] J. Schindelin, I. Arganda-Carreras, E. Frise, V. Kaynig, M. Longair, T. Pietzsch, S. Preibisch, C. Rueden, S. Saalfeld, B. Schmid, J. Y. Tinevez, D. J. White, V. Hartenstein, K. Eliceiri, P. Tomancak, and A. Cardona. Fiji: an open-source platform for biological-image analysis. *Nat. Methods*, 9:676–682, 2012.

[201] S. Sherifova. Modeling the propagation of aortic dissection. Master's thesis, KTH, School of Technology and Health (STH), 2015.

[202] G. Sommer, T. C. Gasser, P. Regitnig, M. Auer, and G. A. Holzapfel. Dissection properties of the human aortic media: an experimental study. *J. Biomech. Eng.*, 130: 021007–1–12, 2008.

[203] G. Sommer, D. C. Haspinger, M. Andrä, M. Sacherer, Ch. Viertler, P. Regitnig, and G. A. Holzapfel. Quantification of shear deformations and corresponding stresses in the biaxially tested human myocardium. *Ann. Biomed. Eng.*, 43:2234–2348, 2015.

[204] S. S. Hans, O. Jareunpoon, M. Balasubramaniam, and G. B. Zelenock. Size and location of thrombus in intact and ruptured abdominal aortic aneurysms. *J. Vasc. Surg.*, 41:584–588, 2005.

[205] L. Azinfar, M. Ravanfar, Y. Wang, K. Zhang, D. Duan, and G. Yao. High resolution imaging of the fibrous microstructure in bovine common carotid artery using optical polarization tractography. *J. Biophotonics*, 10:231–241, 2017.

[206] M. Auer, P. Regitnig, and G. A. Holzapfel. An automatic nonrigid registration for stained histological sections. *IEEE Trans. Image Process.*, 14:475–486, 2005.

[207] N. Sakalihasan, H. Kuivaniemi, B. Nusgens, R. Durieux, and J.-O. Defraigne. Aneurysm: epidemiology aetiology and pathophysiology. In T. M. McGloughlin, editor, *Biomechanics and Mechanobiology of Aneurysms*, pages 1–33. Springer, New York, 2010.

[208] Z. Teng, J. Feng, Y. Zhang, Y. Huang, M. P. F. Sutcliffe, A. J. Brown, Z. Jing, J. H. Gillard, and Q. Lu. Layer- and direction-specific material properties, extreme extensibility and ultimate material strength of human abdominal aorta and aneurysm: a uniaxial extension study. *Ann. Biomed. Eng.*, 43:2745–2759, 2015.

[209] J. Tong, T. Cohnert, and G. A. Holzapfel. Diameter-related variations of geometrical, mechanical and mass fraction data in the anterior portion of abdominal aortic aneurysms. *Eur. J. Vasc. Endovasc. Surg.*, 49:262–270, 2015.

[210] G. A. Holzapfel and R. W. Ogden. Constitutive modelling of passive myocardium: a structurally based framework for material characterization. *Phil. Trans. R. Soc. Lond. A*, 367:3445–3475, 2009.

[211] J. A. Niestrawska, Ch. Viertler, P. Regitnig, T. U. Cohnert, G. Sommer, and G. A. Holzapfel. Microstructure and mechanics of healthy and aneurysmatic abdominal aortas: experimental analysis and modeling. *J. R. Soc. Interface*, 13:2016–0620, 2016.

[212] M. J. Thubrikar, J. Al-Soudi, and F. Robicsek. Wall stress studies of abdominal aortic aneurysm in a clinical model. *Ann. Vasc. Surg.*, 15:355–366, 2001.

[213] B. J. Doyle, A. J. Cloonan, M. T. Walsh, D. A. Vorp, and T. M. McGloughlin. Identification of rupture locations in patient-specific abdominal aortic aneurysms using experimental and computational techniques. *J. Biomech.*, 43:1408–1416, 2010.

[214] M. M. Stringfellow, P. F. Lawrence, and R. G. Stringfellow. The influence of aorta-aneurysm geometry upon stress in the aneurysm wall. *J. Surg. Res.*, 42:425–433, 1987.

[215] D. C. McGiffin, P. B. McGiffin, A. J. Galbraith, and R. B. Cross. Aortic wall stress profile after repair of coarctation of the aorta. It is related to subsequent true aneurysm formation? *J. Thorac. Cardiovasc. Surg.*, 104:924–931, 1992.

[216] F. Inzoli, F. Boschetti, M. Zappa, T. Longo, and R. Fumero. Biomechanical factors in abdominal aortic aneurysm rupture. *Eur. J. Vasc. Surg.*, 7:667–674, 1993.

[217] W. R. Mower, L. J. Baraff, and J. Sneyd. Stress distributions in vascular aneurysms: factors affecting risk of aneurysm rupture. *J. Surg. Res.*, 55:155–161, 1993.

[218] J. F. Rodríguez, G. Martufi, M. Doblaré, and E. A. Finol. The effect of material model formulation in the stress analysis of abdominal aortic aneurysms. *Ann. Biomed. Eng.*, 37:2218–2221, 2009.

[219] MATLAB. R2016a, The MathWorks Inc., Natick, MA, USA, 2016.

[220] G. A. Holzapfel, G. Sommer, M. Auer, P. Regitnig, and R. W. Ogden. Layer-specific 3D residual deformations of human aortas with non-atherosclerotic intimal thickening. *Ann. Biomed. Eng.*, 35:530–545, 2007.

[221] S. E. Greenwald, J. E. Moore, Jr., A. Rachev, T. P. C. Kane, and J.-J. Meister. Experimental investigation of the distribution of residual strains in the artery wall. *J. Biomech. Eng.*, 119:438–444, 1997.

[222] L. Horný, M. Netušil, and T. Voňavková. Axial prestretch and circumferential distensibility in biomechanics of abdominal aorta. *Biomech. Model. Mechanobiol.*, 13: 783–799, 2014.

[223] A. B. Cubit. *Cubit 15.0 User Documentation*. Sandia National Laboratories, Albuquerque, New Mexico, USA, 2017.

[224] J. Helfenstein, M. Jabareen, E. Mazza, and S. Govindjee. On non-pyhsical response in models for fiber-reinforced hyperelastic materials. *Int. J. Solids Structures*, 47: 2056–2061, 2010.

[225] Z. Li and C. Kleinstreuer. A new wall stress equation for aneurysm-rupture prediction. *Ann. Biomed. Eng.*, 33:209–213, 2005.

[226] D. H. J. Wang, M. S. Makaroun, M. W. Webster, and D. A. Vorp. Effect of intraluminal thrombus on wall stress in patient-specific models of abdominal aortic aneurysm. *J. Vasc. Surg.*, 36:598–604, 2002.

[227] S. A. O'Leary, E. G. Kavanagh, P. A. Grace, T. M. McGloughlin, and B. J. Dolye. The biaxial mechanical behaviour of abdominal aortic aneurysm intraluminal thrombus: Classification of morphology and the determination of layer and region specific properties. *J. Biomech.*, 47:1430–1437, 2014.

[228] P. B. Dobrin, W. H. Baker, and W. C. Gley. Elastolytic and collagenolytic studies of arteries. Implications for the mechanical properties of aneurysms. *Arch. Surg.*, 119: 405–409, 1984.

[229] K. A. Wilson, J. S. Lindholt, P. R. Hoskins, L. Heickendorff, S. Vammen, and A. W. Bradbury. The relationship between abdominal aortic aneurysm distensibility and serum markers of elastin and collagen metabolism. *Eur. J. Vasc. Endovasc. Surg.*, 21:175–178, 2001.

[230] S. Menashi, J. S. Campa, R. M. Greenhalgh, and J. T. Powell. Collagen in abdominal aortic aneurysm: typing, content, and degradation. *J. Vasc. Surg.*, 6:578–582, 1987.

[231] R. J. Rizzo, W. J. McCarthy, S. N. Dixit, M. P. Lilly, V. P. Shively, W. R. Flinn, and J. S. Yao. Collagen types and matrix protein content in human abdominal aortic aneurysms. *J. Vasc. Surg.*, 10:365–373, 1989.

[232] G. S. McGee, B. T. Baxter, V. P. Shively, R. Chisholm, W. J. McCarthy, W. R. Flinn, J. S. Yao, and W. H. Pearce. Aneurysm or occlusive disease–factors determining the clinical course of atherosclerosis of the infrarenal aorta. *Surgery*, 110:370–375, 1991.

[233] R. H. Gandhi, E. Irizarry, J. O. Cantor, S. Keller, G. B. Nackman, V. J. Halpern, K. M. Newman, and M. D. Tilson. Analysis of elastin cross-linking and the connective tissue matrix of abdominal aortic aneurysms. *Surgery*, 115:617–620, 1994.

[234] H. Kuivaniemi, E. J. Ryer, J. R. Elmore, and G. Tromp. Understanding the pathogenesis of abdominal aortic aneurysms. *Expert Rev. Cardiovasc. Ther.*, 13:975–987, 2015.

[235] J. A. Curci and R. W. Thompson. Adaptive cellular immunity in aortic aneurysms: cause, consequence,or context? *J. Clin. Invest.*, 114:168–171, 2004.

[236] H. Kugo, N. Zaima, H. Tanaka, Y. Mouri, K. Yanagimoto, K. Hayamizu, K. Hashimoto, T. Sasaki, M. Sano, T. Yata, T. Urano, M. Setou, N. Unno, and T. Moriyama. Adipocyte in vascular wall can induce the rupture of abdominal aorticaneurysm. *Sci. Rep.*, 6:31268, 2016.

[237] H. Kugo, N. Zaima, H. Tanaka, K. Hashimoto, C. Miyamoto, A. Sawaragi, T. Urano, N. Unno, and T. Moriyama. Pathological analysis of the ruptured vascular wall of hypoperfusion-induced abdominal aortic aneurysm animal model. *J. Orthop. Sc.*, 66:499–506, 2017.

[238] H. Tanaka, N. Zaima, T. Sasaki, M. Sano, N. Yamamoto, T. Saito, K. Inuzuka, T. Hayasaka, N. Goto-Inoue, Y. Sugiura, K. Sato, H. Kugo, T. Moriyama, H. Konno, M. Setou, and N. Unno. Hypoperfusion of the adventitial vasa vasorum develops an abdominal aortic aneurysm. *PLoS One*, 10:0134386, 2015.

[239] H. Tanaka, N. Zaima, T. Sasaki, N. Yamamoto, K. Inuzuka, M. Sano, T. Saito, T. Hayasaka, N. Goto-Inoue, K. Sato, H. Kugo, T. Moriyama, H. Konno, M. Setou, and N. Unno. Imaging mass spectrometry reveals a unique distribution of triglycerides in the abdominal aortic aneurysmal wall. *J. Vasc. Res.*, 52:127–135, 2015.

[240] E. Ollikainen, R. Tulamo, S. Lehti, M. Lee-Rueckert, J. Hernesniemi, M. Niemelä, S. Ylä-Herttuala, P. T. Kovanen, and J. Frösen. Smooth muscle cell foam cell formation, apolipoproteins, and ABCA1 in intracranial aneurysms: implications for lipid accumulation as a promoter of aneurysm all rupture. *J. Neuropath. Exp. Neur.*, 75: 689–699, 2016.

[241] G. N. Chaldakov. Cardiovascular adipobiology: A novel – heart-associated adipose tissuein cardiovascular disease. *Serbian Journal of Experimental and Clinical Research*, 9:81–88, 2008.

[242] S. B. Police, S. E. Thatcher, R. Charnigo, A. Daugherty, and L. A. Cassis. Obesity promotes inflammation in periaortic adipose tissue and angiotensin II-induced abdominal aortic aneurysm formation. *Arterioscler. Thromb. Vasc. Biol.*, 29:1458–1464, 2009.

[243] K. Shimizu, R. N. Mitchell, and P. Libby. Inflammation and cellular immune responses in abdominal aortic aneurysms. *Arterioscler. Thromb. Vasc. Biol.*, 26:987–994, 2006.

[244] C. M. Brophy, J. M. Reilly, G. J. W. Smith, and M. D. Tilson. The role of inflammation in nonspecific abdominal aortic aneurysm disease. *Ann. Vasc. Surg.*, 5: 229–233, 1991.

[245] N. Sakalihasan, A. Heyeres, B. V. Nusgens, R. Limet, and C. M. Lapiére. Modifications of the extracellular matrix of aneurysmal abdominal aortas as a function of their size. *Eur. J. Vasc. Surg.*, 7:633–637, 1993.

[246] J. V. White, K. Haas, S. Phillips, and A. J. Comerota. Adventitial elastolysis is a primary event in aneurysm formation. *J. Vasc. Surg.*, 17:371–380, 1993.

[247] K. Karastergiou and V. Mohamed-Ali. The autocrine and paracrine roles of adipokines. *Mol. Cell. Endocrinol.*, 318:69–78, 2010.

[248] S. Galic, J. S. Oakhill, and G. R. Steinberg. Adipose tissue as an endocrine organ. *Mol. Cell. Endocrinol.*, 316:129–139, 2010.

[249] T. Tsuruda, J. Kato, K. Hatakeyama, K. Kojima, M. Yano, Y. Yano, K. Nakamura, F. Nakamura-Uchiyama, Y. Matsushima, T. Imamura, T. Onitsuka, Y. Asada, Y. Nawa, T. Eto, and K. Kitamura. Adventitial mast cells contribute to pathogenesis in the progression of abdominal aortic aneurysm. *Circ. Res.*, 102:1368–1377, 2008.

[250] H. Åstrand, Å. Rydén-Ahlgren, T. Sandgren, and T. Länne. Age-related increase in wall stress of the human abdominal aorta: an in vivo study. *J. Vasc. Surg.*, 42: 926–931, 2005.

[251] T. Tsuruda, T. Imamura, K. Hatakeyama, Y. Asada, and K. Kitamura. Stromal cell biology–a way to understand the evolution of cardiovascular diseases. *Circ. J.*, 74: 1042–1050, 2010.

[252] K. Maiellaro and W. R. Taylor. The role of the adventitia in vascular inflammation. *Cardiovasc. Res.*, 75:640–648, 2007.

[253] S. Cinti, G. Mitchell, G. Barbatelli, I. Murano, E. Ceresi, E. Faloia, S. Wang, M. Fortier, A. S. Greenberg, and M. S. Obin. Adipocyte death defines macrophage localization and function in adipose tissue of obese mice and humans. *J. Lipid Res.*, 46:2347–2355, 2005.

[254] J. H. Lindeman, T. J. Rabelink, and J. H. van Bockel. Immunosuppression and the abdominal aortic aneurysm: Doctor Jekyll or Mister Hyde? *Circulation*, 124: e463–e465, 2011.

[255] K. A. Wilson, A. J. Lee, P. R. Hoskins, F. G. Fowkes, C. V. Ruckley, and A. W. Bradbury. The relationship between aortic wall distensibility and rupture of infrarenal abdominal aortic aneurysm. *Eur. J. Vasc. Endovasc. Surg.*, 37:112–117, 2003.

[256] E. F. Steinmetz, C. Buckley, M. L. Shames, T. L. Ennis, S. J. Vanvickle-Chavez, D. Mao, L. A. Goeddel, C. J. Hawkins, and R. W. Thompson. Treatment with simvastatin suppresses the development of experimental abdominal aortic aneurysms in normal and hypercholesterolemic mice. *Ann. Surg.*, 241:92–101, 2005.

[257] A. Kalyanasundaram, J. R. Elmore, J. R. Manazer, A. Golden, D. P. Franklin, S. W. Galt, E. M. Zakhary, and D. J. Carey. Simvastatin suppresses experimental aortic aneurysm expansion. *J. Vasc. Surg.*, 43:117–124, 2006.

[258] R. Hurks, I. E. Hoefer, A. Vink, G. Pasterkamp, A. Schoneveld, M. Kerver, J. P. de Vries, M. J. Tangelder, and F. L. Moll. Different effects of commonly prescribed statins on abdominal aortic aneurysm wall biology. *Eur. J. Vasc. Endovasc. Surg.*, 39:569–576, 2010.